Topographic SAR Estimation and Processing for Multi-Aperture Spaceborne Radar

by

Ashwin Mohan

B.E., Electrical and Electronics Engineering

Sri Jayachamarajendra College of Engineering

University of Mysore

Mysore, India, 2001

Submitted to the Department of Electrical Engineering and Computer Science and the faculty of the Graduate School of the University of Kansas in partial fulfillment of the requirements for the degree of Master of Science

Thesis Committee

_____

Dr. James M. Stiles (Chair)

_____

Dr. Muhammad Dawood

_____

Dr. Glenn Prescott

Date of Thesis Defense: January 24th, 2005

ACKNOWLEDGEMENTS

I would like to express my sincere gratitude to my research advisor Dr. James Stiles for encouraging me to take up research and motivating me at every step of my thesis work. His wonderful method of teaching and his inspirational words will always help me strive to be a better engineer. I have learnt a lot of valuable lessons from his advise, which will help me a lot to shape my career.

I would like to thank Dr. Muhammad Dawood for accepting to serve on my thesis committee and taking his time out to thoroughly review this document. His recommendations and suggestions have greatly contributed to making this document more perfect and presentable.

I would also like to thank Dr. Glenn Prescott for introducing me to many important concepts in digital signal processing and for accepting to serve on my thesis committee.

Special thanks to my parents Mohan and Rema for their unparalleled love and encouragement and for allowing me chase my dreams and my sister Archana for her endless love and support. To them, I owe all the good things in my life. I thank all my friends back home in India for their constant support and encouragement and my friends in Lawrence for making my stay here such a joyful and memorable experience. Last but not the least, I would like to thank the Almighty. It is my faith in Him that has driven me to stay focused and succeed even when the going gets tough.

TABLE OF CONTENTS

LIST OF FIGURES

LIST OF TABLES

ABSTRACT

A radar sensor may be constructed by deploying a spatially distributed cluster of small and relatively simple radar satellites (also called microsats), thus constituting a single "distributed" radar sensor, whose spatial extent may exceed hundreds of meters or even kilometers. While each array element (microsat) by itself will be a poor radar sensor, the collection and proper processing of radar data from each microsat would form a single, distributed radar sensor whose performance can potentially exceed any single radar system.

In recent years, significant research has been directed at solving problems associated with the Synthetic Aperture Radar (SAR) using this distributed sensor concept. However, little progress has been made on applying this concept to the problem of forming topographic SAR images, a technique in which a surface map of both scattering intensity and surface height is produced, resulting in a three-dimensional topographic map of an illuminated surface

The existing models and associated topographic SAR algorithms used to obtain high-precision digital elevation models were developed under the assumption that every spatial element provides a quality SAR image. However, this does not apply to the distributed sensor because, under dynamic flight conditions, the array formed by the constellation of multi-satellites will be sparsely populated and randomly spaced. Furthermore, since individual elements forming the constellation are limited in aperture, no single element is capable of producing quality SAR

images. Hence, the mathematical models and algorithms developed for conventional Top SAR are not suitable for random and sparse configurations.

The main focus of this thesis is to develop algorithms for determining accurate and unambiguous estimates of surface height using the space-time radar measurements provided by a distributed radar array. A technique is first developed to organize the information collected by a distributed system. Using *eigensensor analysis*, the five sensor parameters of the radar-time, frequency and 3D spatial location- are equivalently represented by a 3D synthetic aperture. Using this synthetic aperture, effective topographic SAR processing and estimation algorithms were developed. The developed algorithms were tested for different topographic scenarios.

1. INTRODUCTION

1.1 Motivation

Over the last few years, there has been considerable interest in the concept of moving radar technology on to spaceborne platforms. The main reason why this mode of radar operation is preferred is because of the several advantages that it offers. Spaceborne radars do not require any on board personnel or flight operators. This, in effect, means that no human beings are placed in a position of danger during the process of data acquisition. Air-borne vehicles are the usual targets for destruction during any military conflict. However radars on space-based platforms are safe once they are placed in orbit and hence are very useful for reconnaissance and other military applications.

However, one of the biggest advantages of using spaceborne radars is its ability to provide global coverage. Radars on airborne platforms are limited by airspace restrictions and their coverage is therefore limited. However, no such restriction applies to spaceborne radars. At the same time, as with most engineering solutions, there are also a few disadvantages associated with space-based radar technology. One of the biggest constraints is the trade-off involving sensor weight, size and power. Microwave radar uses an electromagnetic wavelength longer, by several orders of magnitude, than optical or infrared systems, and thus the sensing aperture (i.e. antenna) size must be correspondingly larger. Another problem arises from the fact that the radar is an active sensor, which means that it must generate the

large electromagnetic power required to illuminate targets of interest. This "power-aperture" problem has proved to be a major stumbling block when it comes to implementing space-based radar systems because constructing and deploying a satellite with a very large antenna structure while generating high transmitter power is both a difficult and costly endeavor. The decision to implement a cluster of "radar satellites" is mainly directed towards mitigating this space-size-power tradeoff problem.

The main motivation behind the use of such radar satellite constellations is that instead of building a single large, complex satellite, we could deploy a spatially distributed cluster of small and relatively simple radar satellites called microsats. With this approach, we no longer face the problem of having to build a single large antenna structure with a design capable of generating high transmitter power. This burden is now distributed across many satellites. Each satellite in this "microsat" constellation implements a transmitter, a receiver and a processor and thus a large, sparse multi-static radar array is formed in space. Since we have replaced a large aperture with smaller radar constellations, the system we have now constitutes a single "distributed" radar sensor, which is capable of illuminating a very large area. Although each array element alone is not useful for any specific application, a colllection of such radar microsats would form a single, distributed radar sensor whose performance exceeds that of a single-aperture radar system. The advantages of this system are numerous: it involves smaller, lighter and less expensive systems. An individual system failure merely degrades the performance of the entire distributed

radar system and the overall system performance can be augmented at any time in the future by adding more individual systems [1]. Figure 1-1 provides an interesting illustration of the arrangement of multi-aperture sparse arrays in space.

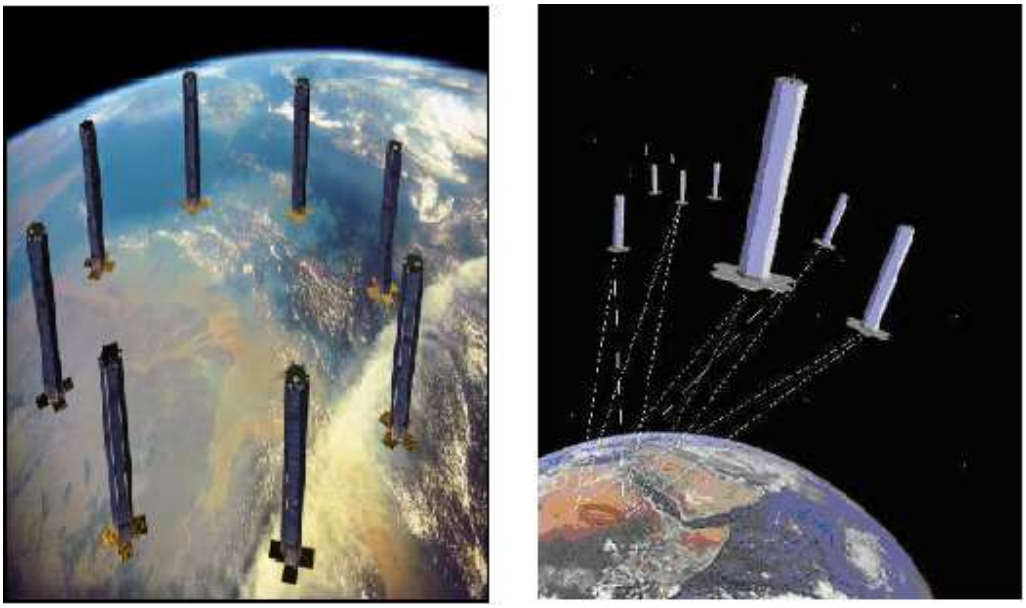

Figure 1-1 Multi-aperture sparse array formations [19,20]

A significant amount of research has been directed towards solving problems associated with applying this distributed sensor concept to the SAR and GMTI radar problems. Some spaceborne configurations that have been suggested are the Interferometer Cartwheel in Europe [14] and the TechSat21 concept in the USA [12]. The Interferometric Cartwheel is proposed as a passive (receive-only) constellation of micro-satellites in a special orbit configuration. Such a system produces a set of radar images which can be combined to improve the final resolution in range and azimuth and thus systematically produce across-track and along-track interferometric data. On the other hand, the TechSat21 employs a cluster of free-floating satellites, each of which transmits its own orthogonal signal and receives all reflected signals. The

cluster essentially forms a multi-element interferometer with a large number of grating lobes and significant ground clutter. The primary applications of the cartwheel are generation of the Digital Elevation Model (DEM) using cross-track interferometry and the mapping of ocean current using the along-track configuration. The TechSat21 has been primarily focused on SAR and Moving Target Indicator (MTI).

One of the most important research goals in this area involves improving the accuracy of elevation estimates. However, little progress has been made on applying this concept to the problem of forming topographic SAR (TopSAR) images using sparse and randomly spaced arrays resulting from realistic dynamic constraints. Typically, a sparse array will result in a beam pattern that is not really useful because it exhibits significant sidelobe levels across all directions outside the mainbeam, thereby influencing the accuracy of the SAR images. However, with the right kind of processing, such a sparse array can provide a significant improvement in radar performance and prove to be useful for topography-estimation applications.

We now go back to our discussion about the features of a distributed radar constellation because a clear understanding of the same is required to appreciate the complexities involved when it comes to processing the responses and extracting information from such systems. One important requirement of a *distributed sensor*, which consists of several microsat constellations, is that the relative position of each microsat remains approximately constant with time. However, what might actually happen is that such a collection of satellites at different altitudes (and therefore different velocities) might drift apart as they orbit the Earth. This in turn means that

we need to expend more fuel in order to make sure the arrangement of the radar constellation remains relatively stable and does not change with time. However, what we could do to overcome this problem is design the array geometry in such a way that we can construct a satellite constellation which remains approximately constant as it orbits the Earth. This in turn ensures that a minimum amount of fuel is required to control the precise positioning of these satellites. Traditional antenna arrays are dense and regularly spaced while the microsat elements of a stable constellation turn out to be sparse and randomly distributed. Hence, it is obvious that a *dynamically stable* distributed radar would be significantly different from an airborne distributed radar sensor. Because of the evident difference in geometry, new radar signal processing algorithms must be created for this distributed sensor.

The concept of SAR interferometry basically involves using two SAR sensors, which are vertically displaced to form an interferometric baseline. By comparing the complex phase difference between the two resulting SAR images, a topographic map can be produced. In particular, extracting the height information of the corresponding data of a certain area is an interesting application. Although the distributed radar constellation, which is at our disposal, provides multiple interferometric baselines (N satellites provide (N-1)*N/2 baselines), what we should note is that we still do not have multiple interferometric SAR baselines. Moreover, the main problem associated with the distributed design is that each microsat element is likely to have insufficient power and aperture size and consequently, no accurate estimates can be generated with the data collected by one single element alone. In other words, the measurements

collected by just one constellation element are not enough to form an unambiguous SAR image. What we need is the accumulation of data from all the microsats in order to obtain accurate estimates. Therefore, again, we come to the conclusion that standard interferometric algorithms and techniques are not applicable to this new distributed sensor concept. New processing algorithms must be derived and applied to provide a topographic map of improved accuracy over other interferometric SAR concepts.

1.2 Organization of the document

The following chapters of this document contain a detailed description and analysis of the methodology adopted for developing topographic SAR estimation and processing algorithms for a multi-aperture spaceborne radar.

Chapter two deals with a detailed description of the software simulator developed using Matlab. This simulator provides a set of complex valued samples, which constitute the measurement data, collected by a sparse and random configuration of antennas. The mathematics behind the modeling of this radar response vector will be described in detail. The second half of this chapter will deal with a discussion about the transformation matrix and its interpretation. This will lead to a detailed derivation of the 3D Synthetic aperture using *eigensensor* analysis followed by a few simulation examples.

Chapter three deals with the development and implementation of a Kalman Filter for processing of data obtained from a multiple-aperture spaceborne radar [3].

The performance of the Kalman filter is evaluated with two different test cases and the advantages of this algorithm over the other estimators are briefly discussed.

Chapter four deals with the theory behind topography estimation using distributed radar array measurements. We start by looking at the conventional topographic SAR, discuss the geometry and the concepts involved in height estimation using standard interferometric techniques and then extend this idea to the distributed topographic SAR. This chapter ends with a discussion about optimal partitioning of the measurement space in order to form a set of two SAR images.

Chapter five forms the core of the thesis and starts by completely describing the topography-estimation algorithm developed during the course of this research. The first test case looks at a simple two-dimensional situation and enables us to understand the effects of eigensensor analysis. This test also helps us to decide on the methodology to be adopted for optimal partitioning of the measurement space. The second test case deals with a more realistic three-dimensional situation and we test the algorithm with different topographic scenarios. The forward-look SAR geometry is explained in detail and compared with the standard side-look case. The results obtained are displayed in the form of three-dimensional elevation models as well as contour plots.

Chapter six summarizes all the concepts developed during the research, presents conclusions and recommends possible opportunities for future research work.

2. MULTI-APERTURE SPACE-BORNE ARRAYS

2.1 The Multi-aperture SAR Simulator

Due to the lack of actual multi-aperture sparse radar array data, it is necessary to create a software model, which will enable us to procure an accurate set of complex receiver samples that accurately reflect the measurements of an arbitrary space-time radar when it is illuminating an arbitrary and diverse target set. This section aims at providing a brief illustration of the mathematics that describe a multi-aperture spaceborne radar model [4]. Figure 2-1 depicts the radar geometry.

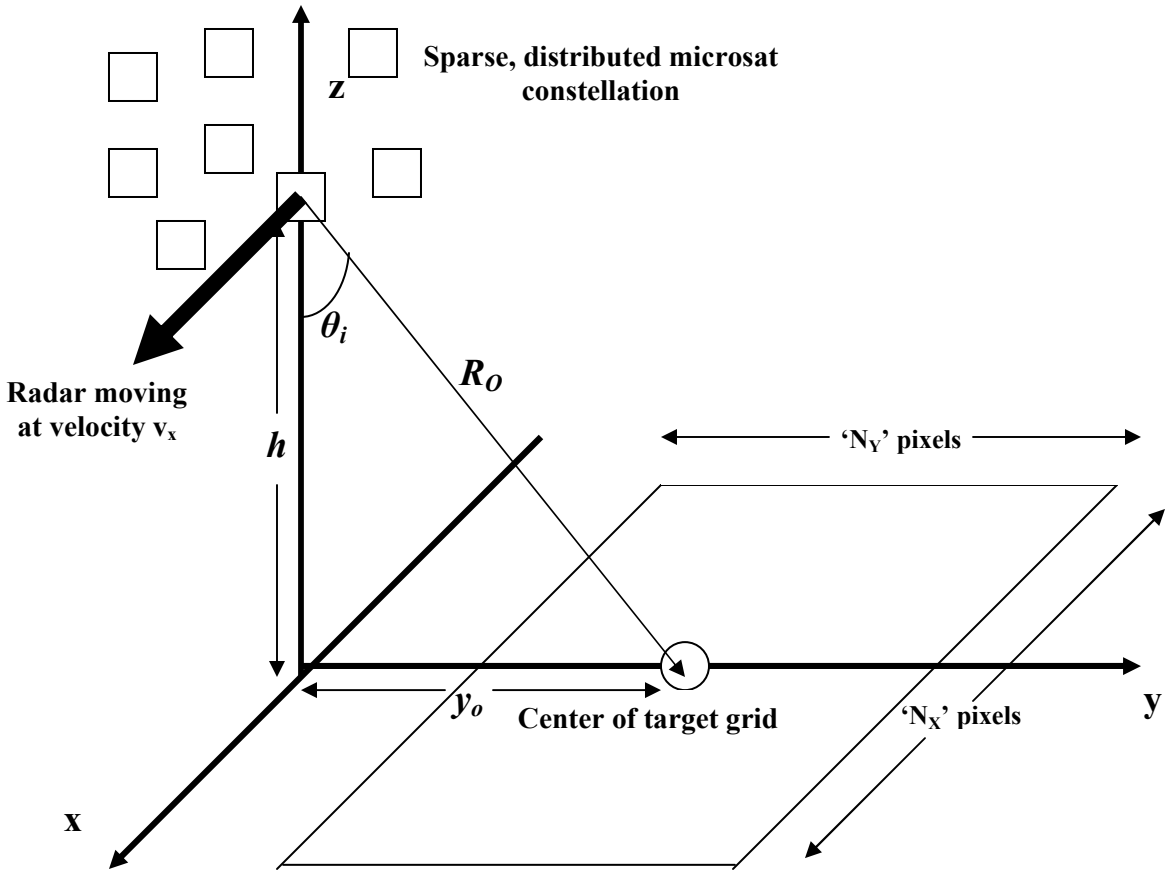

Figure 2-1 Radar Geometry (Side-look case)

2.1.1 Model description - Transmit space

The multi-aperture space-borne radar transmit space consists of two sub-spaces, the temporal (time-frequency) sub-space, and the spatial sub-space. The spatial sub-space consists of three dimensions extending across the three spatial dimensions and basically defines the location of the transmit antenna. The temporal sub-space, on the other hand, spreads out across the dimensions of time and frequency. To be more specific, we could say that the transmit signal is described by a weighted superposition of a set of wide timewidth, wide bandwidth orthonormal basis functions. A windowed Fourier transform is used to describe the transmit signal in terms of (slow-time basis functions) time and (fast-time basis functions) frequency. This result is then sampled across time and frequency, so that the signal can be described as a set of ($B*T$) complex values. The transmit signal sent out by the radar thus consists of a set of complex valued samples that spread out across this overall five-dimensional space. The various vectors that occupy the transmit space are:

$\bar{z}_j^S$ - denotes a vector which occupies the spatial sub-space and represents the position vector specifying the location of the j^{th} transmit antenna.

$\bar{z}_k^t$ - denotes a vector which occupies the temporal (time-frequency) sub-space

The transmit temporal position vectors could be visualized as pointing to locations on a two-dimensional grid which has U number of samples in the 'time' direction and V number of samples in the 'frequency' direction.

$\bar{z}_{jk}$ denotes the combined five dimensional vector in the total transmit signal space and is of the form

$$\bar{z}_{jk} = [x_j, y_j, z_j, t_k, \omega_k]^T \tag{2.1}$$

The vector shown above completely describes the spatial location of the j^{th} transmit antenna and values of the k^{th} time-frequency sample associated with it. The transmit signal generated by this particular transmit antenna is given by $s(\bar{z}_{jk})$. All the elements of the transmit signal can thus be arranged into a single *N*-dimensional vector where *N*= *J***K*. *N* refers to the total number of complex-valued samples contained in the transmit signal while *J* refers to the number of transmit antennas and *K* refers to the number of time-frequency samples transmitted by each of those transmit antennas.

2.1.2 Model description – Target space

The entire target space is characterized with a complex scattering coefficient γ and a set of position vectors corresponding to each target pixel. The target position vector is denoted by

$$\bar{y}_t = [x_t, y_t, z_t, v_t] \tag{2.2}$$

where x_t, y_t and z_t define the position of the t^{th} target in a three-dimensional cartesian space while v_t specifies the radial velocity of the target with respect to ground velocity.

$\boldsymbol{\gamma} = [\gamma_1, \gamma_2, \gamma_3 ..... \gamma_{N_t}]$ represents a vector of dimension equal to N_t (the number of targets) and contains the complex scattering values corresponding to each target.

2.1.3 Model description – Receiver space

Just as we observed with the transmit space, the radar receive space also consists of a three-dimensional spatial sub-space and a two-dimensional temporal (time-frequency) sub-space. The various vectors that constitute the receive (sensor) space are:

$\overline{s}_i^s$ - denotes a vector which occupies the spatial sub-space and represents the position vector specifying the location of the i^{th} receive antenna.

$\overline{s}_{k'}^t$ - denotes a vector which occupies the temporal (time-frequency) sub-space

$\overline{s}_{ik'}$ denotes the combined five dimensional vector in the receive space and is of the form

$$\overline{s}_{ik'} = [x_i, y_i, z_i, t_{k'}, \omega_{k'}]^T \tag{2.3}$$

All the elements of the receive signal can be arranged into a single *M*-dimensional vector where *M= I*K'*. *M* refers to the total number of complex-valued samples that constitude the received signal while *I* refers to the number of receive antennas and *K'* refers to the number of time-frequency samples received by each receive antenna element. The radar response vector **r** is, therefore, an *M*-dimensional vector and contains all the complex measurement values that represent the A/D samples of a space-time radar.

The main function of the simulator is to simulate this radar response vector by modeling the electromagnetic effects on the transmitted, scattered and the received signal. To achieve this, we need to relate the receive measurements to the target and the transmit signal description via far-field propagation operators. The following operators further assist us to model this radar response vector.

$\bar{\bar{K}}_{\theta}$ - is the frequency matrix which relates the transmit space to the target space

$\bar{\bar{K}}_{\varphi}$ - is the frequency matrix which relates the receive signal space to the target position space.

The frequency matrix is also termed as the *Transformation matrix* and will be explained in detail in the next section,

$\mathbf{n} = [n_1, n_2, n_3, n_4, n_5 ..... n_M]^T$ is a vector of the same dimension as the measurement vector and represents the measurement noise. Each element of that vector is a zero-mean complex random variable with variance σ_n^2

We also define a matrix **H** that is a very important part of the radar model equation and is called the *propagation matrix*. This is because the **H**-matrix completely models the propagation effects on the transmit signal as it travels from the transmitter to the target, undergoes scattering and is received back at the radar. It should be noted that the evaluation of the **H**-matrix involves far-field approximations considering the given space-based radar scenario.

The **H**-matrix contains elements of the form,

$$H_t^{mn} = g_h(m,n:t)e^{-j\bar{s}_m^{sT}\bar{\bar{K}}_\varphi^{sT}\bar{y}_t}e^{-j\bar{y}_t^T\bar{\bar{K}}_\theta^s\bar{z}_n^s}e^{-j\bar{y}_t^T(\bar{\bar{K}}_\varphi^t\bar{\bar{K}}_\theta^t)\bar{z}_n^t} \tag{2.4}$$

where H_t^{mn} is an *M-by-N* matrix corresponding to target '*t*'. *M* refers to the total number of received samples while *N* refers to the number of transmit signal samples. $g_h(m,n:t)$ is a complex weighting function that relates the transmit temporal and spatial samples to each other, for a given target *t*.

With the above definitions, we can now proceed and obtain an expression for the M-dimensional measurement vector, $\mathbf{r}$.

The transmit signal $\mathbf{s}$, target scattering coefficient γ_t and the measurement noise vector $\mathbf{n}$ are related to the response vector $\mathbf{r}$ as,

$$\mathbf{r} = \sum_t^{N_t} \gamma_t \mathbf{H}_t \mathbf{s} + \mathbf{n} \tag{2.5}$$

where $\mathbf{r}$ is the measurement vector consisting of *M* samples.

We could go ahead and define an *M-dimensional* normalized measurement vector $\boldsymbol{\rho_t}$ for each target such that

$$\boldsymbol{\rho}_t = \mathbf{H}_t \mathbf{s} \tag{2.6}$$

The normalized measurement vector described above is a very important vector because it is basically the full set of measurement vectors obtained by a radar at a discrete set of space and time locations due to a particular target. If these response vectors are weighted by their appropriate scattering coefficient values and added

together, the result would be the set of measurements obtained by a radar due to all scatterers within the illuminated area.

Thus,

$$\mathbf{r} = \sum_{t}^{N_t} \gamma_t \boldsymbol{\rho}_t + \mathbf{n} \tag{2.7}$$

We can now define another matrix $\mathbf{P}$ which is basically the collection of the normalized response vectors corresponding to each target. Thus, we have

$$\mathbf{P} = \begin{bmatrix} \boldsymbol{\rho}_1 & \boldsymbol{\rho}_2 & \boldsymbol{\rho}_3 & .... & \boldsymbol{\rho}_{N_t} \end{bmatrix} \tag{2.8}$$

Thus, the entire set of measurements can now be represented in matrix-vector notation as,

$$\mathbf{r} = \mathbf{P}\boldsymbol{\gamma} + \mathbf{n} \tag{2.9}$$

2.2 The Transformation Matrix and its interpretation

In the previous section, we looked at the various model equations that finally lead to the expression for radar response. (2.9) contains all the components of the radar physics and expresses the complex measurement that would be obtained by a radar due to a set of scatterers (targets). The received signal is a delayed version of the transmit signal with a phase component that depends on the time-varying propagation delay. The transformation matrix provides information about the rate of change of the phase of the radar response with respect to various sensor and target parameters. We now proceed by defining some important parameters which will be useful to derive the transformation matrix.

With reference to the radar geometry shown in Figure 2-1, the spaceborne system travels in the positive direction at velocity v_x and the array phase reference is located at the origin of the coordinate system. Assuming a flat earth, the z-coordinate of all targets on the ground is $-h$, where h is the altitude of the array phase reference [1]. The following vectors are useful to proceed with derivation of the transformation matrix:

$\bar{y}_t = \begin{bmatrix} x_t & y_t & -h \end{bmatrix}^T$ denotes the position of a target on the earth's surface where

$z_t = -h$

$\bar{v} = \begin{bmatrix} v_x & 0 & 0 \end{bmatrix}$ represents the radar system's velocity

$\bar{s}_i = \begin{bmatrix} x_i & y_i & z_i \end{bmatrix}$ represents the location of the the i^{th} sensor (radar receiver). This vector contains only the spatial information of a receive antenna and is therefore a subset of the $\bar{s}_{ik}$, vector defined in the previous section.

In terms of the above position and velocity vectors, the range from the transmitter to a target is given by,

$$R_{tx-tgt} = \left|\bar{s}_i - \bar{y}_t\right| = \sqrt{(v_x t - x_t)^2 + (y_t)^2 + (h)^2} \tag{2.10}$$

Similarly, the range from the target back to a receiver is given by,

$$R_{tgt-rx} = \left|\bar{s}_i + \bar{v}t - \bar{y}_t\right| = \sqrt{(x_i + v_x t - x_t)^2 + (y_i - y_t)^2 + (z_i + h)^2} \tag{2.11}$$

The two-way propagation delay is therefore given by,

$$\tau = \frac{1}{c}\left[\sqrt{(x_i + v_x t - x_t)^2 + (y_i - y_t)^2 + (z_i + h)^2} + \sqrt{(v_x t - x_t)^2 + (y_t)^2 + (h)^2}\right] \tag{2.12}$$

The phase of the radar response will finally be,

$$\psi = \omega\tau \tag{2.13}$$

or,

$$\psi = \frac{\omega}{c}\left[\sqrt{(x_i + v_x t - x_t)^2 + (y_i - y_t)^2 + (z_i + h)^2} + \sqrt{(v_x t - x_t)^2 + (y_t)^2 + (h)^2}\right] \tag{2.14}$$

In order to obtain the sensor transformation matrix and then the synthetic sensor, two first-order Taylor expansions of the phase of the radar response are carried out [1,10]. Thereafter, using the array phase reference, mean sensor time and mean frequency, the sensor parameters around which the expansion is performed are given by,

$$\bar{s}_o = \begin{bmatrix} 0 & 0 & 0 & \omega_c & 0 \end{bmatrix}^T \tag{2.15}$$

The central point of illumination on the ground and thus the point around which the expansion is performed is taken as,

$$\bar{y}_O = \begin{bmatrix} x_O & y_O & -h \end{bmatrix} \tag{2.16}$$

Now, in terms of derivates, the sensor transformation matrix relating the receive signal space to the target position space - $\bar{\bar{K}}_\varphi$ is given by,

$$\bar{\bar{K}}_\varphi = \begin{bmatrix} \frac{\partial^2}{\partial x_t \partial x_i} & \frac{\partial^2}{\partial x_t \partial y_i} & \frac{\partial^2}{\partial x_t \partial z_i} & \frac{\partial^2}{\partial x_t \partial t_k'} & \frac{\partial^2}{\partial x_t \partial \omega_k'} \\ \frac{\partial^2}{\partial y_t \partial x_i} & \frac{\partial^2}{\partial y_t \partial y_i} & \frac{\partial^2}{\partial y_t \partial z_i} & \frac{\partial^2}{\partial y_t \partial t_k'} & \frac{\partial^2}{\partial y_t \partial \omega_k'} \\ \frac{\partial^2}{\partial h \partial x_i} & \frac{\partial^2}{\partial h \partial y_i} & \frac{\partial^2}{\partial h \partial z_i} & \frac{\partial^2}{\partial h \partial t_k'} & \frac{\partial^2}{\partial h \partial \omega_k'} \end{bmatrix} \Psi \tag{2.17}$$

Substituting (2.14) - (2.16) into (2.17), and evaluating the above matrix at $\overline{s}_o$ and $\overline{y}_o$, the sensor transformation matrix becomes,

$$\overline{\overline{K}}_\varphi = \frac{w_c}{c}\begin{bmatrix} \frac{-(h^2+y_o^2)}{R_o^3} & \frac{x_o y_o}{R_o^3} & \frac{-hx_o}{R_o^3} & \frac{-2v_x(h^2+y_o^2)}{R_o^3} & \frac{2x_o}{w_c R_o} \\ \frac{x_o y_o}{R_o^3} & \frac{-(h^2+x_o^2)}{R_o^3} & \frac{-hy_o}{R_o^3} & \frac{2v_x x_o y_o}{w_c R_o} & \frac{2y_o}{w_c R_o} \\ \frac{-hx_o}{R_o^3} & \frac{-hy_o}{R_o^3} & \frac{-(x_o^2+y_o^2)}{R_o^3} & \frac{-2hx_o}{R_o^3} & \frac{-2h}{w_c R_o} \end{bmatrix} \quad (2.18)$$

where *(x_o,y_o,-h)*, represents the center of the square grid comprising the target pixels and $R_o = \sqrt{x_o^2 + y_o^2 + h^2}$.

If we consider a standard side-looking case, then $x_o = 0$ and the sensor transformation matrix becomes,

$$\overline{\overline{K}}_\varphi = \frac{w_c}{c}\begin{bmatrix} \frac{-1}{R_o} & 0 & 0 & \frac{-2v_x}{R_o} & 0 \\ 0 & \frac{-h^2}{R_o^3} & \frac{-hy_o}{R_o^3} & 0 & \frac{2y_o}{w_c R_o} \\ 0 & \frac{-hy_o}{R_o^3} & \frac{-y_o^2}{R_o^3} & 0 & \frac{-2h}{w_c R_o} \end{bmatrix} \quad (2.19)$$

We can split the transformation matrix into separate spatial and temporal pieces such that

$$K^{spatial} = \frac{w_c}{c}\begin{bmatrix} \frac{-1}{R_o} & 0 & 0 \\ 0 & \frac{-h^2}{R_o^3} & \frac{-hy_o}{R_o^3} \\ 0 & \frac{-hy_o}{R_o^3} & \frac{-y_o^2}{R_o^3} \end{bmatrix} \text{ and } K^{temporal} = \begin{bmatrix} \frac{-2v_x}{R_o} & 0 \\ 0 & \frac{2y_o}{w_c R_o} \\ 0 & \frac{-2h}{w_c R_o} \end{bmatrix}$$

(2.20)

The sensor transformation matrix thus provides with information regarding the change of phase with respect to various parameters such as sensor location and target geometry. However, what is evident from the double derivative is that this information is *coupled.* The phase varies with time, space, frequency *and* the location of the scatterer. However, the only scatterer-dependent parameters that affect how the received phase varies over the sensor are the x, y and z coordinates of the target position (scatterer). Since the target has only three variables that affects its response at the radar, we can say that we need only three sensor dimensions to represent the SAR data. Thus, the hypothesis is that although the phase varies with respect to five sensor parameters, those sensor parameters can be projected into the coordinates of three independent *eigensensors,* and this concept will be discussed in detail in the next section.

2.3 The 3D Synthetic Aperture – Eigen Sensor Analysis

Eigensensor analysis basically refers to the problem of finding a coordinate system in which the solution to a given problem has a simple expression. Several

aspects of distributed radar systems make effective signal processing problematic. The most significant of these is the characteristics of the spatial array, which provides both a sparse and a random sampling over a large volume. Moreover, the sensor look angle will not be typically perpendicular to the direction of sensor velocity (leading to a non-zero squint angle), so that isorange and isodoppler contours will not be perpendicular, nor will they align with the traditional cross-track and along-track directions. Consequently, traditional radar tools and signal processing algorithms are not applicable to the sparse array concept. The distributed system collects information as a function of frequency, time and three spatial dimensions but the sampling in these five dimensions is aperiodic and each measurement provides independent but coupled information about any and all target dimensions.

A very useful tool for organizing and analyzing the information collected by a distributed system is the *eigensensor analysis* [1]. Using this technique, we can separate out the distributed radar measurements into their fundamental components, so that sensor behavior and signal processing can be accurately determined. The construction of the eigensensor begins with the phase function $\psi(\overline{s}_{ik'}; \overline{y}_t)$ of the field scattered from a stationary target located at $\overline{y}_t$. Assuming that the target is illuminated by a modulated form of a carrier signal $\exp\{j\omega_o t\}$, this scattered phase function can be written in terms of the five-dimensional measurement vector $\overline{s}_{ik'}$ mentioned in the previous section. As already shown, this vector describes the five radar measurement dimensions time *t*, relative frequency $\omega_r = \omega - \omega_o$ and the three

dimensions of space which define the spatial location of the receive elements. If we expand this phase function as a Taylor series around the center of the radar measurement $\bar{s}_o$ and then retaining only the first two terms gives a far-field approximation for the scattered phase [1]:

$$\psi(\bar{y}_t, \bar{s}_{ik'}) \approx \psi(\bar{y}_t, \bar{s}_o) + \nabla_s \psi \,|_{\bar{s}_o} \; \Delta\bar{s}$$

$$= \left.\frac{\partial \psi(\bar{y}_t, \bar{s}_{ik'})}{\partial x_i}\right|_{\bar{s}_o} x_i + \left.\frac{\partial \psi(\bar{y}_t, \bar{s}_{ik'})}{\partial y_i}\right|_{\bar{s}_o} y_i + \left.\frac{\partial \psi(\bar{y}_t, \bar{s}_{ik'})}{\partial z_i}\right|_{\bar{s}_o} z_i + \left.\frac{\partial \psi(\bar{y}_t, \bar{s}_{ik'})}{\partial \omega}\right|_{\bar{s}_o} \omega_r + \left.\frac{\partial \psi(\bar{y}_t, \bar{s}_{ik'})}{\partial t}\right|_{\bar{s}_o} t$$

$$= k_x(\bar{y}_t)x_i + k_y(\bar{y}_t)y_i + k_z(\bar{y}_t)z_i + \tau(\bar{y}_t)\omega_r + \omega_D(\bar{y}_t)t \tag{2.21}$$

The five derivative operators provide the five measurements associated with the radar sensor.

Delay $\tau(\bar{y}_t)$ is given by the change in phase with respect to ω_r.

Doppler $\omega_D(\bar{y}_t)$ is given by the change in phase with respect to time, *t*.

k_x, k_y, k_z represent the spatial frequencies

On the whole, all these five target "frequencies" can be expressed as a vector as shown below.

$$\mathbf{E}(\bar{y}_t) = \begin{bmatrix} k_x(\bar{y}_t) & k_y(\bar{y}_t) & k_z(\bar{y}_t) & \tau(\bar{y}_t) & \omega_D(\bar{y}_t) \end{bmatrix} \tag{2.22}$$

The main problem with this arrangement is that each of the five frequencies is dependent on all the three target dimensions and therefore we could say that each of the five sensor measurements in $\bar{s}_{ik'}$ provides information about every dimension of

the target location $\bar{y}_t$. Therefore what is required is some sort of "decoupling" in the sensor measurements so that useful information could be extracted out of the radar response data.

Thus, in order to interpret the transformation matrix in a better fashion, it is written in terms of its singular value decomposition (SVD). As seen from (2.19), $\bar{\bar{K}}_\varphi$ is a three-dimensional matrix with the three rows corresponding to the three target dimensions (third dimension being height). When expanded in terms of its SVD,

$$\bar{\bar{K}}_\varphi = \bar{\bar{U}} * \bar{\bar{S}} * \bar{\bar{V}}^T \tag{2.23}$$

where

$$\bar{\bar{U}} = \begin{bmatrix} \bar{u}_1 & \bar{u}_2 & \bar{u}_3 \end{bmatrix} \qquad \text{(3 x 3 matrix)}$$

$$\bar{\bar{S}} = \begin{bmatrix} \sigma_1 & 0 & 0 & 0 & 0 \\ 0 & \sigma_2 & 0 & 0 & 0 \\ 0 & 0 & \sigma_3 & 0 & 0 \end{bmatrix} \qquad \text{(3 x 5 matrix)}$$

$$\bar{\bar{V}} = \begin{bmatrix} \bar{v}_1 & \bar{v}_2 & \bar{v}_3 & \bar{v}_4 & \bar{v}_5 \end{bmatrix} \qquad \text{(5 x 5 matrix)} \tag{2.24}$$

While the S matrix consists of the non-singular values resulting from the decomposition, the columns of the matrix $\bar{\bar{U}}$ consist of the eigen vectors of $\bar{\bar{K}}_\varphi{}^T \bar{\bar{K}}_\varphi$ and the columns of the matrix $\bar{\bar{V}}$ consists of the eigen vectors of $\bar{\bar{K}}_\varphi \bar{\bar{K}}_\varphi{}^T$. The symbol '*' denotes the multiplication operation.

We could also express the result of the SVD as

$$\bar{\bar{K}}_\varphi = \sum_{i=1}^{3} \sigma_i \bar{u}_i \bar{v}_i^T \tag{2.25}$$

where $\bar{u}_i$ are three-dimensional and $\bar{v}_i$ are five-dimensional orthonormal vectors. Analysis of the propagation matrix in the measurement space enables us to obtain the *eigensensors.* We proceed by simplifying the far-field phase expression into scalar terms.

$$\psi(\bar{s}_{ik}, \bar{y}_t) \approx \kappa_0^T \bar{s}_{ik} + \bar{s}_{ik}^T \bar{\bar{K}}_{\varphi}^T \bar{y}_t \tag{2.26}$$

where K_ψ represents the frequency matrix or transformation matrix which relates the receive signal space to the target position space.

Using (2.25), (2.26) can now be written as,

$$\psi(\bar{s}_{ik}', \bar{y}_t) = \kappa_o^T \bar{s}_{ik}' + (\bar{s}_{ik}^T, \bar{v}_1 \sigma_1)(\bar{u}_1^T \bar{y}_t) + (\bar{s}_{ik}^T, \bar{v}_2 \sigma_2)(\bar{u}_2^T \bar{y}_t) + (\bar{s}_{ik}^T, \bar{v}_3 \sigma_3)(\bar{u}_3^T \bar{y}_t)$$

$$= \kappa_o^T \bar{x}_{ik} + \kappa_\alpha \alpha + \kappa_\beta \beta + \kappa_\gamma \gamma \tag{2.27}$$

The result shows that a complex sensor can be represented in terms of three decoupled measurements, which are referred to as *eigensensors*. The scalar value $\alpha_t = \bar{u}_1^T \bar{y}_t$ is used to provide information only about the target frequency $\kappa_\alpha = \bar{s}_{ik}^T, \bar{v}_1 \sigma_1$, which is a scalar value dependent on the target position in the direction of $\bar{v}_1$ only. A similar relationship exists between measurement β, target frequency κ_β and the direction $\bar{v}_2$ as well as the measurement γ, target frequency κ_γ and the direction $\bar{v}_3$. The eigen vectors $\bar{u}_i$ and $\bar{v}_i$, therefore, form a very good basis for our radar problem. The measurements α, β and γ are determined by projecting the sensor measurement vector $\bar{s}_{ik}'$ on to $\bar{v}_i$ while the target frequencies $\kappa_{\alpha,}, \kappa_\beta$ and κ_γ are determined by projecting the target position vector $\bar{y}_t$ on to the eigen space defined by $\bar{u}_i$.

2.4 Eigensensor Simulations

It is clear from the previous section that we can project a five-dimensional radar measurement space into a three-dimensional *measurement eigen space* or *eigensensor space.* Similarly, the physical target space can be replaced by an equivalent three-dimensional *eigen target space*. Figure 2-2 depicts the two-dimensional eigen space representation of a sparse radar array consisting of 8 receive antennas with 17 time samples and 31 frequency samples. The z dimension of the target location is ignored because of which the target space is two-dimensional and this leads to a two-dimensional eigensensor space. Figure 2-3 depicts an equivalent three-dimensional eigensensor which results if the target space is three-dimensional in nature (target height also considered).

The result of such a projection on to the new *eigensensor* coordinates is that we obtain a measurement scenario, which is analogous to the far-field approximations carried out for the standard side-looking SAR. One sensor measurement (relative frequency) provides information only about one target frequency (delay), which is a function of target position in one direction (cross-track), while a second measurement (time) provides information only about the second target frequency (doppler), which is a function of the target position in an orthogonal direction (cross-track). At the same time, this design also collects data across one spatial dimension to provide information about a third target frequency that is a function of the target position in the vertical direction (height).

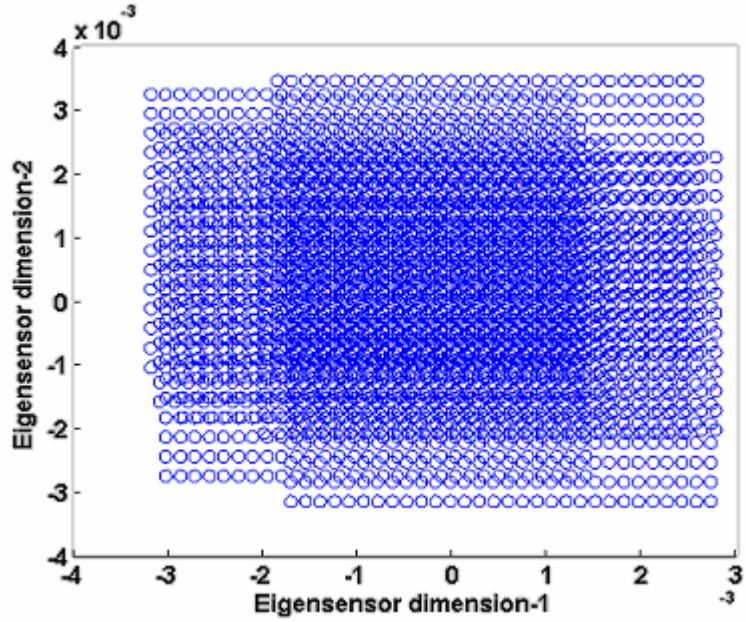

Figure 2-2 Two dimensional Eigensensor array for a small microsat constellation consisting of 8 receive antennas.

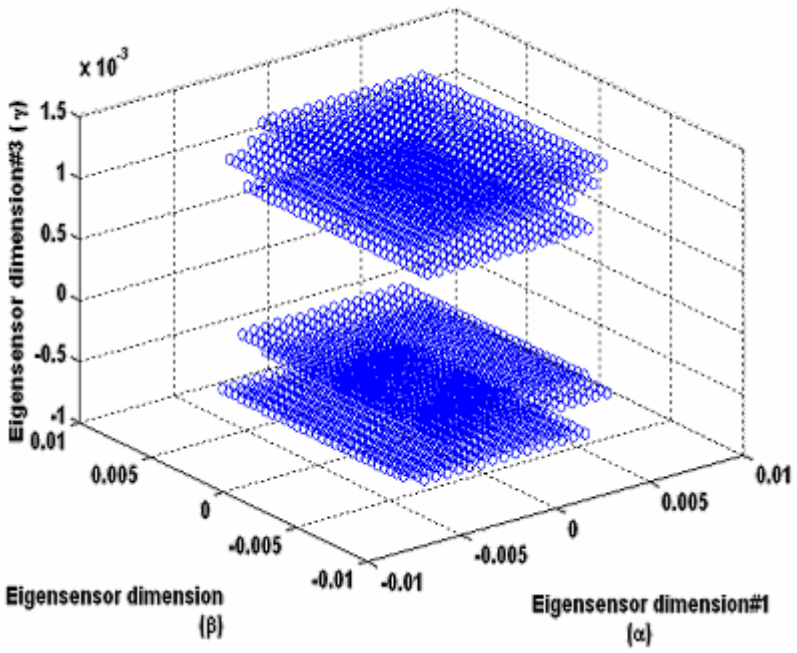

Figure 2-3 Measurement space completely characterized by a three-dimensional Eigensensor space representing 8 receive antennas where each antenna receives 17 time samples and 31 frequency samples

Thus, the strength of this decomposition is that it can be used to transform the distributed radar problem into a form where the analysis is clear and well defined.

In this chapter, we have successfully looked at how to simulate the radar response vector by developing a software model and then showed how to utilize the concepts of eigensensor analysis to convert the sparse radar array problem to a form which can be easily applied to interferometry. The next chapter deals with the design and implementation of the SAR (Kalman) processor

3. KALMAN FILTER

3.1 Significance of the Kalman filter design

There has been significant research carried out related to development of algorithms for processing of the sparsely populated multiple aperture spaceborne radar [1,3,13]. [3] specifically deals with the application of the Kalman filtering technique for SAR processing of sparse satellite clusters and comparison of its results with the other estimation techniques. Some of the algorithms that were initially used for this purpose were the matched filter, the maximum-likelihood filter and the minimum mean-squared error filter [13]. Even though the matched filter is able to maximize the received energy with respect to noise, it is unable to minimize the error due to the presence of clutter in target response. *Clutter* basically refers to any objects that cause unwanted reflections of a radar's electromagnetic energy to be returned to the radar receiver. These unwanted returns interfere and compete with the valid returns of interest and cause the radar response to become cluttered and difficult to decipher. In the SAR scenario that we consider, all the target resolution cells surrounding the target of interest are said to constitute clutter. This is because, if we are estimating the scattering coefficient of a specific target pixel, we do not wish to receive any responses from the surrounding pixels. Thus, if the responses from the illuminated targets are significantly correlated, a very large error will result. Generally, in the case of the sparse arrays, the responses of all surrounding resolution

cells will be correlated to a great extent and hence a different linear processor must be implemented.

The maximum likelihood (ML) estimator has the ability to minimize the error due to clutter but does nothing to reduce the interference due to noise. As a result, the estimation error degrades rapidly with any decline in the measurement SNR. Now, if we possess some *a priori* knowledge of the radar transmit power and noise figure, then a minimum mean squared error estimator can be implemented. The MMSE estimator is a discrete implementation of a Wiener filter and minimizes the error due to both noise and clutter. In other words, if the matched filter maximizes signal to noise and the ML estimator maximizes signal to clutter, the MMSE estimator can be said to maximize signal to interference. We can therefore say that the MMSE filter is the mathematically optimum compromise between the correlation and the ML filters.

The biggest disadvantage of an MMSE filter is that a matrix inverse operation that appears in one of the intermediate steps can be impractically large for many radar problems and this can slow down the computing speed drastically. The solution to this problem is that the MMSE estimate can be computed iteratively wherein the data vector is split into smaller segments in order to reduce the processing time. This leads to the *Kalman Filter* algorithm. The Kalman filter is an iterative implementation of the MMSE estimator [3]. We can implement it by operating on sections of the radar response vector $\mathbf{r}$, rather than on the entire length of the vector. Before using the Kalman processor for applications involving interferometry, we need to test the efficacy of the algorithm and the accuracy of its estimation, and that forms the focus

of this chapter. The following sections provide a detailed explanation regarding the theory behind Kalman filter design, its implementation and analysis of the results obtained.

3.2 Kalman Filter Theory

In 1960, R.E Kalman presented the set of recursive equations that have come to be known as the Kalman Filter. However there were several other major developments that actually preceded the introduction of the Kalman Filter. R.A Fischer initially introduced the idea of maximum likelihood estimation. This approach was followed by Kolmogorov in 1941 and Wiener in 1942, when they independently developed a linear minimum mean-square estimation technique that received considerable attention and provided the foundation for the subsequent development of the Kalman filter theory [18].

In simple words, we could say that the purpose of a Kalman filter is to estimate the state of a system from a set of measurements, which contain random errors or noise. The system is said to be composed of two essential parts, the state or process equation and the measurement or observation equation. In state-space notation, the *state equation* or the *process equation* models the expected variation in the parameter $\mathbf{x}(k)$, which is to be estimated. It is given by,

$$\mathbf{x}(k) = \mathbf{A}(k)\mathbf{x}(k) + \mathbf{b}(k) \tag{3.1}$$

As mentioned earlier, $\mathbf{x}(k)$ is the parameter which is to be estimated while $\mathbf{A}(k)$ is known as the state transition matrix which models the expected variation in the value

of **x***(k)* from *k-1* to *k*. In other words, the state transition matrix relates the state at a previous step *k-1* to the state at the current step *k*. **b***(k)* represents the process noise and conveys the uncertainty in the modeling of this expected variation.

The *observation* or *measurement equation* is given by

$$\mathbf{z}(k) = \mathbf{H}(k)\mathbf{x}(k) + \mathbf{v}(k) \tag{3.2}$$

Here, **H***(k)* describes the relationship between the signal vector **x***(k)* and the observation vector **z**(*k*) while **v**(*k*) represents the measurement noise.

With respect to the above equations, we can state that the Kalman filter process basically involves optimally solving (3.1) and (3.2) and thereby utilizing the entire set of observed data contained in **z***(k)* to obtain the minimum mean-square estimate of the parameter **x.** The complete algorithm as well as the application to a radar scenario will be discussed in the next section.

3.3 Application to the Radar scenario

Although the Kalman filter algorithm is usually described from the point of view of application to time-varying, dynamic systems, we can just the same apply it to static systems. Hence, this algorithm is very useful for our radar scenario. We call the radar application a static one because we assume that the state vector containing the *scattering coefficient of the target resolution cells*, which is the parameter to be estimated, remains approximately constant with respect to time, space and frequency over the extent of the radar measurement.

As seen from (2.7), the radar response vector is given by the following equation,

$$\mathbf{r} = \sum_{t}^{N_t} \gamma_t \boldsymbol{\rho}_t + \mathbf{n} \tag{3.3}$$

It is clear from the above equation that the response vector is given by the sum of the weighted responses of all illumination targets with the included effect of noise. From (2.9)

$$\mathbf{r} = \mathbf{P}\boldsymbol{\gamma} + \mathbf{n} \tag{3.4}$$

where,

$$\boldsymbol{\gamma} = \begin{bmatrix} \gamma_1 & \gamma_2 & \gamma_3 & \cdots & \gamma_T \end{bmatrix} \tag{3.5}$$

and

$$\mathbf{P} = \begin{bmatrix} \boldsymbol{\rho}_1 & \boldsymbol{\rho}_2 & \boldsymbol{\rho}_3 & \cdots & \boldsymbol{\rho}_{N_t} \end{bmatrix} \tag{3.6}$$

Our final objective is to estimate the scattering coefficient $\boldsymbol{\gamma}$ given the radar response vector **r**. We could achieve the same by using any linear estimator, which can be written as,

$$\hat{\boldsymbol{\gamma}} = \mathbf{T}\,\boldsymbol{\gamma} \tag{3.7}$$

where

$\hat{\boldsymbol{\gamma}}$ is the estimate of the complex scattering coefficient $\boldsymbol{\gamma}$

T is a matrix that describes the linear estimator

For the Linear Minimum Mean-squared or Wiener estimator, **T** is given by [3],

$$\mathbf{T}_{MMSE} = \mathbf{K}_{\gamma}\mathbf{P}^{T}[\mathbf{P}\mathbf{K}_{\gamma}\mathbf{P}^{T} + \mathbf{K}_{n}]^{-1} \tag{3.8}$$

where

$\mathbf{K}_{\gamma}$ is given by $E\left\{\boldsymbol{\gamma}\boldsymbol{\gamma}^{T}\right\}$

$\mathbf{K}_{n}$ is given by $E\left\{\mathbf{n}\mathbf{n}^{T}\right\}$

As mentioned earlier, the main problem that we face when implementing this estimator is the inverse operator that appears in (3.8). This inversion operation can be very large for several radar problems and is a potential stumbling block when it comes to computation. The solution to this problem is the Kalman filter algorithm.

We can take the radar response vector and split it up into, say, L vectors each with a dimension of 5 (as an example). It should however be noted that the length of the segments is arbitrary and can be as small as 1. The segmented response vector looks as shown below,

$$\mathbf{r} = \left[\underbrace{r_1 \quad r_2 \quad r_3 \quad r_4 \quad r_5}_{r(1)} \quad \underbrace{r_6 \quad r_7 \quad r_8 \quad r_9 \quad r_{10}}_{r(2)} \quad \ldots\ldots \quad \underbrace{r_{M-4} \quad r_{M-3} \quad r_{M-2} \quad r_{M-1} \quad r_M}_{r(L)} \right] \tag{3.9}$$

Equivalently, we can also segment the matrix **P**, which is a collection of the normalized response vectors corresponding to all targets, into smaller pieces.

$$\mathbf{P} = \left[P^{T}(1) \quad P^{T}(2) \quad P^{T}(3) \quad \ldots. \quad P^{T}(L) \right]^{T} \tag{3.10}$$

Finally, we can segment the noise vector as shown below,

$$\mathbf{n} = \left[n(1) \quad n(2) \quad n(3) \quad .... \quad n(L) \right] \tag{3.11}$$

The parameter that is to be estimated in this case is $\boldsymbol{\gamma}$ and **r** is the observation vector. Thus, in case of this radar problem, we can refer to (3.1) and define the *process* or *state equation* as,

$$\boldsymbol{\gamma}(l) = \mathbf{A}(l)\boldsymbol{\gamma}(l-1) + \mathbf{u}(l) \tag{3.12}$$

where **A***(l)* is the state transition matrix as described in (3.1) and **u***(l)* is process noise which represents the uncertainty in **A***(l)*.

Equation (3.4) gives the relationship between the measurement vector and the state vector and therefore it is very similar to the *observation equation* given in (3.2). Hence, the observation equation for the radar scenario can be defined as,

$$\mathbf{r}(l) = \mathbf{P}(l)\boldsymbol{\gamma}(l) + \mathbf{n}(l) \tag{3.13}$$

where l represents the iteration number or the section of data (out of a total of L sections of data) on which the processing is being done.

A change in the value of l corresponds to a change in a set of radar measurements, which are collected over time, space and frequency. We start by assuming that the scattering coefficients are constant with respect to these three parameters of measurement. Thus $\mathbf{A}(l)$ is an identity matrix. The following "initial values" are chosen as an input to the algorithm.

$$\begin{aligned}
&\hat{\boldsymbol{\gamma}}(0/0) = E\{\boldsymbol{\gamma}\} = 0 \\
&\mathbf{K}_{\gamma}(0/0) = \sigma_{\gamma}^2 \overline{\overline{I}} \\
&\mathbf{K}_{n}(0/0) = \sigma_{n}^2 \overline{\overline{I}} \\
&\mathbf{K}_{u}(l) = 0
\end{aligned} \tag{3.14}$$

The Kalman filter algorithm can be described as follows:

Step 1: The estimated scattering coefficient $\hat{\boldsymbol{\gamma}}(l-1/l-1)$ and the error covariance matrix of the scattering coefficients, $\mathbf{K}_{\gamma}(l-1/l-1)$, are known after processing the previous step.

Step 2: Initially, the *a priori* error covariance matrix is obtained as follows

$$\mathbf{K}_{\gamma}(l/l-1)=\mathbf{K}_{\gamma}(l-1/l-1)+\mathbf{K}_{u}(l) \tag{3.15}$$

where $\mathbf{K}_{u}(l)$ is the covariance matrix of the noise process **u** and its value is taken as zero.

Step 3: The Kalman gain matrix is then computed. This calculation of the Kalman gain is carried out with the objective of minimizing the effect of the error covariance matrix of the scattering coefficients $\mathbf{K}_{\gamma}(l)$. The process ensures that the mean square error is minimized, which based on the orthogonality theorem occurs when the error in the estimate is orthogonal to the measurement data [3]. Thus we have,

$$\mathbf{G}\left(l\right)=\mathbf{K}_{\gamma}(l/l-1)\mathbf{P}^{T}(l)[\mathbf{P}(l)\mathbf{K}_{\gamma}(l/l-1)\mathbf{P}^{T}(l)+\mathbf{K}_{n}(l)]^{-1} \tag{3.16}$$

In the above equation, $\mathbf{G}\left(l\right)$ is the *Kalman gain*.

Step 4: (*Innovation process*): This step involves the computation of the error between the observed measurement and the predicted measurement. The error value obtained is called the *innovation.*

$$\mathbf{v}(l)=\mathbf{r}(l)-\mathbf{P}(l)\hat{\boldsymbol{\gamma}}(l-1/l-1) \tag{3.17}$$

where $\mathbf{v}(l)$ is the innovation value. This value refers to some *new information* that is required for the next step of estimation. In other words, the *innovation* reflects the

discrepancy between the predicted measurement $(\mathbf{P}(l)\hat{\boldsymbol{\gamma}}(l-1/l-1))$ and the actual measurement $(\mathbf{r}(l))$. A residual of zero would mean that the two are in complete agreement and we have no further *new information,* which in turn would mean that we have reached the end of the estimation process. The *innovation*, which forms the essence of the Kalman Filtering Theorem, is orthogonal to all the past observations and could be used to make an optimal estimate of $\boldsymbol{\gamma}$ [3]**.**

Step 5: The final objective in the Kalman process is to find the estimate $\hat{\boldsymbol{\gamma}}(l/l)$ as a linear combination of an *a priori* estimate $\hat{\boldsymbol{\gamma}}(l-1/l-1)$ and a weighted difference between the actual measurement and a measurement prediction, which is defined by the product of the *Kalman gain* and the *innovation*. Thus, a new estimate value is obtained using the previously calculated Kalman gain and the innovation value.

$$\hat{\boldsymbol{\gamma}}(l/l) = \hat{\boldsymbol{\gamma}}(l-1/l-1) + \mathbf{G}(l)\mathbf{v}(l) \tag{3.18}$$

where $\hat{\boldsymbol{\gamma}}(l/l)$ is the new MMSE estimate of $\hat{\boldsymbol{\gamma}}$ given $\mathbf{r}(l)$.

From (3.16) and (3.18), it is interesting to see that as the measurement error covariance $[\mathbf{K}_n(l)]$ approaches zero, the Kalman gain weights the innovation more heavily. On the other hand, if the estimate error covariance $[\mathbf{K}_\gamma(l)]$ approaches zero, then the Kalman gain weights the innovation less heavily. In other words, as the measurement error covariance approaches zero, the actual measurement **r** is "trusted" more and the predicted measurement is trusted less. This process helps us move closer to the correct estimate.

Step 6: The updated error correlation matrix is then given by

$$\mathbf{K}_{\gamma}(l/l) = [\mathbf{I} - \mathbf{G}(l)\mathbf{P}(l)]\mathbf{K}_{\gamma}(l/l-1) \tag{3.19}$$

At the end of the last step we have $\hat{\boldsymbol{\gamma}}(l/l)$ and $\mathbf{K}_{\gamma}(l/l)$. Repeating the iteration once more would produce $\hat{\boldsymbol{\gamma}}(l+1/l+1)$ and $\mathbf{K}_{\gamma}(l+1/l+1)$.

The entire Kalman filter algorithm is repeated until all the radar measurements have been utilized and good estimates are obtained. The next section deals with implementation of the Kalman Filter algorithm so that it can be used to obtain an estimate of target scattering coefficients given a set of radar measurements.

3.4 Kalman Filter – Performance Analysis

In order to test the efficacy of the developed Kalman filter, a series of tests were carried out with sets of randomly chosen scattering coefficients. This section aims at outlining some important factors to be considered while setting up the algorithm and analyzing its performance.

3.4.1 Selecting physical parameters for the Radar model

One very important criteria when it comes to forming SAR images is the minimum number of spatial receive elements and hence the number of receive time-frequency samples that are required to unambiguously estimate the scattering coefficients corresponding to the target image pixels. Hence, a systematic approach was followed to decide on the various physical parameters that were provided as inputs to the SAR simulator. For the test under consideration, all the targets were taken to be arranged in the form of a two-dimensional square grid of dimension N_x *by*

N_y where N_x is the number of resolution cells in the x-direction while N_y refers to an equal number of resolution cells in the y-direction. If Δx is the resolution along the x-direction and Δy is the resolution along the y-direction, then we can denote the target position vectors as

$$\bar{y}_t = [n_x * \Delta x, n_y * \Delta y, z_t, v_t] \tag{3.20}$$

where $-\left(\frac{N_x - 1}{2}\right) \le n_x \le \frac{N_x - 1}{2}$ and $-\left(\frac{N_y - 1}{2}\right) \le n_y \le \frac{N_y - 1}{2}$

The resolution of the radar was chosen to equal in both along-track and cross-track directions, which caused the resolution cells to be square. This condition helps us to set a first constraint on the ratio of Bandwidth B to the Time width, T. The radar resolution in the x-direction is given by the following equation [4],

$$\Delta x = \frac{cR_o}{2UT_o v_x f_c} \tag{3.21}$$

where

f_c - center frequency of the transmit signal

U – number of time samples

T_o – signal repetition interval

v_x – radar velocity

R_o- radar range

Similarly, the resolution in the y-direction, for the considered scenario, is given by

$$\Delta y = \frac{c}{2B \sin \theta_i} \tag{3.22}$$

where

B is the bandwidth

c is the velocity of light

θ_i is the tilt angle

By using the condition that the resolution is equal in both directions and then re-arranging (3.21) and (3.22) we reach a constraint on the B/T ratio given by

$$\frac{B}{T} = \frac{vf_c}{y_o} \tag{3.23}$$

The above equation is termed the "*square pixel constraint equation*".

A necessary condition for unambiguously imaging all resolution cells is that the number of independent measurement samples should be greater than the number of resolution cells. This requirement is defined by an important radar parameter called *clutter rank,* which is effectively equal to the number of resolution cells (given by $Nx * Ny$) in a SAR image. Now, since the number of independent measurement samples is approximately equal to $I*B*T$, where I is the number of spatial receive elements, we find that unambiguous imaging can result only when,

$$I * B * T > Nx * Ny \tag{3.24}$$

In order to establish a convenient rule for deciding on the minimum number of spatial receive elements I required for accurate estimation, we define a parameter that is given by the ratio of the total number of resolution cells to the signal time-bandwidth product. This parameter is called β and it is given by [4],

$$\beta = \frac{N_x N_y}{BT} \tag{3.25}$$

For a single aperture radar, this value should be less than or equal to 1 in order to ensure unambiguous imaging. However, for multi-aperture radar, this value can be greater than one, provided the number of receive antennas is sufficient. For example, the value of β was chosen as 4.2 for all the simulations carried out in this section. This means that the time-bandwidth product *using only one antenna* is sufficient to unambiguously image only around 25% of the original image. In order to get better estimates, we would need to increase the number of receive antennas. Thus, we see that the value for β sets the lower bound on the number of required antennas.

Comparing (3.18) and (3.19), we find that,

$$I > \beta = \frac{N_x N_y}{BT} \tag{3.26}$$

This confirms our earlier premise that the number of spatial receive elements should be greater than the value of β in order to obtain good estimates.

The physical extent of the arrays is usually too small to resolve the resolution cells and therefore resolution is mainly determined by the temporal values of the signal bandwidth and time width. If the spatial extent of the array in the along track direction is L_x, then the approximate width of the main beam is given by:

$$\Delta X_s = \frac{cR_0}{f_c L_x} \tag{3.27}$$

We can now define a parameter η which represents the ratio of the spatial resolution to the temporal resolution i.e.

$$\eta = \frac{\Delta X_s}{\Delta x} \tag{3.28}$$

For all the simulations carried out in this thesis, the value of η was taken as 5 which means that the width of the main antenna beam is approximately five times the resolution along the x-direction.

One module in the radar model was devoted to assigning the various input parameters that could be utilized while simulating the response data. Some of these input values, which were common to all the tests, are summarized in Table 3-1. These values are consistent with a spaceborne radar in low-Earth orbit.

Radar System height	183 km
Radar velocity	780 m/s
Tilt angle (θ_i)	0.7854 radians (45 degrees)
Radar Range	259 km
Pulse repetition frequency (prf)	20.65 KHz
Center frequency of transmit signal	10 GHz

Table 3-1 Set of values chosen as input to the SAR simulator

3.4.2 Test 1 – Randomly chosen scattering coefficients

The first test that was carried out establishes the efficacy of the Kalman filter. The scattering coefficient values that were used to form the image were assigned random magnitude and phase values. The other input parameters were assigned in accordance with Table 3-2.

The performance of the Kalman Filter is expressed in terms of the variation in error versus the fraction of data processed [3]. The error criterion, which serves as a good indicator of estimation accuracy, is the Mean-squared error (MSE) μ of pixel magnitudes normalized by the image's mean-squared pixel magnitude. We have,

$$\mu = \frac{(\hat{\gamma} - \gamma)^H (\hat{\gamma} - \gamma)}{(\gamma^H \gamma)} \tag{3.29}$$

The fraction of measurement vector processed, ε, is given by,

$$\varepsilon = \frac{\mathrm{l}}{\mathrm{L}} \tag{3.30}$$

Where l is the number of measurement vectors processed by the Kalman Filter out of a total of L vectors. In (3.29), ^{H} denotes a conjugate transpose operation.

Number of receive elements (antennas)	8
Number of along/cross-track target pixels	31
Number of time samples	15
Number of frequency samples	31
Total number of samples/receive antenna	465
Length of aperture	2.286 m
Along-track target resolution	679.3 m
Cross-track target resolution	679.3 m

Table 3-2 Input parameters unique to Test 1

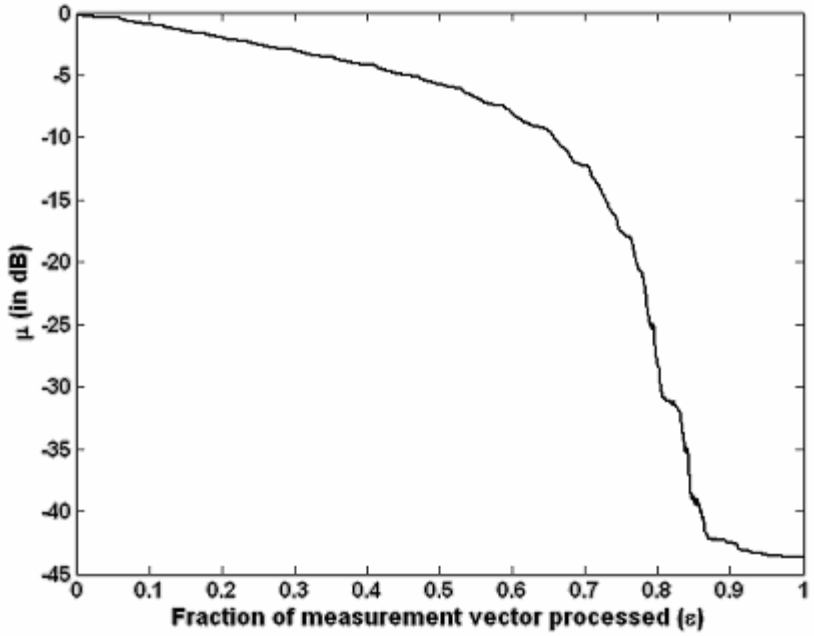

Figure 3-1 Performance of the Kalman Filter – MSE versus ε

Figure 3-1 provides information about the variation of μ with respect to ε. The final estimate obtained after all the measurements have been processed is identical to the actual image, which explains the low value of MSE provided by the Kalman Filter.

3.4.3 Test 2 – Results

This section deals with displaying the results obtained when the Kalman filter was tested with a more realistic scenario. Figure 3-2(a) shows the input image provided to the simulator. The image shows a view of the University of Kansas Memorial stadium in Lawrence, Kansas and was cropped and converted to a 31-by-31 resolution image. The pixel intensities were assigned a random phase value and the resulting set of complex scattering coefficients was used as one of the input vectors to

the SAR simulator. Table 3-3 shows the various parameter values assigned during this simulation.

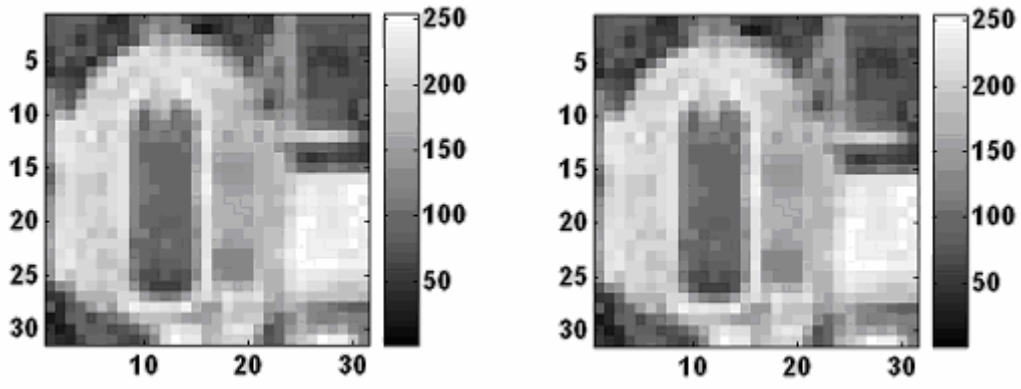

(a) Actual Image **(b) Estimated Image**

Figure 3-2 Kalman Filter Performance – Comparison of actual and estimated SAR images

Number of receive elements (antennas)	8
Number of along-track target pixels	31
Number of cross-track target pixels	31
Number of time samples	15
Number of frequency samples	31
Total number of samples/receive antenna	465
Length of aperture	2.286 m
Along-track target resolution	679.3 m
Cross-track target resolution	679.3 m

Table 3-3 Input parameters unique to Test 2

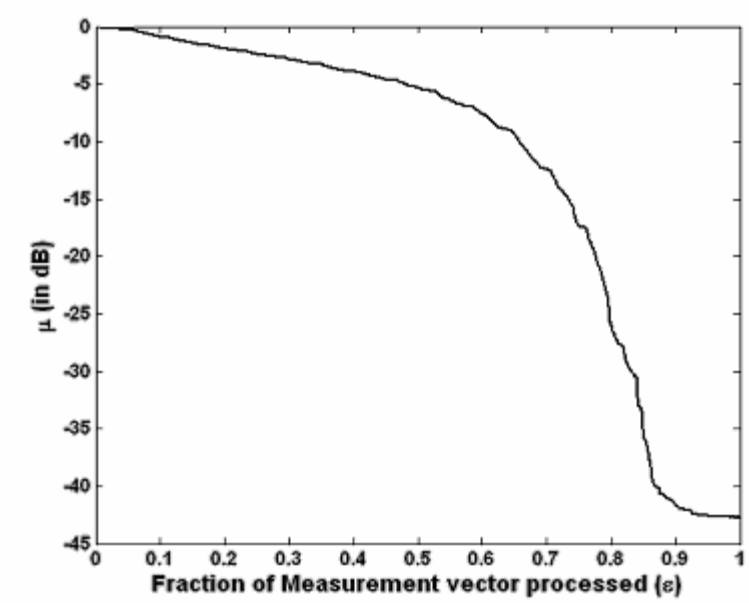

Figure 3-3 Performance of Kalman Filter while estimating KU Football stadium image

Figure 3-3 is similar to Figure 3-2 and depicts a plot of μ versus ε. The Kalman Filter algorithm gives a final MSE of almost -43 dB which is indicative of very good estimation. Figure 3-4 shown on the next page gives us some insight into how the Kalman Filter proceeds through its iterations while estimating the scattering coefficient values.

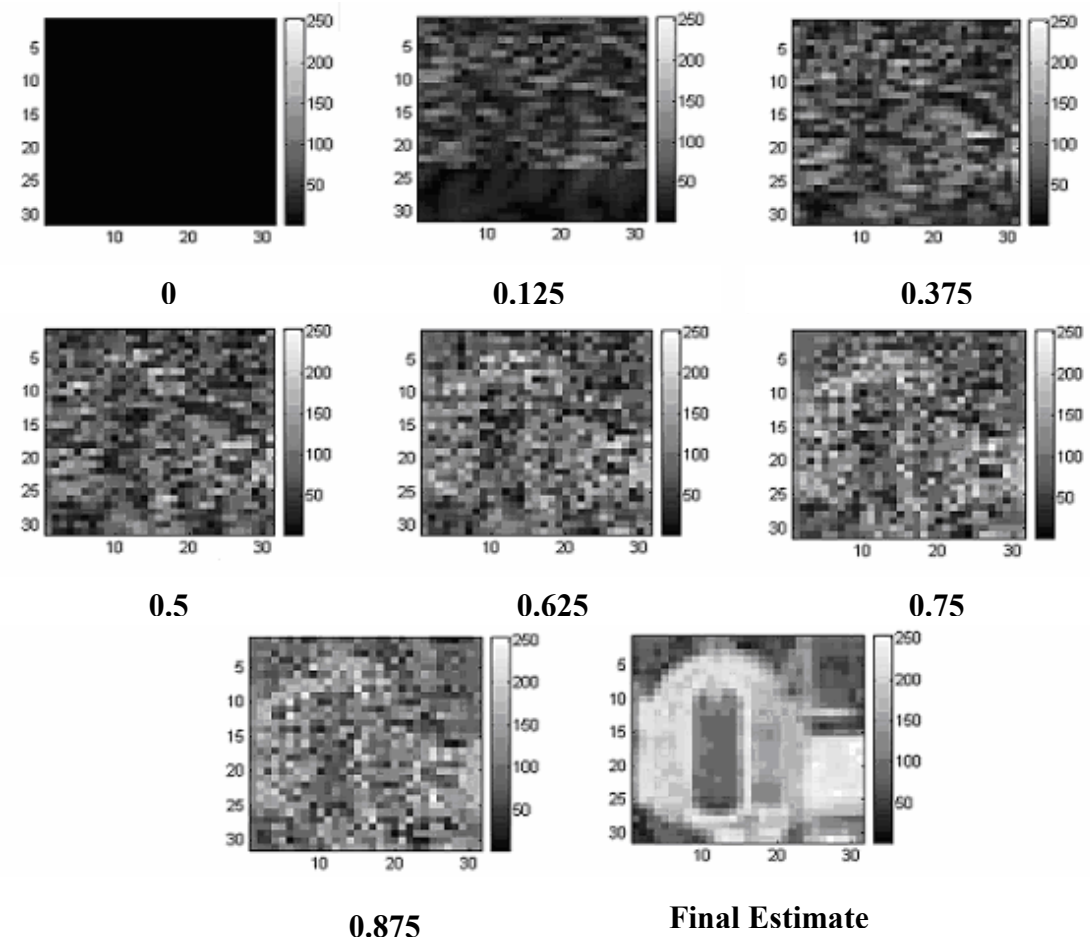

Figure 3-4 Performance of the Kalman Filter- Estimates obtained during intermediate iterations of the Kalman filter algorithm. The numbers below each figure indicate the fraction of the measurement vector that has been processed up to that stage of estimation

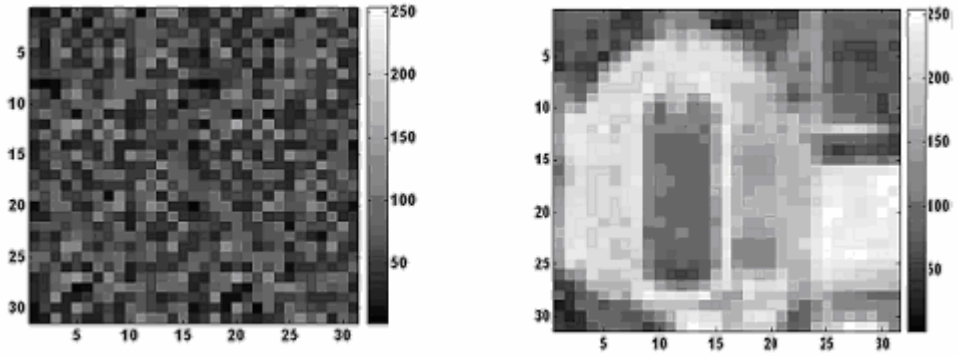

(a) With 1 receive aperture **(b) With 8 receive apertures**

Figure 3-5 Indicates need for multiple apertures

Another purpose of this test is to display the need for multiple receive apertures to enhance the quality of estimation. Figure 3-5(a) shows a SAR image formed using only one receive antenna while Figure 3-5(b) shows the SAR image formed using multiple (eight) receive antennas. It is quite obvious from the above result that having only one receive aperture provides a low time-bandwidth product and hence an insufficient number of time-frequency samples to accurately form a SAR image. Thus, as mentioned at the beginning of this section, this test strengthens the case for a *multi-aperture* system and also depicts the application of the Kalman Filter to a radar scenario. The Kalman filter thus forms a very efficient SAR processor and provides a robust and accurate way to form accurate SAR images. The next step is to look at the application of this tool to SAR interferometry, a technique which forms the core of this thesis.

4. TOPOGRAPHY ESTIMATION USING DISTRIBUTED RADAR ARRAY MEASUREMENTS

This chapter deals with a detailed discussion of the concepts leading to a *topography-estimation algorithm*, which will be applicable to a distributed radar design concept.

We will begin by looking at the conventional topographic SAR, briefly discuss why the traditional interferometric techniques do not apply to the distributed concept and then move on to a detailed analysis of the methodology useful for height estimation using distributed radar array measurements.

4.1 Conventional Topographic SAR

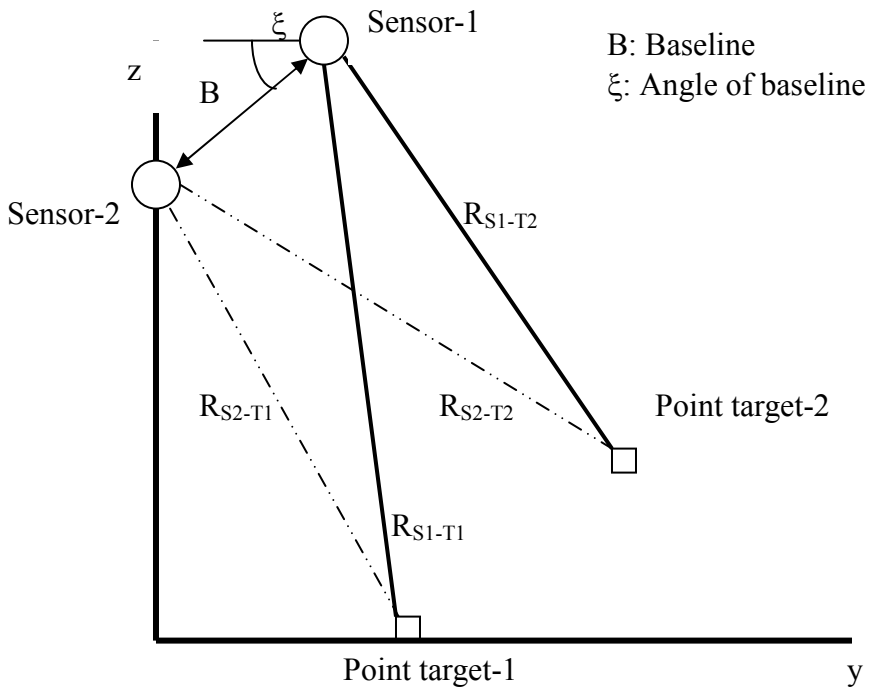

Figure 4-1 SAR Interferometry – basic geometry [2]

The conventional TopSAR technique makes use of the phase differences between two complex SAR images of the same scene acquired from two spatially separated locations, either by using two antennas in a single-pass mode or a single antenna in a repeat-pass mode. A simple implementation of a SAR interferometer uses two antennas separated by a fixed distance horizontally in a plane orthogonal to the platform velocity vector. This separation is called the *interferometric baseline* or simply the *baseline*. The baseline introduces the small depression angle difference between the two images that SAR interferometry requires. Ideally, the remaining data collection geometry parameters and the radar system parameters remain the same for both the SAR images.

Considering Figure 4-1, if we utilize only sensor 2, target 1 cannot be distinguished from target 2 because $R_{S2\text{-}T1} = R_{S2\text{-}T2}$. Hence, there is no detectable phase difference between both the echo signals. Applying a second sensor solves this ambiguity because in that case, $R_{S1\text{-}T2} \neq R_{S2\text{-}T2}$ [2].

The phase of the echo signal that is reflected back from target 2 at the sensor 1 is:

$$\phi_1 = \frac{2\pi * 2R_{S1-T2}}{\lambda} \tag{4.1}$$

The phase measured at sensor 2 is given by:

$$\phi_2 = \frac{2\pi * 2R_{S2-T2}}{\lambda} \tag{4.2}$$

Now, forming the phase difference of both signals results in the interferometric phase:

$$\phi_a = \phi_1 - \phi_2 = \frac{4\pi}{\lambda} * (R_{S1-T2} - R_{S2-T2}) \tag{4.3}$$

which is then used to numerically compute the height [2].

In general, the estimation of the Digital Elevation Model from interferometric SAR raw data involves the following steps [2,15]:

Processing

We start with two corresponding, interferometrically recorded raw-data scenes. Processing the SAR data leads to the formation of two complex SAR images. These two images are formed from the data collected from two different recording positions.

The first image is formed from the values given by:

$$\boldsymbol{\gamma}_1 = |\boldsymbol{\gamma}_1| * e^{j\varphi_1} \tag{4.4}$$

where $\boldsymbol{\gamma}_1$ represents the vector which contains the scattering coefficients of all target pixels required to form Image-1 i.e. $\boldsymbol{\gamma}_1 = \begin{bmatrix} \gamma_{11} & \gamma_{12} & \gamma_{13} & .... & \gamma_{1Nt} \end{bmatrix}$ (4.5)

On the other hand, the second image is formed using the complex values given by

$$\boldsymbol{\gamma}_2 = |\boldsymbol{\gamma}_2| * e^{j\varphi_2} \tag{4.6}$$

where $\boldsymbol{\gamma}_2$ is the vector that contains all the scattering coefficient values needed to form Image-2 i.e. $\boldsymbol{\gamma}_2 = \begin{bmatrix} \gamma_{21} & \gamma_{22} & \gamma_{23} & .... & \gamma_{2Nt} \end{bmatrix}$. (4.7)

Coregistration

This procedure corrects any geometric recording distortions due to the different recording positions of both the receiving antennas.

Formation of the Interferogram

The interferogram is formed by calculating the conjugated complex pixel-wise multiplication of the two complex SAR images. This complex interferogram contains the current height information.

$$\boldsymbol{\gamma} = \boldsymbol{\gamma}_1 * \boldsymbol{\gamma}_2{}^{T} = \mathbf{a}.e^{j\boldsymbol{\varphi}_a} \tag{4.8}$$

where $\boldsymbol{\varphi}_a = \boldsymbol{\varphi}_1 - \boldsymbol{\varphi}_2$ and $\mathbf{a} = |\boldsymbol{\gamma}_1| * |\boldsymbol{\gamma}_2|$. ^{T} indicates a conjugate transpose.

However, at this stage we do come across the problem of phase ambiguity since the phase measurements wrap around the interval [-π,π].

Calculation of interferometric phase

To utilize the height information out of the complex interferogram with the help of the arc tangent function, the phase value is calculated.

$$\boldsymbol{\varphi}_a = \arctan\left(\frac{\mathrm{Im}\{\boldsymbol{\gamma}\}}{\mathrm{Re}\{\boldsymbol{\gamma}\}}\right) + 2\pi N, N = 0, \pm 1, \pm 2, ... \tag{4.9}$$

Phase Unwrapping

The problem of phase ambiguity is resolved with the helped of the phase-unwrapping algorithm [17]. Hence, the unambiguous phase is obtained.

$$\boldsymbol{\varphi}_a \Rightarrow \boldsymbol{\varphi}_h \tag{4.10}$$

[Ambiguous phase $\Rightarrow$ Unambiguous phase]

Reconstruction of Imaging geometry

This step involves geometric calculation of the slant height out of the unambiguous phase. One desirable method used for improving the utility of the

interferogram data is orthorectification [2], which corrects the interferogram for the range layover effect and produces a smooth map.

Creation of the Digital Elevation Model

The final stage of processing involves calculation of the ground height from the slant height values, leading to the creation of a Digital Elevation Model (DEM). The entire process is also described in the flowchart shown in Figure 4-2.

The generation of the DEM and its accuracy is dependent on the phase unwrapping methods, which in turn are linked to orbital parameters and particularly to the interferometric baseline. For a single-pass system, we have accurate information about the baseline formed with the two physical antennas, and thus topography can be calculated using an exact inverse algorithm [2,5]. However, for repeat-pass systems, the exact knowledge of orbital parameters and the precise estimation of the baseline length and orientation pose big problems.

The existing models and TopSAR processing algorithms to obtain high-precision DEM were developed keeping in view

1) a well-defined circular or elliptical geometry limited by vertical and horizontal baseline requirements
2) the assumption that every spatial element provides a quality SAR image

However, as it has been already pointed out, the array formed by a spaceborne constellation of multi-satellites will be sparsely populated and randomly spaced. Moreover, individual elements that make up the constellation are constrained with respect to aperture size and design and therefore a single element (receive antenna) is

not capable of forming accurate SAR images on its own. Hence, the conventional TopSAR algorithms need to be modified accordingly in order to be applicable to this new distributed case. In Chapter 2, we have discussed the procedure of simulating the response from a sparse, randomly distributed array and in Chapter 3, we looked at the idea of forming SAR images by utilizing such a radar response. We will now proceed by looking at how to use those SAR images to obtain accurate topography estimates.

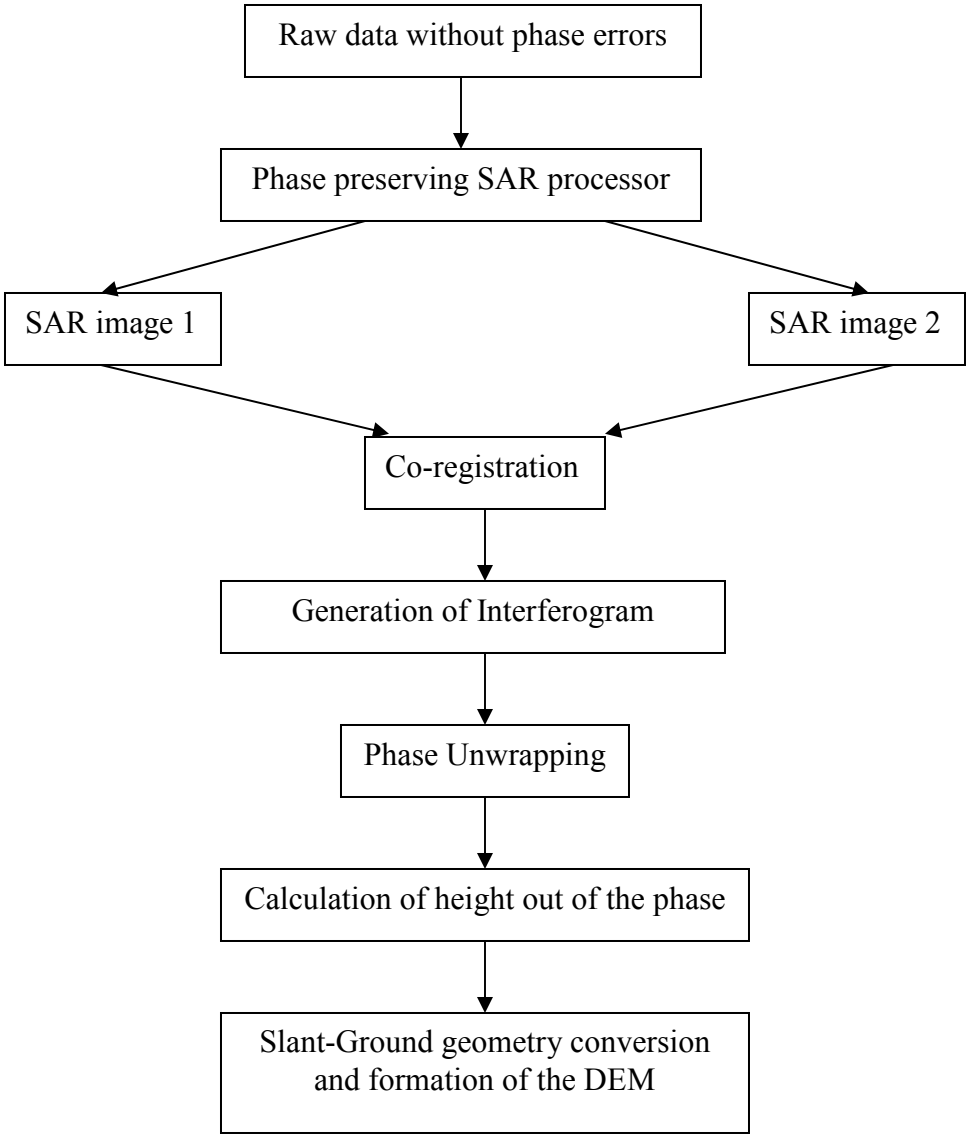

Figure 4-2 Flowchart depicting height estimation using standard interferometric techniques

4.2 Distributed Topographic SAR

The eigensensor analysis technique described in the previous chapter provides the solution to the problems we face when it comes to developing processing and estimation algorithms relevant to the sparse, randomly distributed SAR. Using this technique, we can organize the measurement data that has been obtained and slice that data vector into two parts, so that the measurement samples from each part can be used to form two independent SAR images. Thereafter, the procedure of finding the height estimates is very similar to the standard interferometric SAR.

One very important characteristic of spaceborne radar sensors is the *clutter rank*. A radar collects a limited amount of information since the measurement vector is finite in dimension. For a radar to be effective, this measurement dimension must exceed the amount of information required to completely describe all the illuminated targets. Thus, we could define information as the minimum number of "significant" eigen values of a measurement covariance matrix [11]. For spaceborne radar, the dominant scatterer is the earth's surface and therefore the minimum number of independent measurement samples required to describe the scattering from an illuminated target is known as the clutter rank. As mentioned in the section, this number is effectively equal to the number of resolution cells (pixels) in a SAR image. When it comes to micro-satellite arrays consisting of several elements, we have to collect the data samples from all elements of the array to create a measurement vector whose dimension exceeds the clutter rank. Thus, the strength of a space-time radar sensor is that a fine-resolution SAR image can be formed over an arbitrarily large

area. By adding additional antennas to the radar array, the dimension of sensor measurement can be increased without altering the clutter rank. In this manner, the measurement dimension of the distributed radar can always be made to exceed the clutter rank, no matter how large the image area which is to be mapped. Moreover, the ratio of the measurement dimension to the clutter rank can be made large by adding a sufficient number of elements to the distributed array. This is in contrast with traditional single-aperture SAR, wherein increasing the measurement dimensions (which effectively means increasing the bandwidth or timewidth) leads to a proportionate increase increase in clutter rank.

If we extend the same idea to the distributed topographic SAR, we find that a necessary condition is that the measurement dimension should be at least twice the clutter rank. This is because we need enough measurement samples so that even after partitioning the measurement set into two parts, we have a number of measurement samples that exceeds the number of pixels in the SAR image. Thus, the overall distributed radar can be viewed as a composite of two (or even more) sensors. The next section will deal with the actual methodology used for partitioning.

4.3 Partitioning the radar measurement space

For the standard interferometer, the time frequency (t, ω) data of each SAR element (receive antenna) forms a plane in the three-dimensional measurement space. These planes are parallel to each other, and perpendicular to the measurement dimension associated with the interferometric baseline. Partitioning this data is

therefore straightforward because each time-frequency data plane can now be used to form a SAR image. The main technical challenge that we come across is that of developing a methodology for segmenting the distributed radar measurement vector in an optimal manner, where the optimization criterion is minimized estimation error while forming the SAR images. In other words, how can measurement data from the distributed radar be decomposed into two (or more) unambiguous SAR sensors such that a topographic map can be generated with the smallest error? To accomplish this, we must return to the concept of the eigensensor. For SAR interferometry, the illuminated surface target is expressed as a function of three spatial dimensions which are x, y and z where z indicates surface height. From (2.19), we know that the resulting sensor transformation matrix is a 3x5 matrix and has three non-singular values. To recap the results of the eigensensor analysis, it has already been shown in section 2.3 about how the radar measurements that span five dimensions can be projected onto the eigen vectors $\bar{v}_1, \bar{v}_2$ and $\bar{v}_3$, resulting in a three-dimensional synthetic array where each measurement dimension provides information about one specific target frequency only. This three-dimensional eigensensor provides a tool for optimally partitioning the distributed radar data such that a set of independent SAR images can be formed.

As it will be seen in the results shown later, when it comes to the sparse, distributed radar system, the standard side-looking case is quite simple to analyze. This is because when it comes to the side-looking scenario, the *eigensensor* space contains time-frequency planes corresponding to each receive antenna lying parallel

to each other. On analyzing the three-dimensional eigensensor space, it is found that the γ dimension contains information pertaining to the along-track and vertical positions of the radar receive antennas. Hence, if the time-frequency planes corresponding to each receiver antenna were spatially apart along this γ *eigensensor* dimension, it would effectively mean that the receiver antennas are spatially separated along a rough interferometric baseline in *physical space* as well. Therefore we could simply pick the planes corresponding to one-half the receive elements (which are spatially separated from the other half in *physical* space as well as in *eigen* space) to form one SAR image and utilize the remaining half of the measurement samples to form the second SAR image. This process is depicted in Figure 4-3.

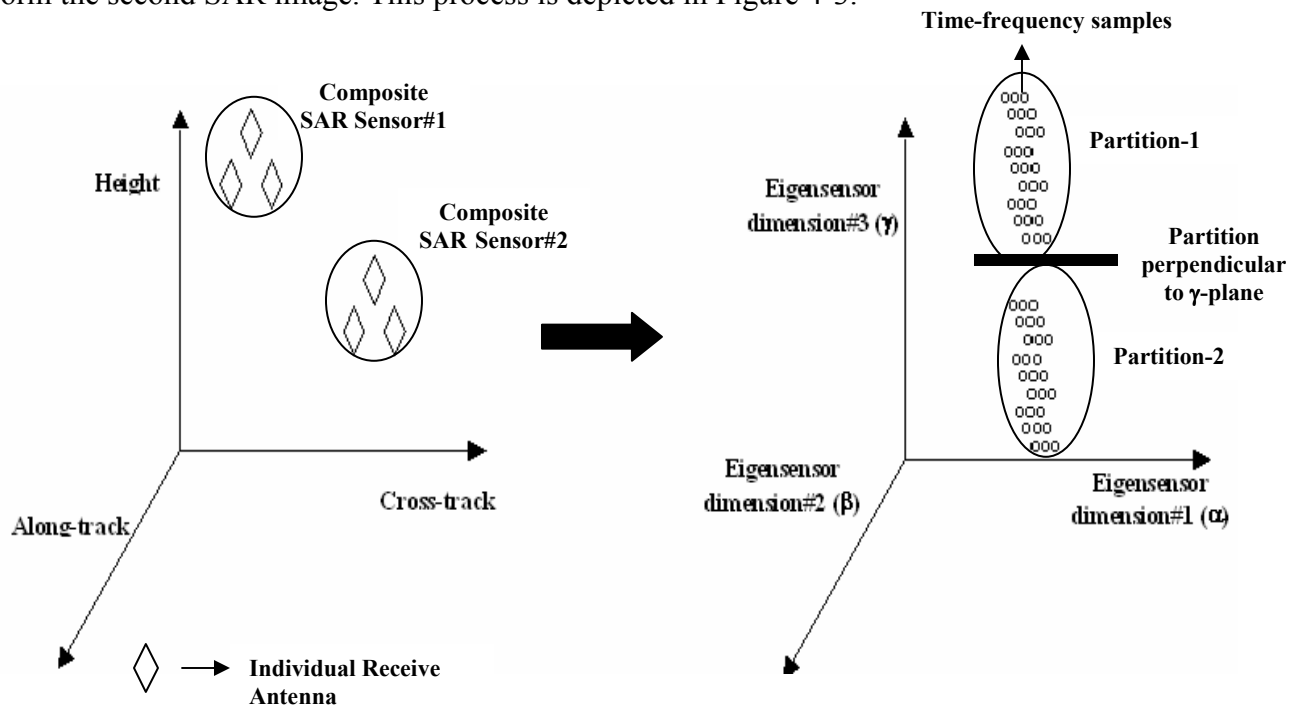

(a) Actual arrangement of receive antennas in space **(b) Equivalent Eigensensor**

Figure 4-3 Depiction of eigensensor and methodology of partitioning (Side-look)

The figure 4-3(a) looks at an arrangement of six receive antennas in space. The spatial location of the antennas is such that two spatially separate *composite* SAR sensors (consisting of two groups of three receive antennas each) can be formed. As seen in Figure 4-3 (b) the process of eigensensor analysis organizes the data in such a way that the time-frequency planes corresponding to the antennas contained in SAR sensor 1 constitute partition 1 while those corresponding to the antennas contained in SAR sensor 2 constitute partition 2. These two data sets obtained after partition are used to form the required complex SAR images.

Now, if we consider a forward (or backward) looking case, the problem becomes more complex because the planes which contain measurement data does not lie along parallel planes but will be distributed throughout the three-dimensional measurement space defined by the *eigen* coordinates α, β and γ. However, the measurement data can still be partitioned in a manner analogous to the standard SAR interferometer. The data can be partitioned into parallel layers, where the data in each layer can be used to form a SAR image. In this way, the distributed radar sensor can be decomposed into one or more independent SAR sensors. An important point to be noted here is that it is quite possible that two measurement samples taken at different times and at different receive antennas can occupy the same location on the eigensensor array. And this makes the partitioning problem more critical. Firstly, the thickness of each layer depends again on the clutter rank – the number of measurement samples included in each layer must exceed this clutter rank which, as mentioned earlier, equals the number of pixels in the SAR image. Secondly, the

partitioning process should also take into account the orientation of the layers within the eigensensor space. The challenge is to determine which would be the right way to slice the measurement space. The answer lies in the fact that there is one measurement direction in the eigen sensor array, γ, which is associated with a change in the surface height. The extent of the eigen array in this direction is analogous to the length of the interferometric baseline of the standard SAR interferometer. In other words, the length of the array in this direction is very important with respect to estimation accuracy. Thus, the larger this baseline, more accurate will be the topographic estimate. We could therefore conclude that the measurement samples in the eigensensor should be partitioned into layers perpendicular to the direction of the coordinate γ. The resulting SAR images correspond to independent samples along the equivalent interferometric baseline of the eigensensor and thus provide a set of complex scattering estimates for each resolution cell that would potentially lead to accurate topographic estimates.

We have now established a mechanism to organize the response of a distributed, sparse SAR (eigensensor analysis) and also discussed the methodology that could be used to partition the measurement space, form two complex images and use interferometric techniques to estimate the height of the topography. The next chapter deals with describing the *topography estimation algorithm* and analyzing the various tests and simulations that were carried out to apply the above techniques and discuss the results obtained.

5. TOPOGRAPHY ESTIMATION ALGORITHM

5.1 Description of the algorithm

This section contains the core of the thesis and will describe, in detail, the topography-estimation algorithm that was developed for generating a three-dimensional elevation model corresponding to the height of a given landscape. In the previous chapter, we looked at a technique to organize and partition the measurement space so that suitable processing algorithms could be applied to the sparse, distributed case as well. The following steps summarize the *topography estimation algorithm*, and the various results obtained will be shown in the following sections:

Step 1: Simulating the distributed SAR response

The space-time radar simulator is used to obtain a set of measurement samples that constitute the response vector. Once the response and the normalized response vectors $\boldsymbol{\rho}$ are obtained, we could use these vectors along with other information to estimate the value of scattering coefficients that constitute a SAR image by using the Kalman filter algorithm, which was developed and described in Chapter 3. The *base case* that is considered is one in which all the targets are at zero height (no elevation). The *base* $\mathbf{P}$ matrices (and thus the component normalized response vector-$\boldsymbol{\rho}$ *matrices*) were evaluated for this case and stored as data files. As mentioned earlier, the normalized measurement vector $\boldsymbol{\rho}$ is very important because it basically consists of the full set of measurement vectors obtained by the radar at a discrete set of space and time locations due to a particular target. Hence, by storing the $\boldsymbol{\rho}$ vectors

corresponding to the case when all the targets are at zero height, what we mean is that the SAR processor has information only about the targets when they are all located over a flat surface with no elevation at all. However, in reality, the topography varies with respect to altitude. It could contain grasslands with gradually varying slopes or mountainous regions with steep slopes. Hence, the *actual case* would be one wherein we supply the SAR simulator with the real values of height and evaluate the *actual* response vector $\mathbf{r}$.

Step 2: Partitioning the measurement data

What we actually need is a set of two complex SAR images. Hence, the measurement vector $\mathbf{r}$ is partitioned using the technique explained in section 4.3 in order to form two complex SAR images using measurements from the two partitions.

Step 3: Processing

The two primary inputs to the Kalman processor are again the vectors $\mathbf{r}$ and $\boldsymbol{\rho}$. Now, while the Kalman processor has the $\boldsymbol{\rho}$ vectors corresponding to zero target height (base case), the response vector that we are providing it with contains the measurements corresponding to the *actual* varying topography. Hence, when we form the two SAR images using the partitioned sets of data, there will be an "error" in estimation using the KF.

Step 4: Calculation of interferometric phase

We are particularly interested in the *phase errors,* which refer to the errors in estimation of the phase of the scattering coefficient values. This phase error value is found to be proportional to the target height. The difference in the phase values

corresponding to a particular target, detected at both the SAR sensors, is what we define as *interferometric phase* and a plot of this parameter enables us to obtain a clear indication of how it varies with target height.

To start with, let us define the estimated scattering coefficient of a particular target, say '*t*', at sensor 1 as γ_{1t} where,

$$\gamma_{1t} = |\gamma_{1t}| * e^{j\varphi_1} \tag{5.1}$$

It is evident that γ_{1t} is one of the elements of the vector $\boldsymbol{\gamma}_1$ defined in (4.5)

Similarly, we define the estimated scattering coefficient of *the same* target at sensor 2 as γ_{2t} where,

$$\gamma_{2t} = |\gamma_{2t}| * e^{j\varphi_2} \tag{5.2}$$

Then we have,

$$\gamma_{diff} = \gamma_{1t} * \gamma_{2t}^{T} = |\gamma_{1t}| * |\gamma_{2t}| e^{j(\varphi_1 - \varphi_2)} \tag{5.3}$$

Again, from (4.7) γ_{2t} would be one of the elements of the vector $\boldsymbol{\gamma}_2$ which contains all the scattering coefficients required to form the second SAR image.

The value of difference in phase $\boldsymbol{\varphi}_1 - \boldsymbol{\varphi}_2$ is the interferometric phase and is a very critical parameter when it comes to estimating height. ^{T} indicates conjugate transpose.

Step 5: Surface height estimation

To finally estimate the height, we need to have some idea about how the interferometric phase varies with different target heights. In order to get this information, simulations were carried out wherein a chosen target was moved to different heights and the corresponding interferometric phase was recorded at each

step. A plot of the obtained values enables us to calculate the critical "slope" value (rate of change of interferometric phase with respect to height) necessary for height estimation.

With this information, we could now obtain the interferogram corresponding to the *actual* surface topography in which each target pixel is elevated to a certain height, calculate the interferometric phase and with the obtained "slope" information, the height of each target pixel could be estimated to form a complete digital elevation model (DEM). The flowchart shown in figure 5-1 describes the complete surface estimation algorithm. It is quite clear that this algorithm is fundamentally quite similar to the standard interferometric techniques and very useful because with it, we have a very useful tool to carry out topographic estimation even with the sparse and distributed spaceborne radar arrays

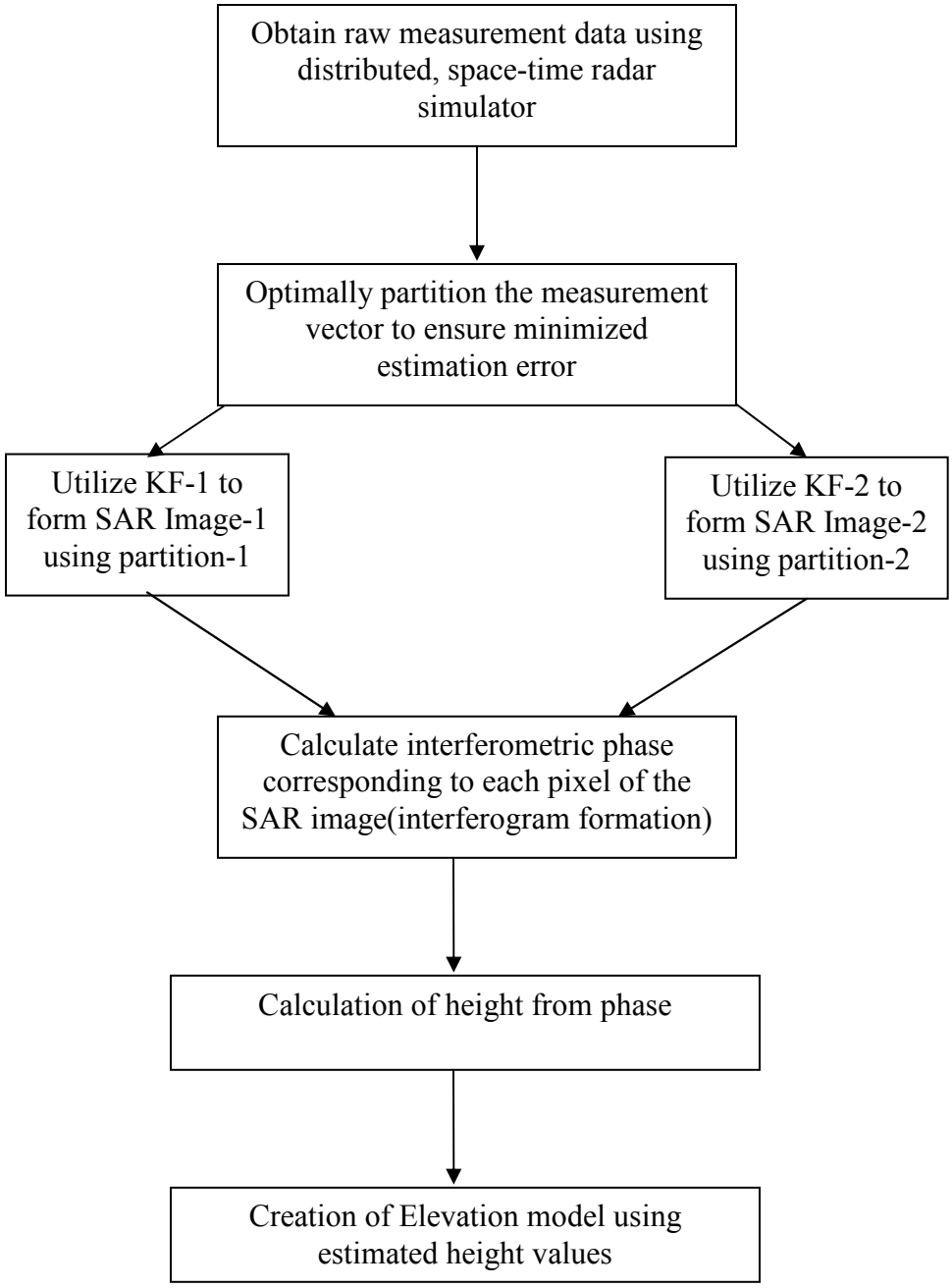

Figure 5-1 Depiction of the topography-estimation algorithm

5.2 Test 1 – Targets along the cross-track axis

Before testing the algorithm with a more realistic scenario, a simple scenario was considered. This section deals with a test carried out in which a 15x15 square target grid was considered but then all targets, expect those that are spread out along a line over the cross-track reference axis, were removed. We are therefore concerned only with two dimensions – *y* (cross-track) and *z* (height). Figure 5-2 depicts the layout of the targets.

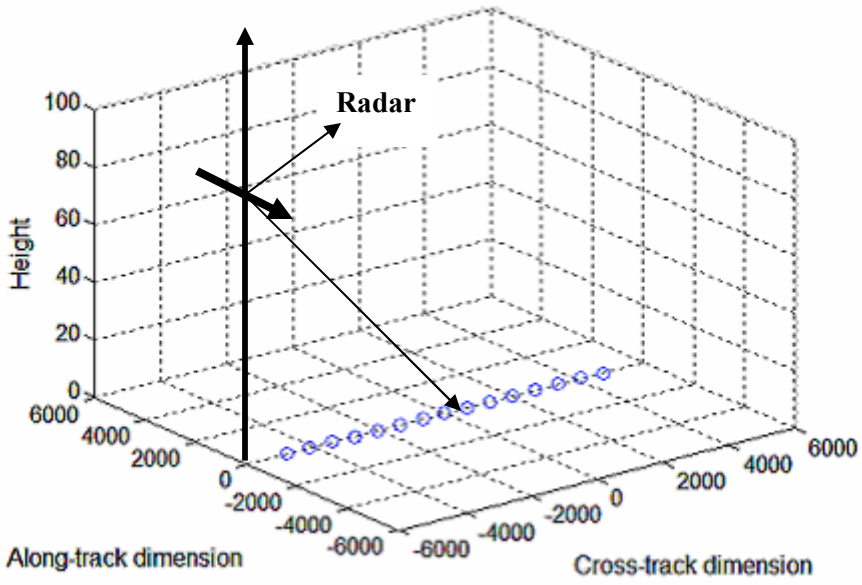

Figure 5-2 Target space – Standard side-looking scenario

All targets are initially assumed to be at zero altitude. We also assume a *standard side-look* SAR scenario. The main objective of this test was to mainly

1) observe and analyze the measurement space as well as the target space in *eigen* dimensions.

2) Determine how to partition the measurement space optimally so that the information gained from this test could be extended to a more realistic three-dimensional scenario.

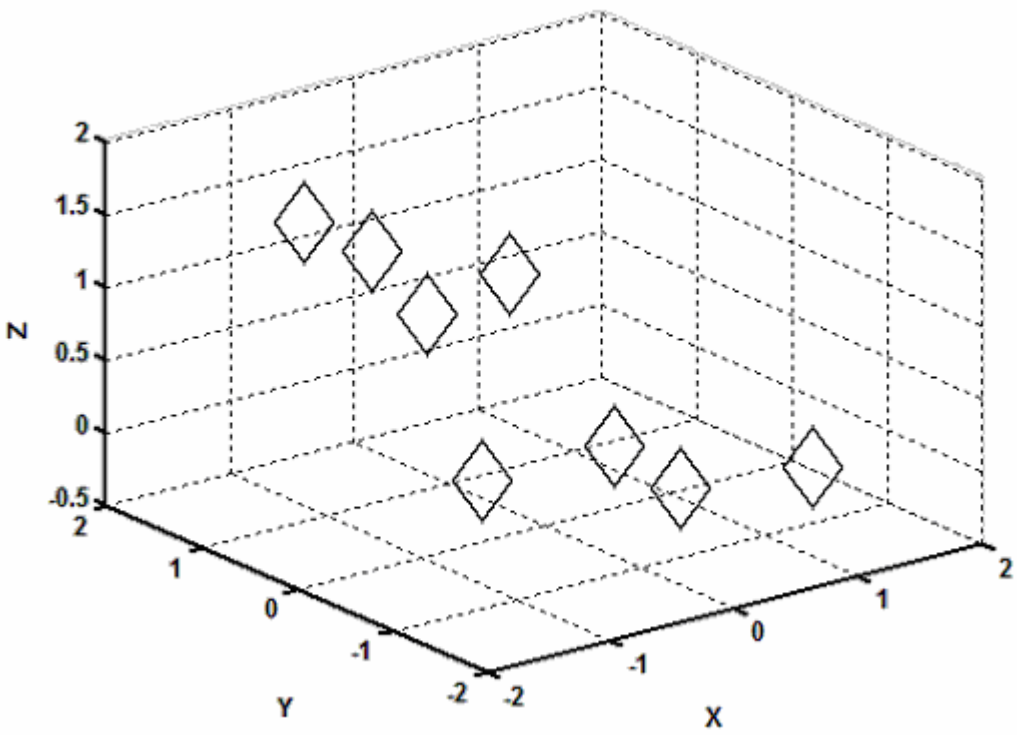

Figure 5-3 Arrangement of receive antenna elements in space

In order to simplify the problem, the number of time samples was fixed at one. Figure 5-3 depicts the spatial receive antenna array arrangement. The coordinates of the antenna location were chosen randomly by taking into consideration the length of the radar array. We need to keep in mind that the along-track position of a target is completely measured by time and the along-track position of the receiver. On the other hand, the cross track location is completely measured by frequency and the cross-track receiver position.

Table 5-1 indicates the parameters were used as input to the SAR simulator in order to carry out this test.

Number of receive elements (antennas)	8
Number of along-track target pixels	1
Number of cross-track target pixels	15
Number of time samples	1
Number of frequency samples	30
Total number of samples/receive antenna	30
Length of aperture	2.267 m
Along-track target resolution	685 m
Cross-track target resolution	685 m

Table 5-1 Input values for the radar simulator during Test-1

The target pixels were assigned scattering coefficient values whose magnitude and phase were picked randomly. The radar simulator provided a response vector which consisted of 240 samples. Figure 5-3(a) depicts the measurement (sensor) space in eigen dimensions while Figure 5-3(b) depicts the target space in eigen dimensions.

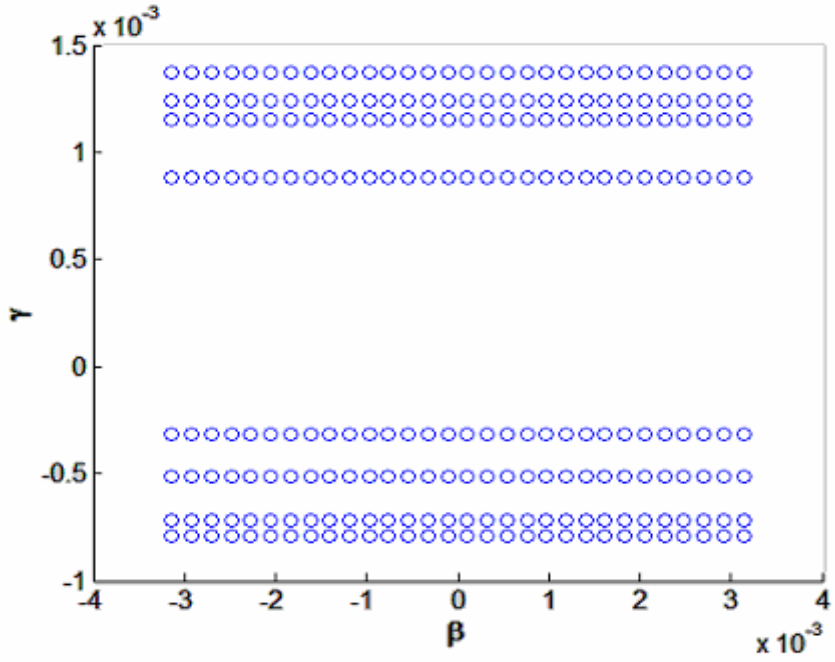

Figure 5-4(a) 2D Eigensensor array (1-time sample and 30-frequency samples/antenna)

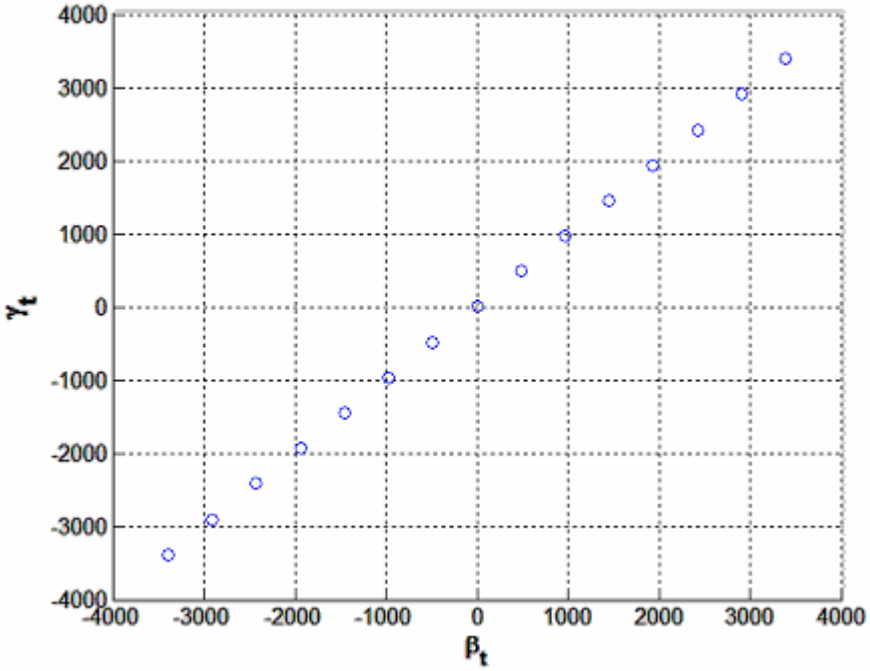

Figure 5-4(b) Target space in Eigen dimensions

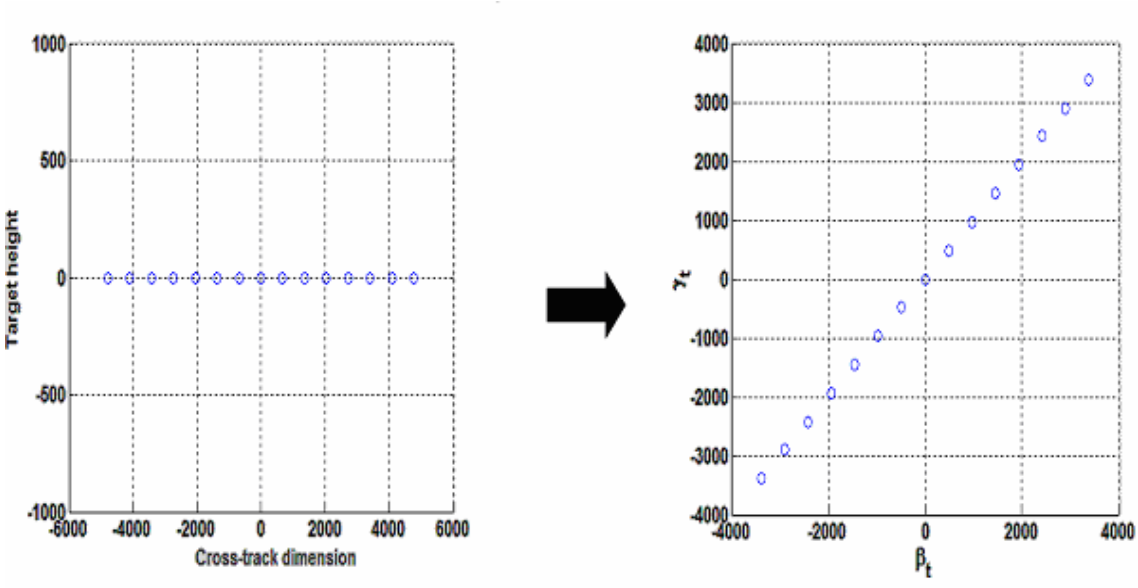

Figure 5-5(a) Target space projected on to eigen coordinates – all targets are at zero altitude

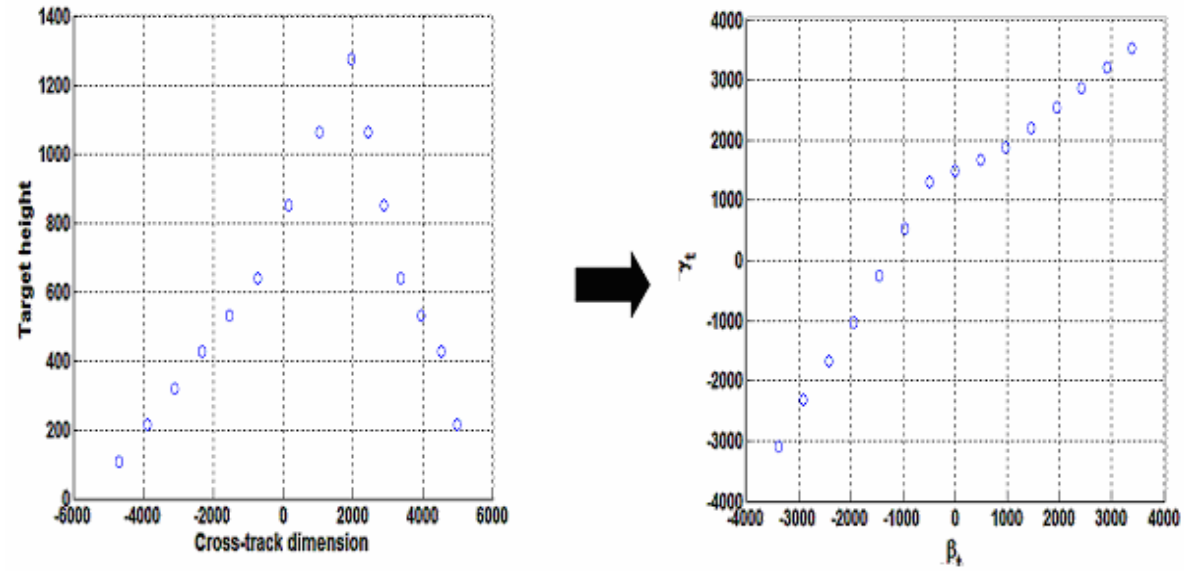

Figure 5-5(b) Target space projected on to eigen coordinates – targets are at varying altitudes

Since we are looking at a two-dimensional case, the eigen space is also two-dimensional while the transformation matrix $\overline{\overline{K}}_{\varphi}$ is a 2x5 matrix. The target "eigen" coordinates are labeled as β_t and γ_t while the eigensensor coordinates are designated as β and γ. It is clear that when the target position vector $\bar{y}_t$ is projected on to the vector $\bar{u}$ (obtained after SVD on the transformation matrix), it gets rotated as seen in the Figure 5-5(a). The eigensensor is also two-dimensional and consists of the measurement (frequency) samples corresponding to each antenna neatly lined up next to each other. From our discussion about *eigensensor analysis*, we know that the sensor dimension β provides information about the target position along dimension β_t while the sensor dimension γ provides information about the target position along γ_t. Therefore, in order to determine the interferometric phase, we work in the eigen space. Each target pixel is provided a perturbation equal to its height along the γ_t dimension since this will be sensed by the γ dimension of the eigensensor. We already know from Section 4.3, that the optimal partitioning would occur if the eigensensor is portioned into layers perpendicular to the dimension which corresponds to target height. Therefore, since the γ_t dimension corresponds to target height, we would need to partition in a direction which is perpendicular to the γ dimension as shown in Figure 5-5. The partitioning process provides us with two sets of measurement samples which can be used to form the two complex SAR images.

From (5.3), the interferometric phase can be calculated. However what we still need to investigate is how this phase value varies with target height. In order to obtain this information, a test was carried out wherein target 8 was moved to different

heights ranging from a depth of 10,000 meters to a peak of 10,000 meters. The results obtained are depicted in Figure 5-8.

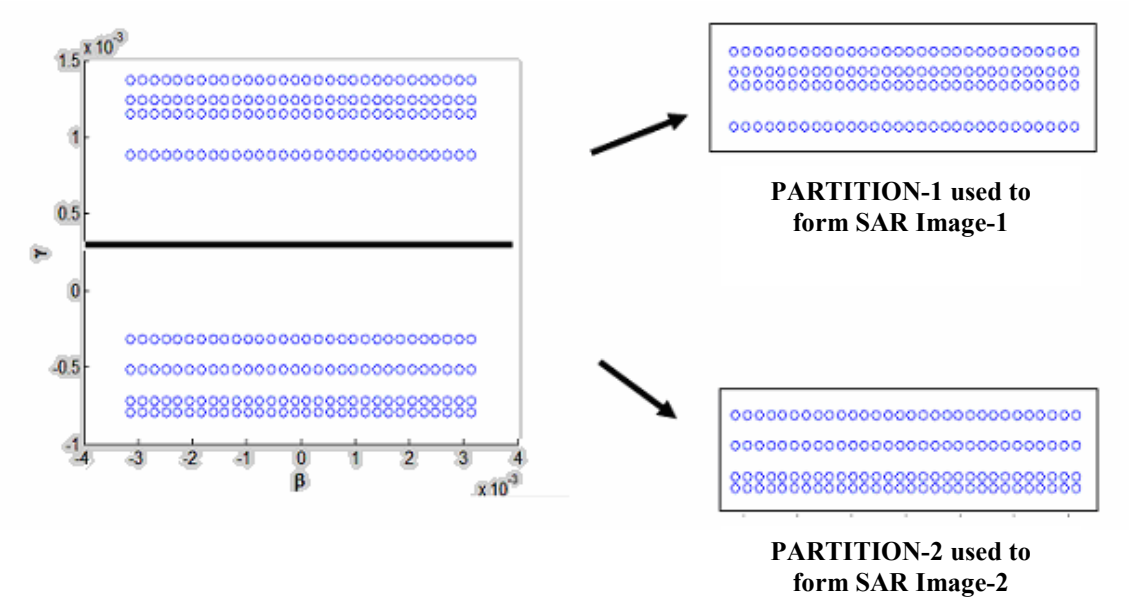

Figure 5-6 Partitioning of measurement space to form two SAR images

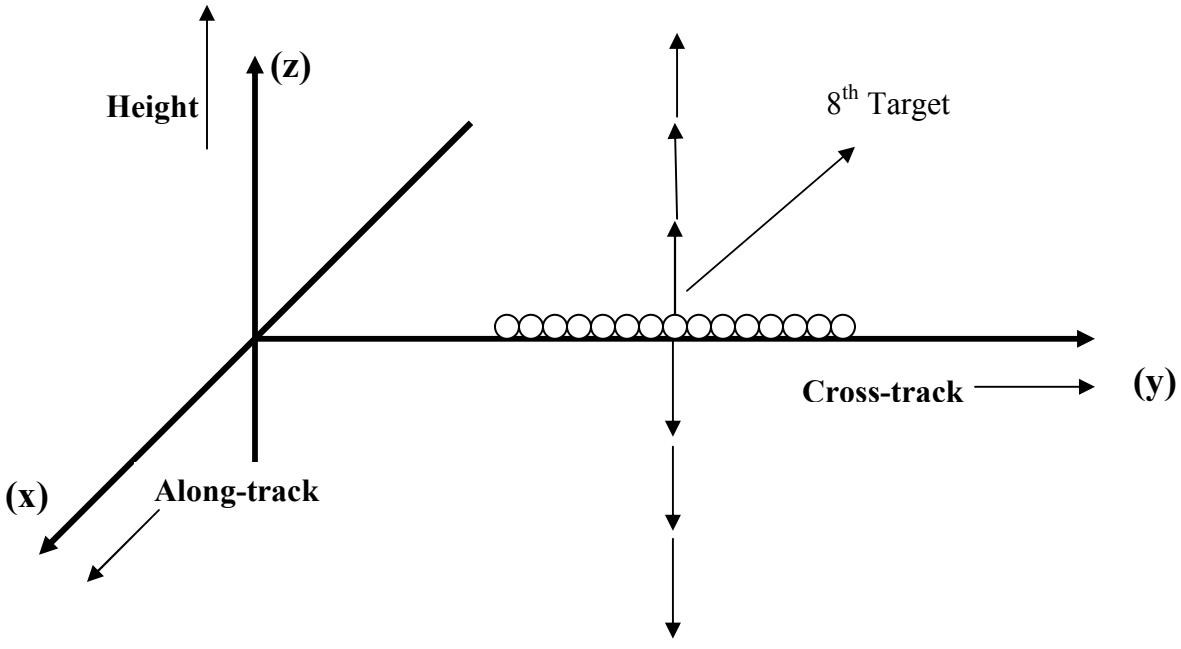

Figure 5-7 Target 8 shifted in order to determine the interferometric phase at different heights

Figure 5-8 clearly depicts the variation of interferometric phase with respect to the target position along the eigen dimension γ_t. As expected, the phase value lies in the interval $[-\pi, +\pi]$ and beyond heights/depths of around 2000 meters, we have to overcome phase ambiguities because of the *wrap-around* effect.

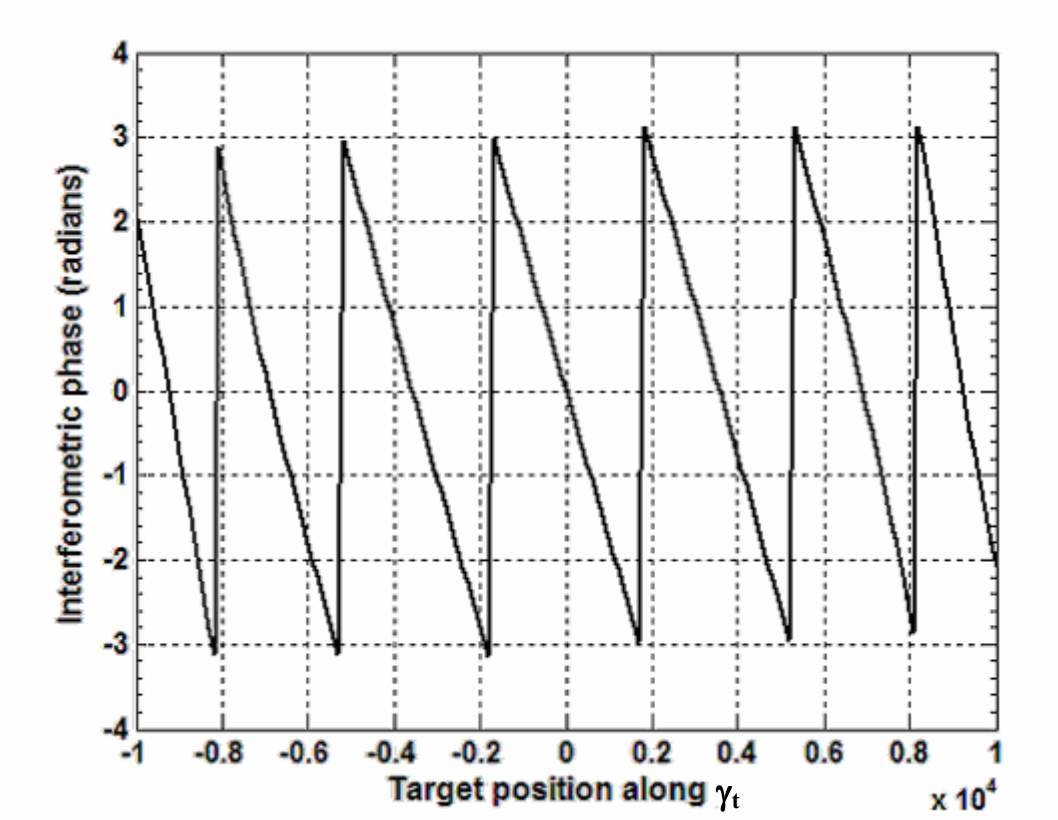

Figure 5-8 Variation of interferometric phase with target height

The reason we need the above plot is that it gives us critical information about the rate of change of the phase. This value is given by the *slope* of the linear portion of the above plot. With this information we can determine the height of any given target pixel if we know the difference between the phase values recorded at the two SAR sensors as seen from (5.3).

We are also interested in examining the change in interferometric phase recorded due to other targets when only target number 8 is shifted to different altitudes. For example, what we expect is that when target pixel number 8 is at a height of approximately 500 m and another target (say target pixel number 11) is at zero altitude, we should ideally detect no difference in the phase values recorded (in the response from target number 11) at the two SAR sensors. Figure 5-9 depicts a plot of the relative change in the interferometric phase due to change in height of target 8 when compared to other targets, which are kept at zero altitude.

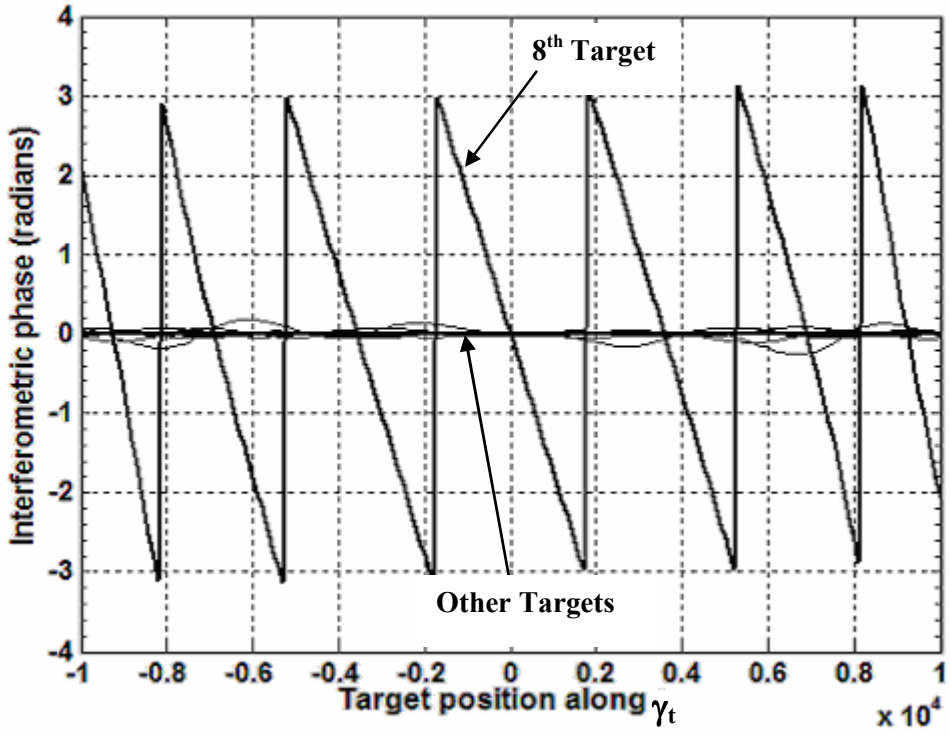

Figure 5-9 Change in the interferometric phase corresponding to target 8 when compared to that of other targets

Another interesting plot obtained during this test is shown in Figure 5-10. This plot gives the variation of the normalized magnitude of the scattering coefficient

corresponding to target 8 as it is moved to different altitudes. Basically, it gives us an idea about what maximum height or depth the target can be at in order to stay within the main beam of the radar antenna. From (3.21), the approximate width of the main beam is given by,

$$\Delta X_s = \frac{cR_0}{f_c L_x} \tag{5.4}$$

where L_x is the spatial extent of the radar array in the along-track direction.

By calculations using the above equation, it is found that the width of the main beam is around 3425m and this is corroborated by Figure 5-10.

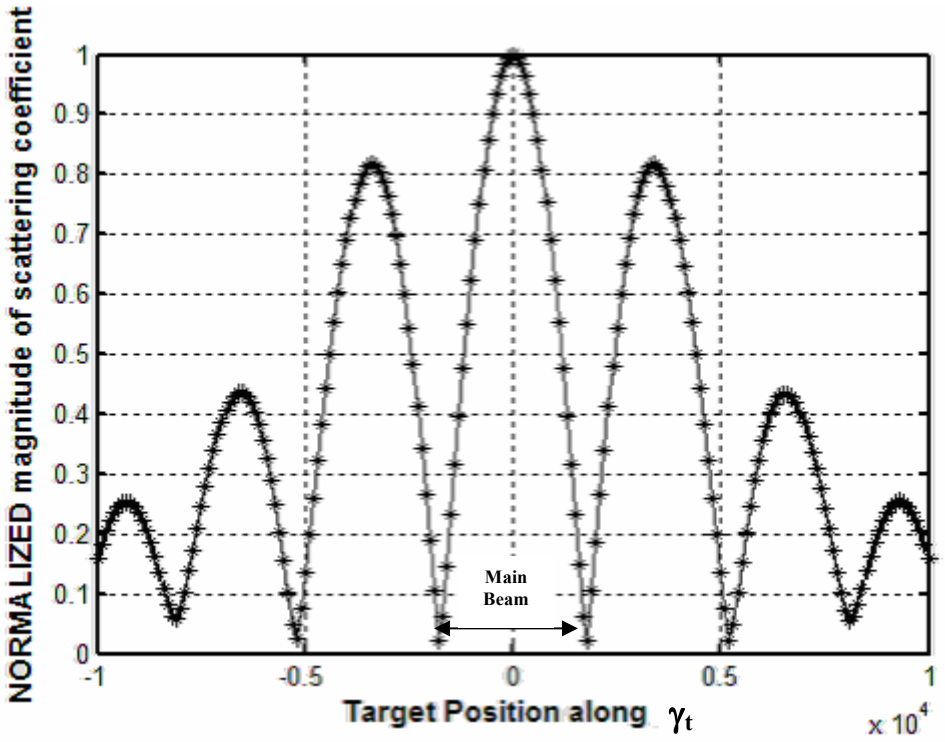

Figure 5-10 Variation of the *normalized* magnitude coefficient of target pixel 8 as it is moved to different altitudes

We then go ahead and compare the width of the beam obtained in the *fully-focused case* (in which the KF utilizes all the measurement samples) to the beam widths obtained with KF-1 and KF-2 individually. The acronym KF used here refers to the Kalman Filter. Since the length of the array reduces effectively by a one-fourth, we see from (5.4) that the beam width increases (approximately four times). Figure 5-11 demonstrates this behavior.

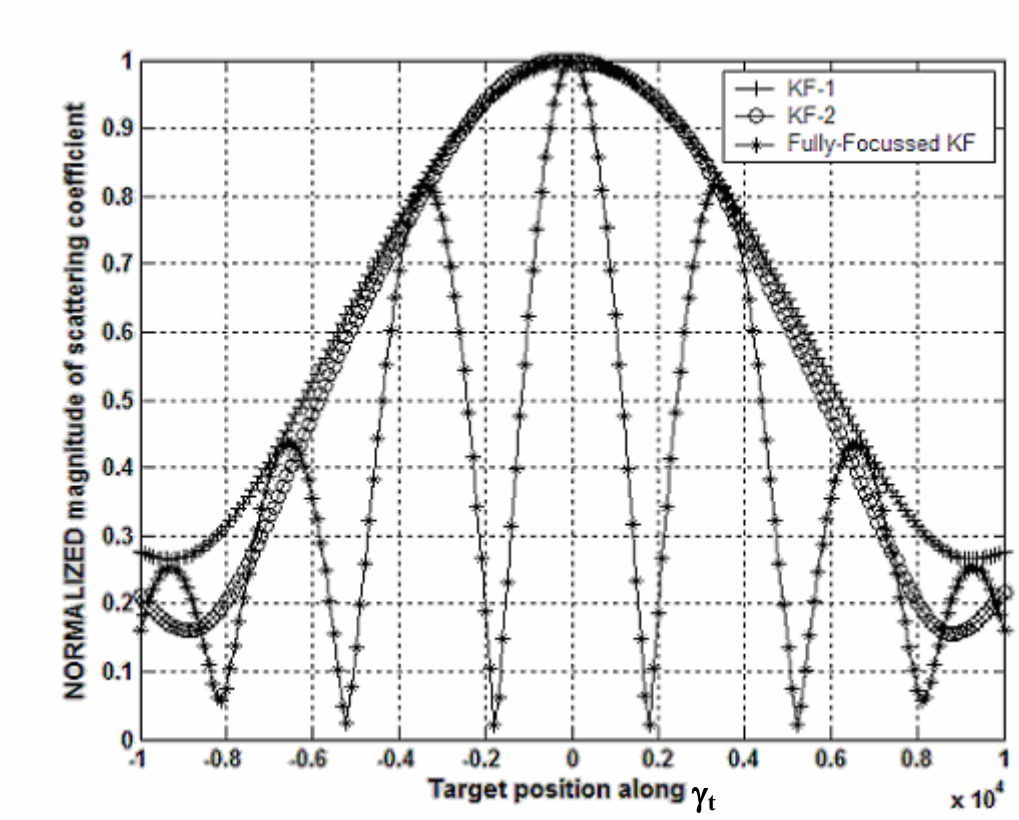

Figure 5-11 Comparison of variation of normalized magnitude of scattering coefficient (i) Fully focused KF (ii) KF-1 (iii) KF-2

With the information obtained using this test, we are ready to apply the topography estimation algorithm to a more realistic three-dimensional scenario, and this will be the focus of the next section.

5.3 Test 2 – Three-dimensional scenario

We are now ready to test the algorithm with a more realistic scenario in which the targets are spread out over a square grid such that the resolution along one dimension is the same as the resolution along the other. Each target pixel was assigned a specific scattering coefficient value whose magnitude and phase was chosen randomly. Figure 5-12 shows the layout of the target pixels over a three-dimensional Cartesian coordinate system while Figure 5-13 shows the optical image that is formed by assigning randomly generated values of scattering coefficients to each target pixel.

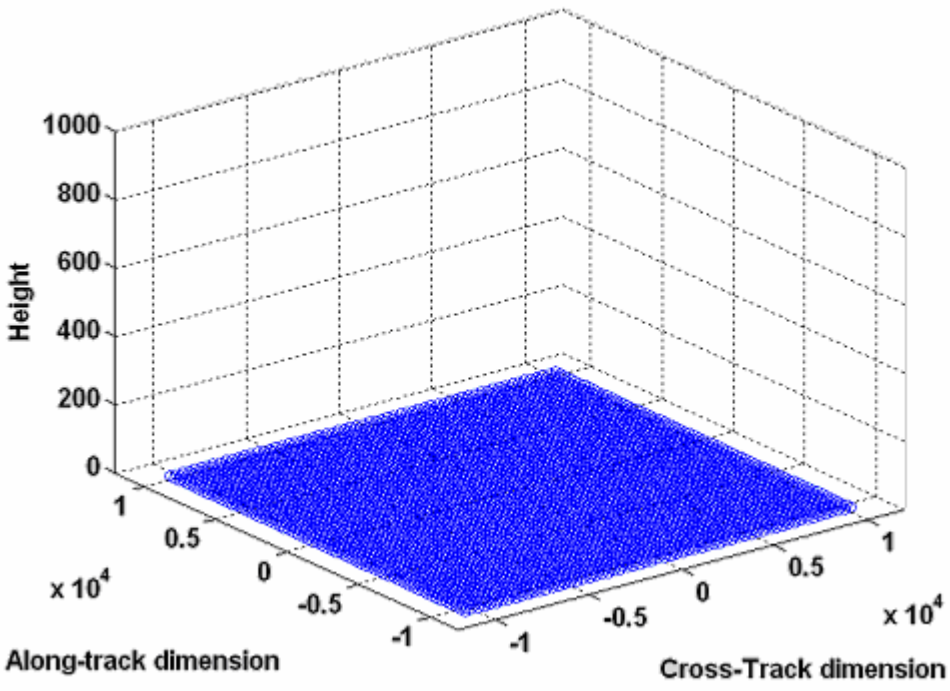

Figure 5-12 Three-dimensional target space (63x63) with targets at zero altitude

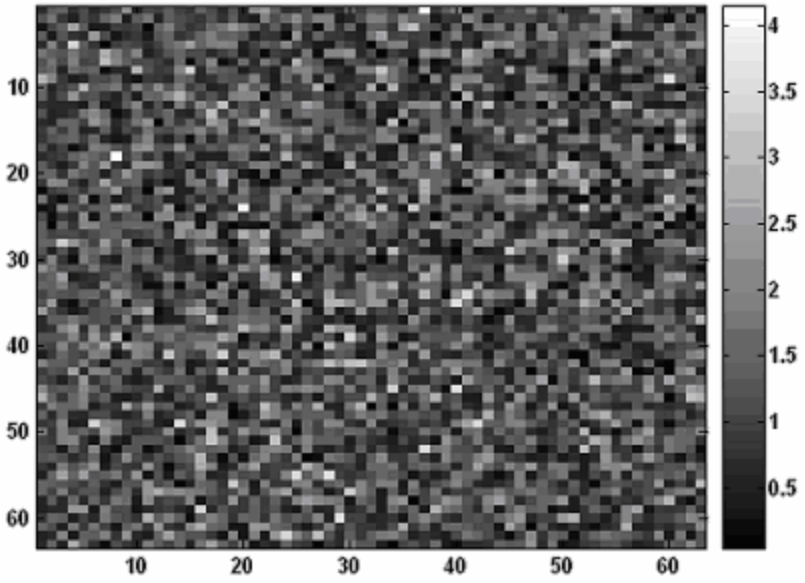

Figure 5-13 Randomly chosen scattering coefficient values for each pixel of the given target grid

The values chosen as input to the radar simulator are shown in Table 5-1

Number of receive elements (antennas)	8
Number of along-track pixels	63
Number of cross-track pixels	63
Number of time samples	31
Number of frequency samples	63
Total number of samples/receive antenna	1953
Length of aperture	1.1143 m
Along-track target resolution	335 m
Cross-track target resolution	335 m

Table 5-2 Input values for the radar simulator during Test-2

Figure 5-14 below shows the scenario where each target pixel is at a different altitude.

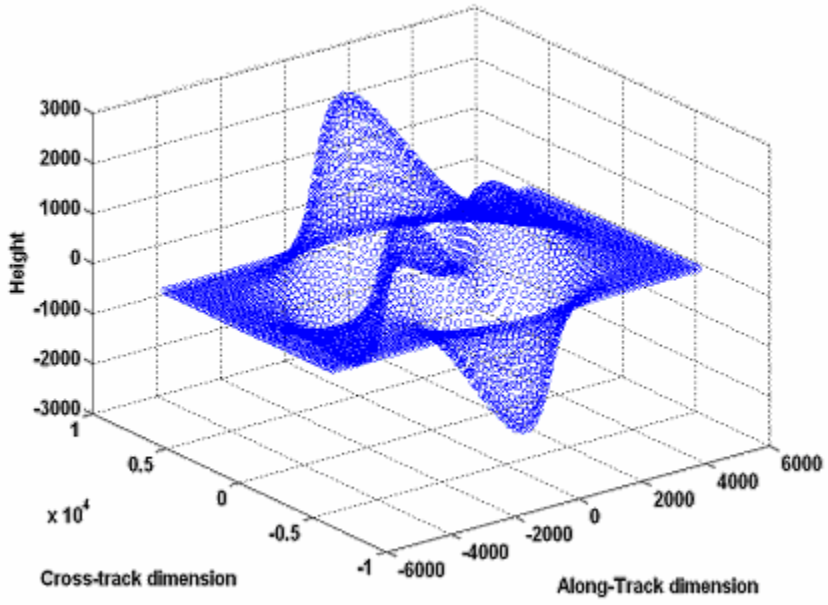

Figure 5-14 Three-dimensional target space with targets at different altitudes

The sensor transformation matrix will be a 3x5 matrix in this case because we have to consider all the three dimensions (along-track, cross-track and height) of the target in our measurements. Using *eigensensor* analysis, we obtain the three-dimensional eigensensor as well as the target layout in *eigen* space. The standard side-look case provides us with a very simple representation of the measurement space in eigen dimensions. As seen from Figure 5.15(a), all the time-frequency samples corresponding to a particular receive element form a two dimensional plane and the time-frequency planes corresponding to all the antennas neatly line themselves parallel to each other which greatly simplifies the problem. However, as it will be seen later, the analysis is a little more complicated when it comes to the forward-look or the backward look case.

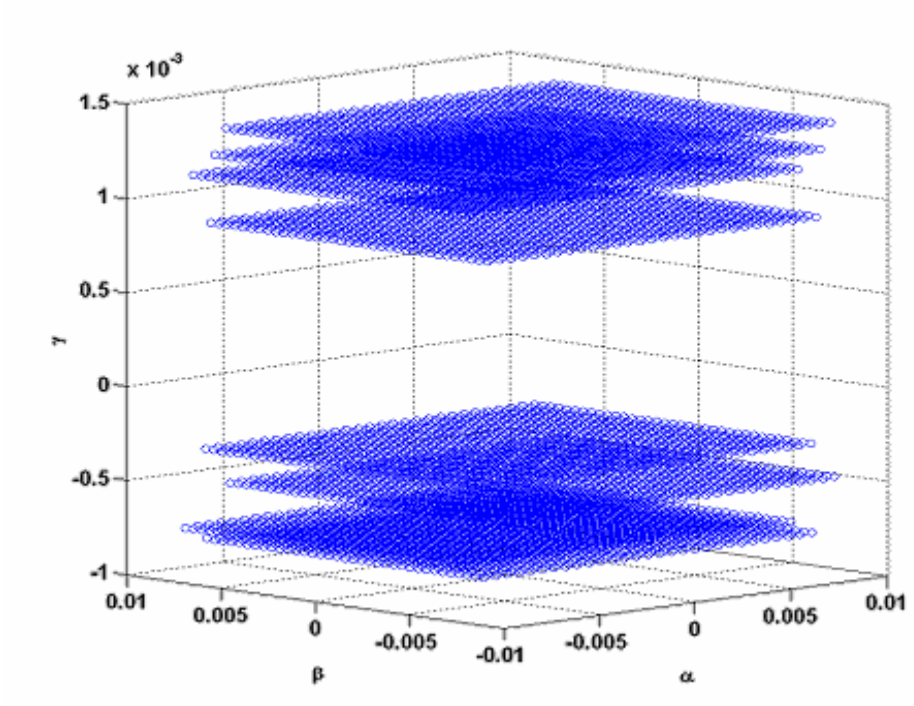

Figure 5-15(a) 3D Eigensensor array (Side-look)

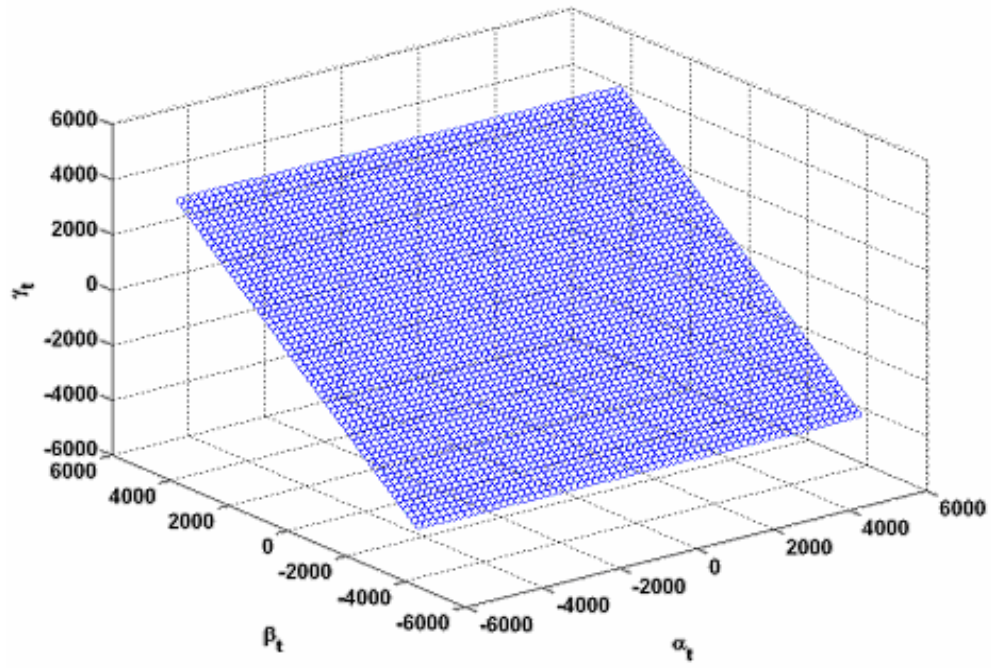

Figure 5-15(b) Target space in Eigen dimensions

Having organized the measurement data obtained at the output of the SAR simulator, we could proceed by partitioning the data in order to form the two complex SAR images. Again, from the concepts discussed in the previous section, we know that the sensor dimension γ can detect any position of the target along the γ_t dimension which basically contains information about any change in the surface height. Thus we partition the data in such a way that the time-frequency samples corresponding to four out the eight receive antennas lie in one partition and the remaining samples constitute the second partition. The two SAR images that are formed using these two partitions are equivalent to images of the same surface formed from two spatially separate locations and in this case, the *interferometric baseline* is provided by the extent of the eigensensor along the γ dimension.

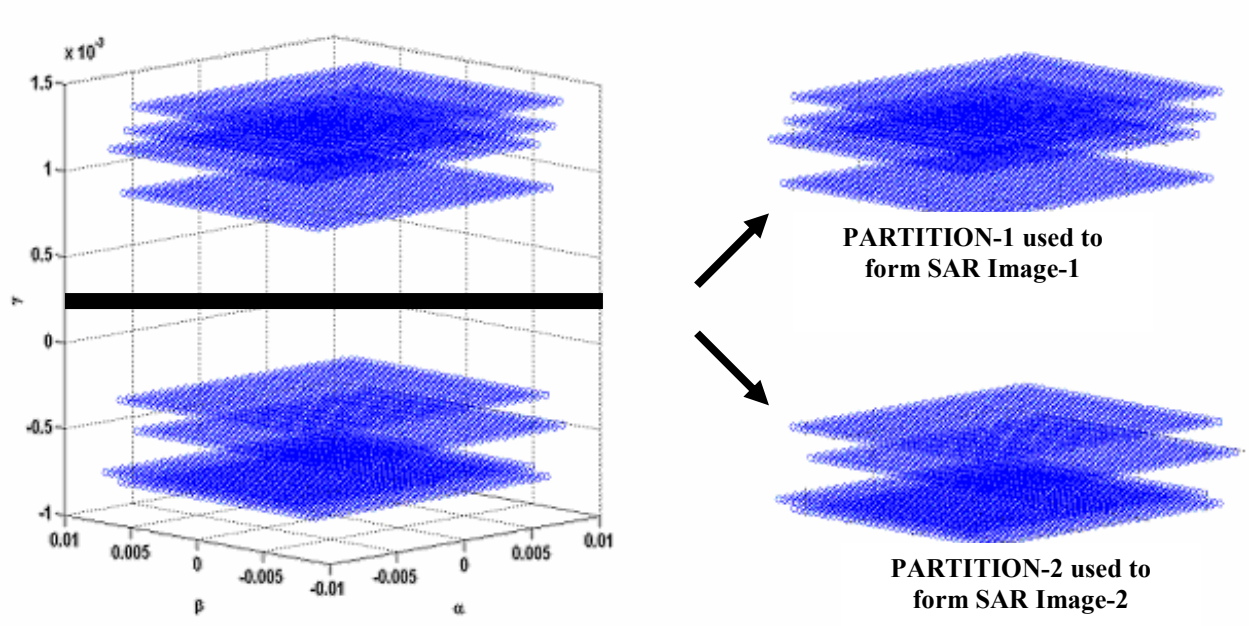

Figure 5-16 Partitioning the three-dimensional Eigensensor

Before proceeding with the process of height-estimation, a quick test was carried out to observe the variation of interferometric phase with target position. Due to computational constraints, a simpler three-dimensional scenario consisting of a 15 by 15 grid was chosen and a test was carried out wherein target 113 was picked and moved to different heights ranging from a depth of 20,000 meters to a peak of 20,000 meters. Figure 5-17(a) depicts the variation of interferometric phase as a function of target height. It is observed that the width of the main beam is wider because of the different spatial arrangement of the receive antennas when compared to the two-dimensional case. Figure 5-17(b) shows a plot of the normalized magnitude of scattering coefficient corresponding to target pixel 113 as it is moved along the β_t eigen dimension.

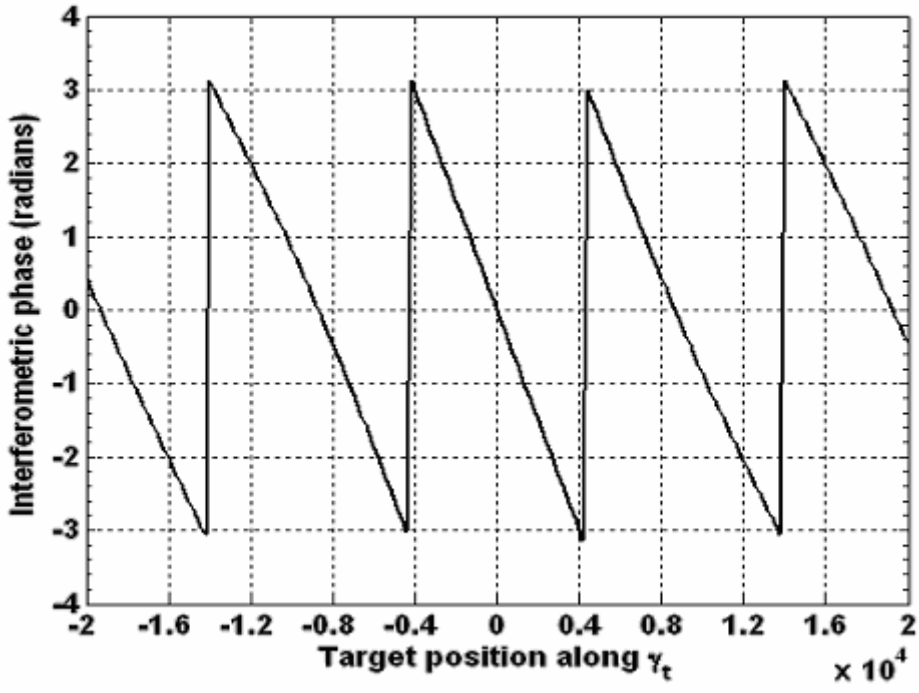

Figure 5-17(a) Variation of interferometric phase with position of 113th target for a 3D scenario

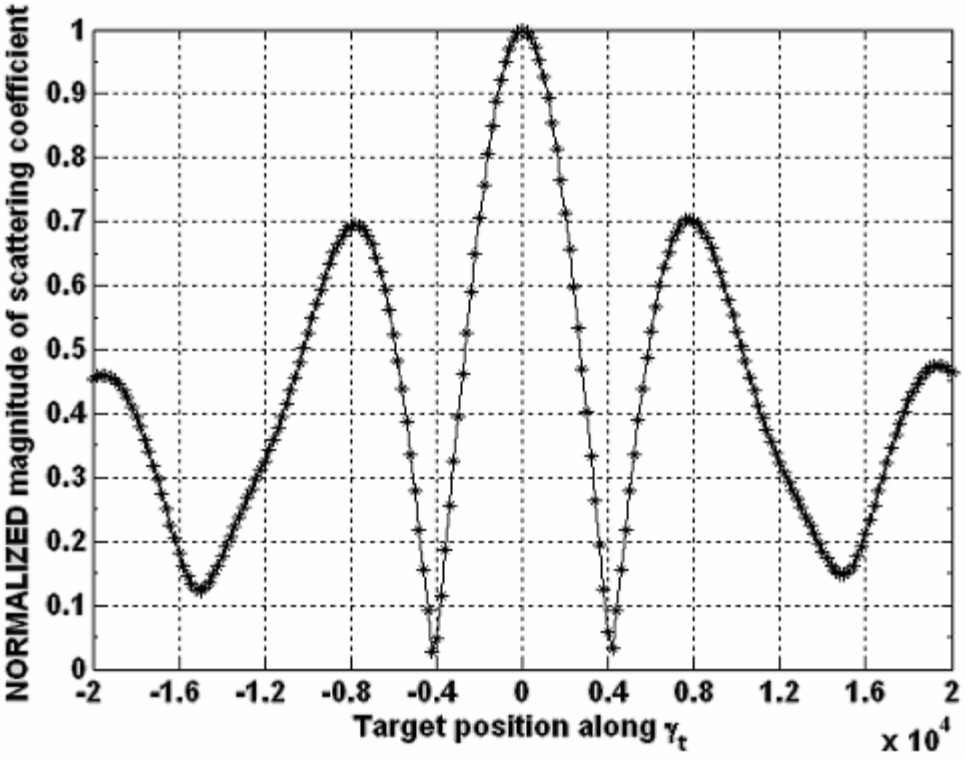

Figure 5-17(b) Normalized magnitude of scattering coefficient as a function of target position

Figure 5-17(a) provides us very critical information regarding the rate of change of the interferometric phase with respect to target position along the β_t dimension which corresponds to target height. We can define some important vectors at this stage.

From (4.5), $\boldsymbol{\gamma}_1 = \left[\gamma_{11} \quad \gamma_{12} \quad \gamma_{13} \quad ..... \quad \gamma_{1N_t}\right]$ represents the complex scattering estimates of a specific resolution cell as determined by KF-1 using the measurement samples contained in one out of the two available partitions.

From (4.7), $\boldsymbol{\gamma}_2 = \left[\gamma_{21} \quad \gamma_{22} \quad \gamma_{23} \quad ..... \quad \gamma_{2Nt}\right]$ represents the complex scattering estimates of a specific resolution cell as determined by KF-2 using the measurement samples contained in the second partition.

$\boldsymbol{\varphi}_{INT} = \left[\phi_{INT-1} \quad \phi_{INT-2} \quad \phi_{INT-3} \quad ..... \quad \phi_{INT-Nt}\right]$ represents the interferometric phase due to each target pixel.

Thus if the slope as seen in Figure 5-17(a) is denoted by *S* and the interferometric phase $(\phi_1 - \phi_2)$ due to target '*t*' is given by ϕ_t, then the height h_t of that particular pixel is given by,

$$h_t = \frac{\phi_t}{S} \tag{5.5}$$

We can apply (5.5) to an entire vector consisting of the interferometric phase values corresponding to each pixel and this enables us to construct an elevation model using the estimated height values. A topographic scenario generated using the *peaks* function in MATLAB was provided as input to the radar simulator and the surface height was then estimated using the *topography estimation algorithm*.

The algorithm provides very good results with respect to estimating the height of each target pixel, as seen from the plots presented. An important observation made was that the algorithm provides accurate estimates of surface height if we assume that the surface topology is relatively regular and slowly changing – an assumption which works very well in all but the most rugged and mountainous regions.

Figure 5-18(a) depicts the high-resolution scenario that was considered as the next test case while Figure 5-18(b) depicts the results obtained by using the height-estimation algorithm. The plots on the following page show the corresponding contour plots which give us a good idea regarding the accuracy of estimation.

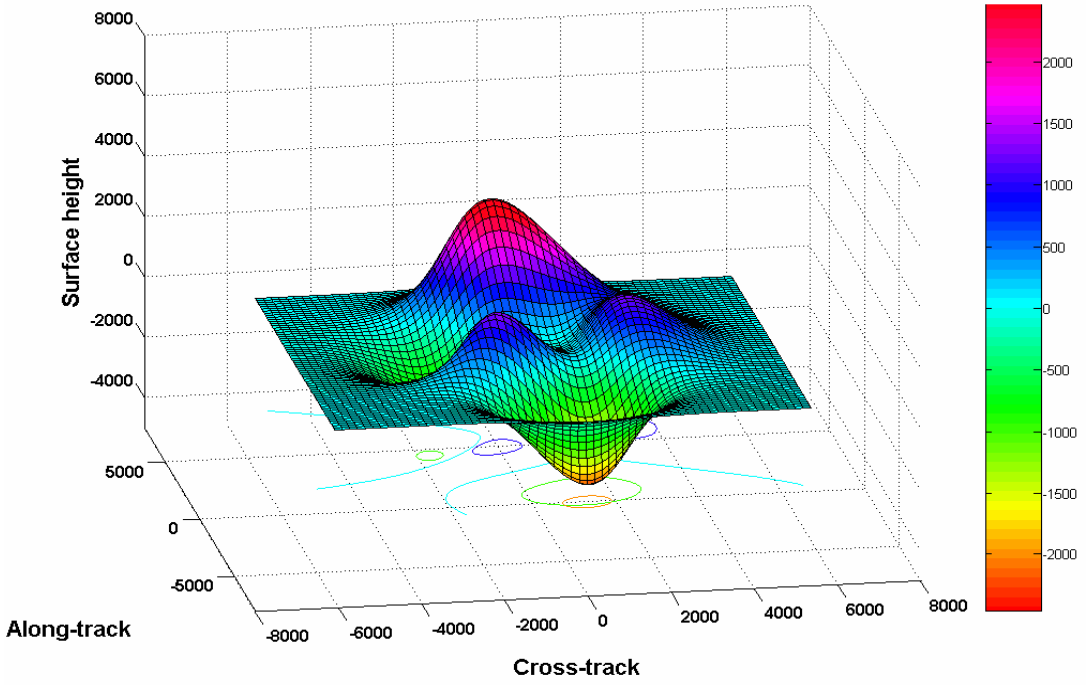

Figure 5-18(a) Three-dimensional elevation model depicting the ACTUAL topography-1

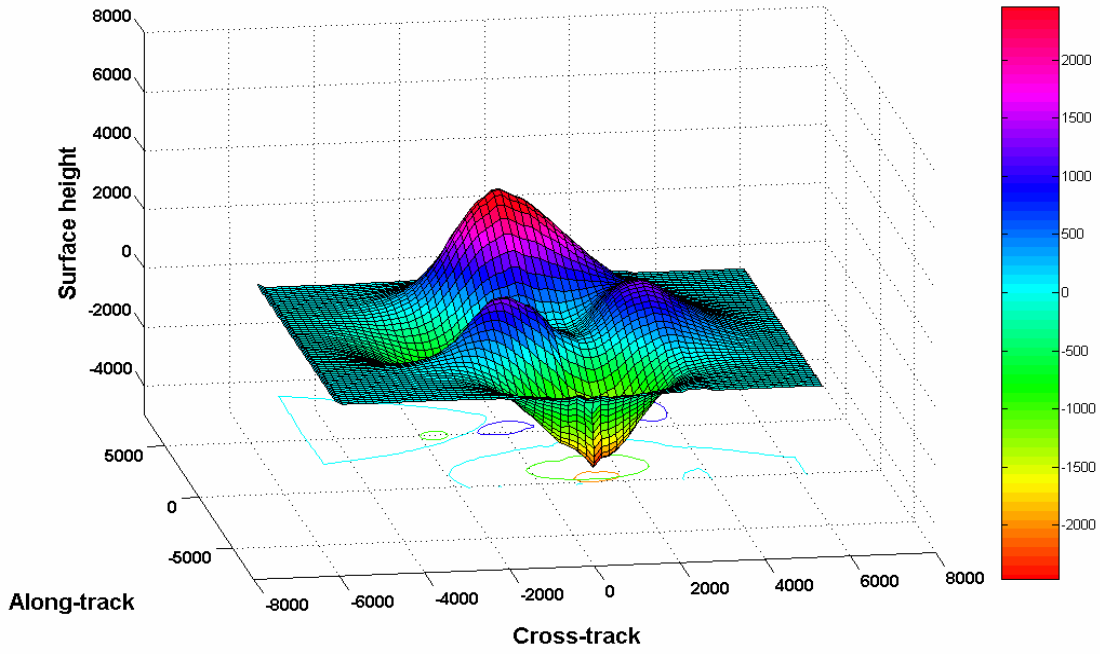

Figure 5-18(b) Three-dimensional elevation model depicting the ESTIMATED topography-1

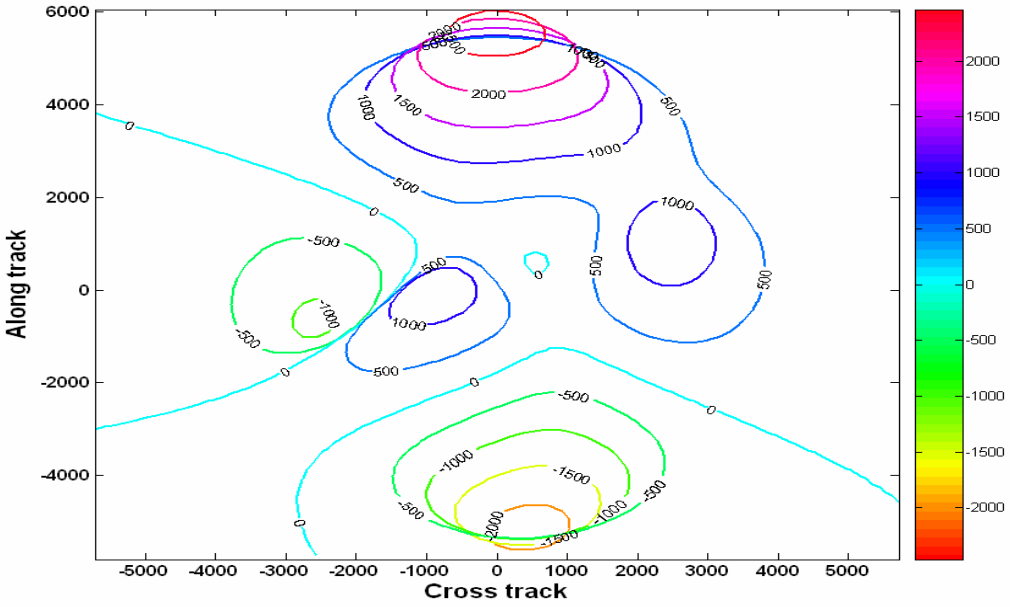

Figure 5-19(a) Contour plot depicting ACTUAL surface topography-1

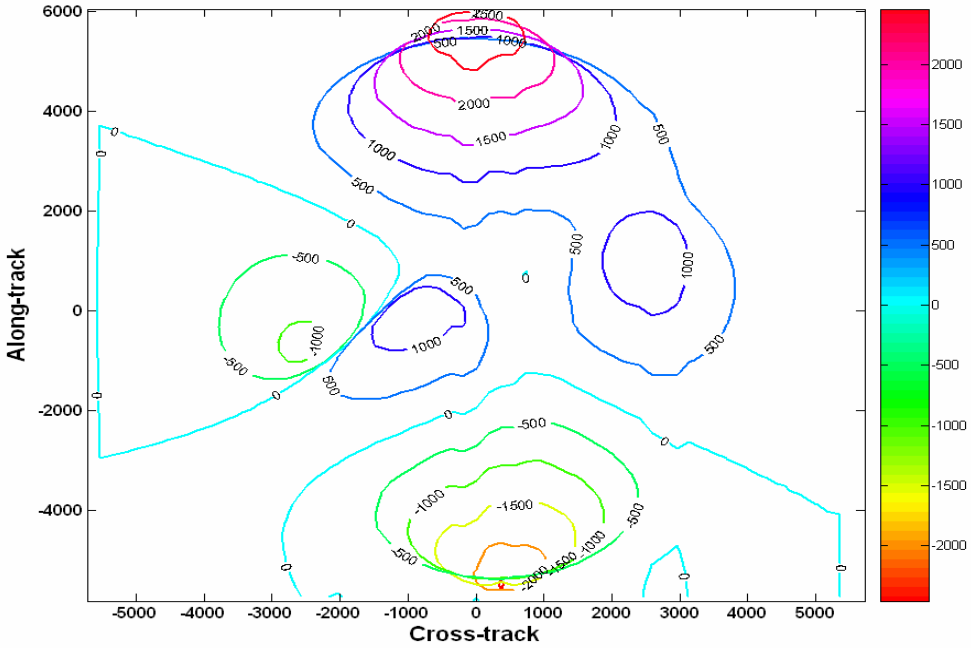

Figure 5-19(b) Contour plot depicting ESTIMATED surface topography-1

It should be pointed out that one important assumption that was made in all these simulations is that the maximum height encountered over a given topography was always taken to be within the width of the main beam of the receive antenna [Figure 5-17(b)] so that no phase ambiguities occurred. This simplifies our problem because otherwise height estimators usually provide typically degenerate solutions as a result of the ambiguity associated with phase measurement, which then needs to be resolved.

The algorithm was then tested on a different topographic scenario shown in Figure 5-20(a). Figure 5-20(b) shows the estimated surface height layout while Figure 5-21(b) provides a contour plot. The image with 63x63 resolution was the highest resolution image that was considered for simulations because processing an image with higher resolution was plagued by memory and computational constraints.

The tests carried out in this section thus far have clearly demonstrated the application of a new algorithm, which is very useful for processing the data from sparse satellite clusters and utilizing the information gathered by the radar to estimate the height of the illuminated topography.

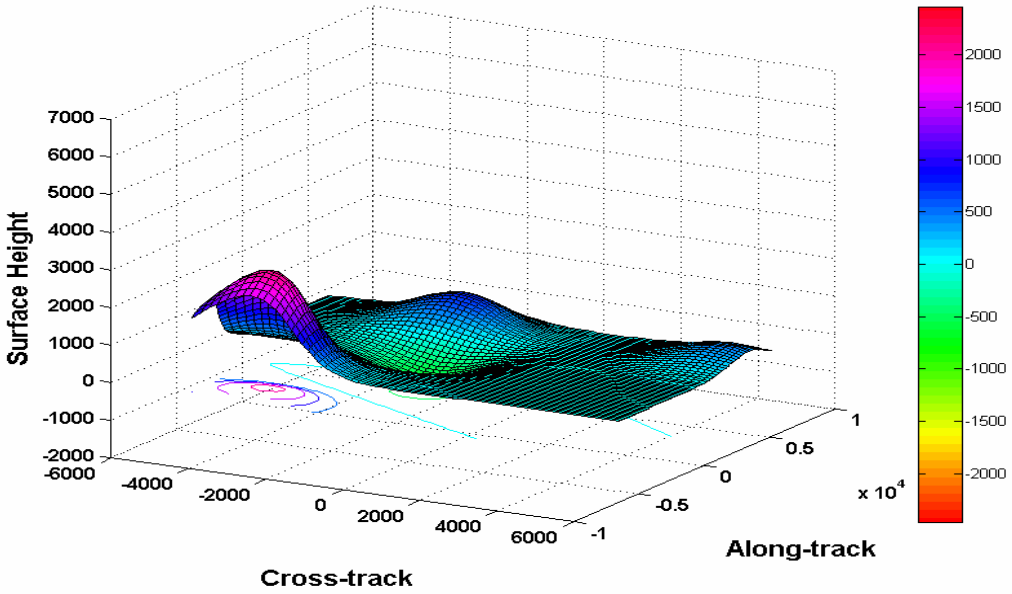

Figure 5-20(a) Three-dimensional elevation model depicting the ACTUAL topography-2

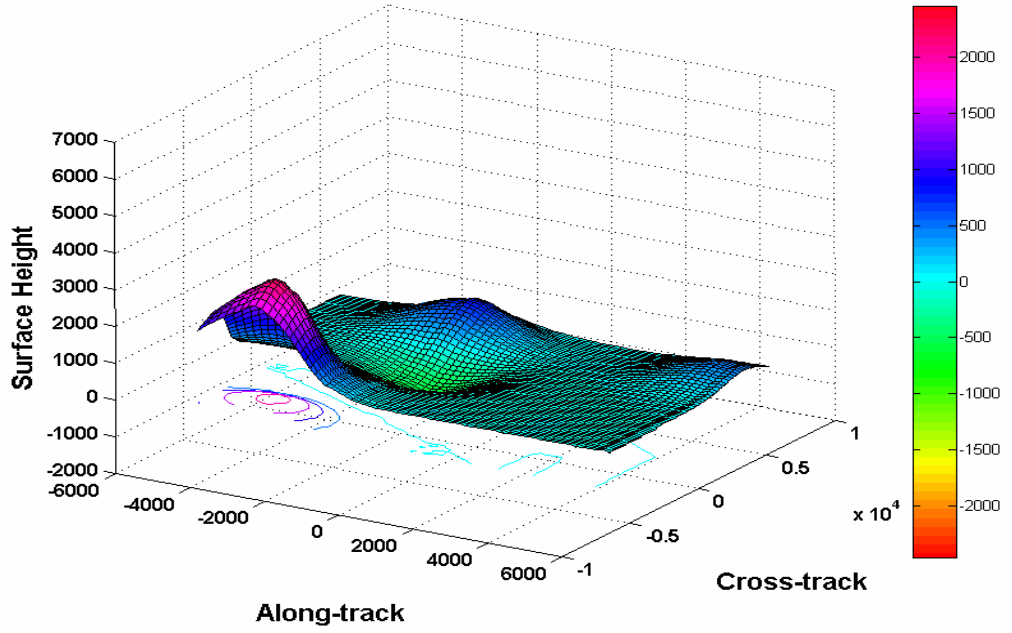

Figure5-20(b) Three-dimensional elevation model depicting ESTIMATED topography-2

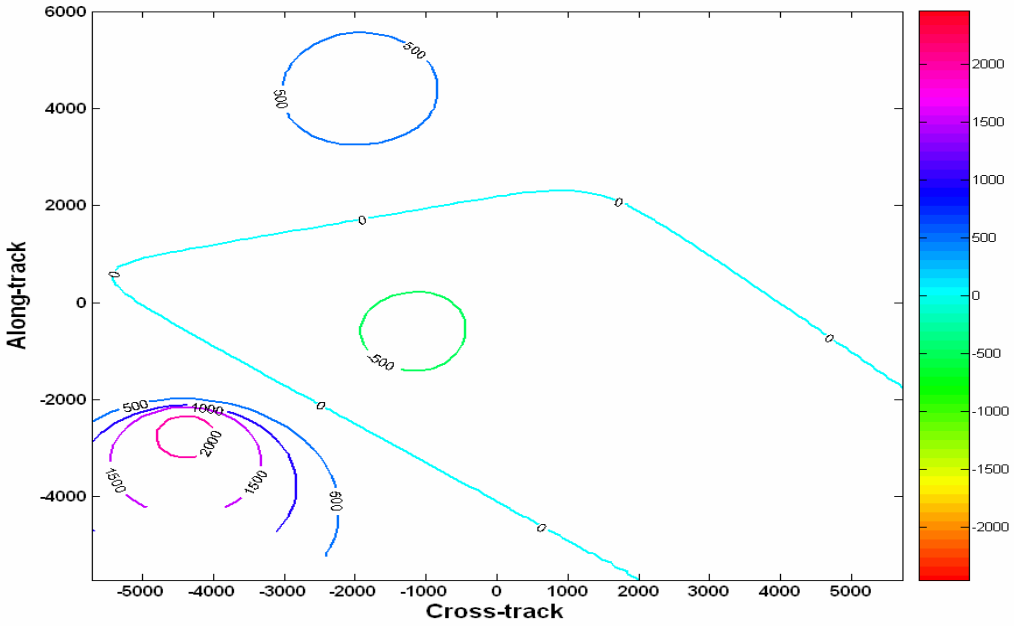

Figure 5-21(a) Contour plot depicting ACTUAL surface topography-2

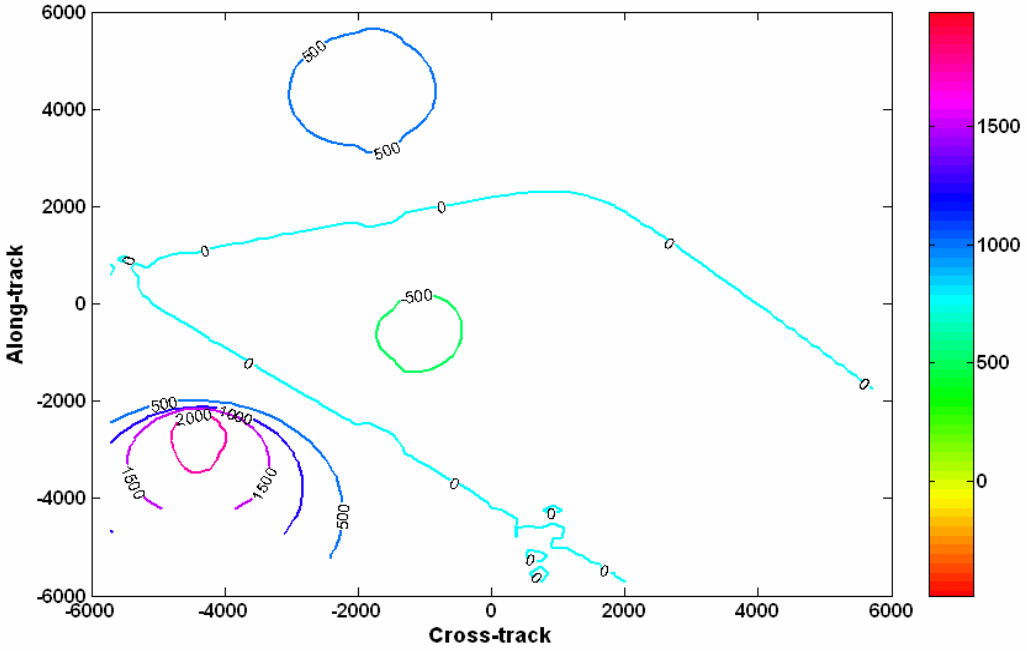

Figure 5-21(b) Contour plot depicting ESTIMATED surface topography-2

5.4 Test 3 – Forward-look SAR

All the tests that have been described up till now considered a normal side-looking SAR scenario. This section deals with the application of the *topography-estimation algorithm* to a forward-look SAR scenario.

5.4.1 Forward-look SAR geometry

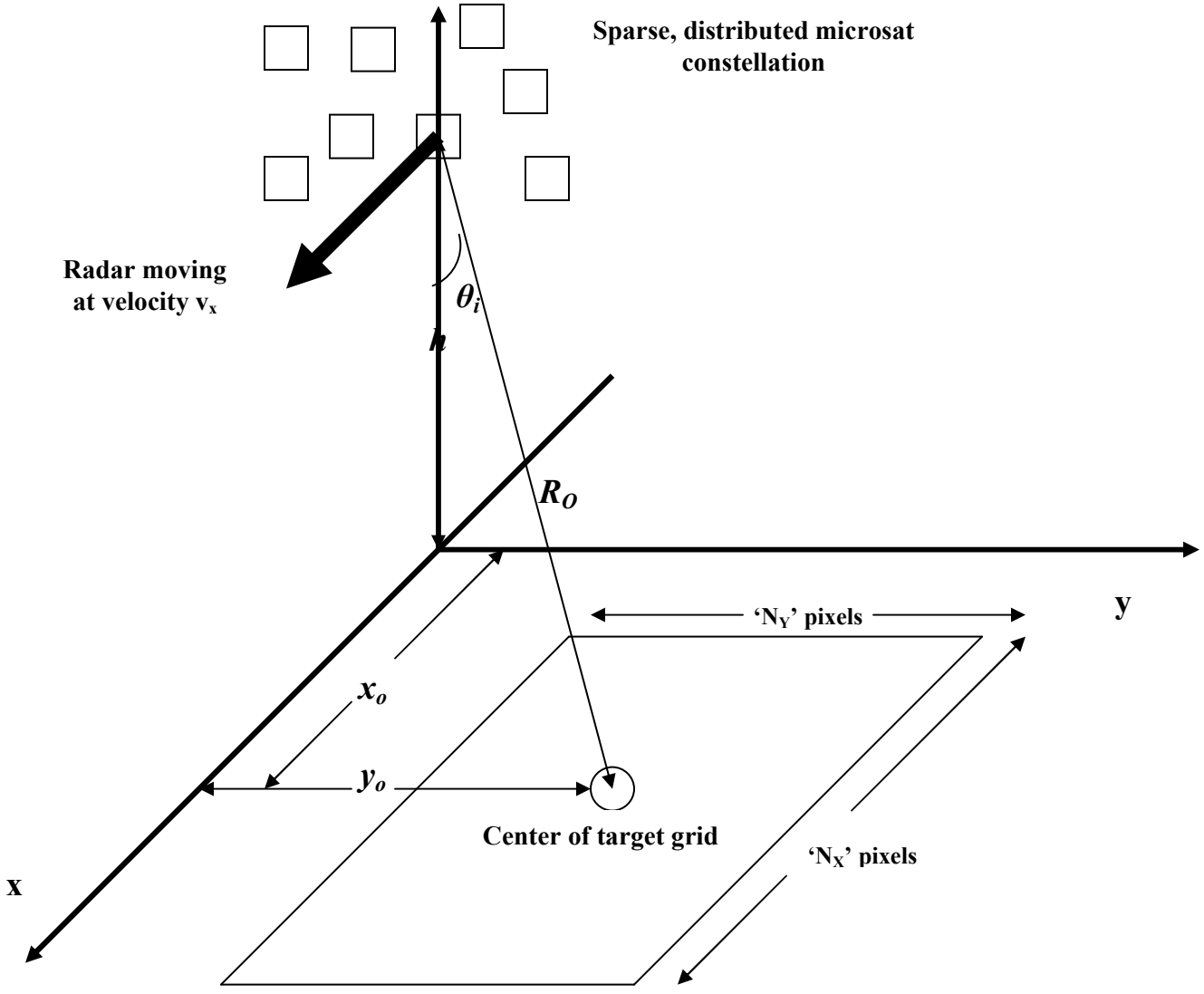

Figure 5-22 Radar Geometry (Forward-looking case)

Figure 5-22 illustrates typical forward-look geometry which is quite similar to the side-look geometry demonstrated in Figure 2-1. The sensor moves in the positive x-direction with a velocity v_x while the center of the square target grid is defined by the coordinates (x_o, y_o). In the side-looking case, $x_o = 0$ and $R_o = \sqrt{y_o^2 + h^2}$ whereas in the forward-look case, clearly $x_o \neq 0$ while $R_o = \sqrt{x_o^2 + y_o^2 + h^2}$.

Similar to the side-look SAR, the forward-look SAR creates a two-dimensional range-doppler mapping of the three-dimensional illuminated scene. However, a very important characteristic by which the forward-look differs from the standard side-looking SAR is the way in which its grid of range-Doppler resolution cells intersects the XY plane. This is shown in Figure 5-23. When imaging using side-look geometry, lines of constant range and constant Doppler in the XY plane intersect each other orthogonally. These intersections divide the XY plane into separate resolution cells. In forward-look however, these two sets of lines are parallel and do not resolve scatterers in the Y direction. Figure 5-23 basically illustrates this difference by showing sections of the iso-range Doppler circles for each case. Therefore, at low grazing angles, the side-look SAR provides little vertical resolution, while the forward-look SAR provides little resolution in the Y direction. Figure 5-24 provides a comparison of the image geometries in both the cases while Figure 5-25 gives an example of the difference in the images of a test site formed using both forward and side look scenarios.

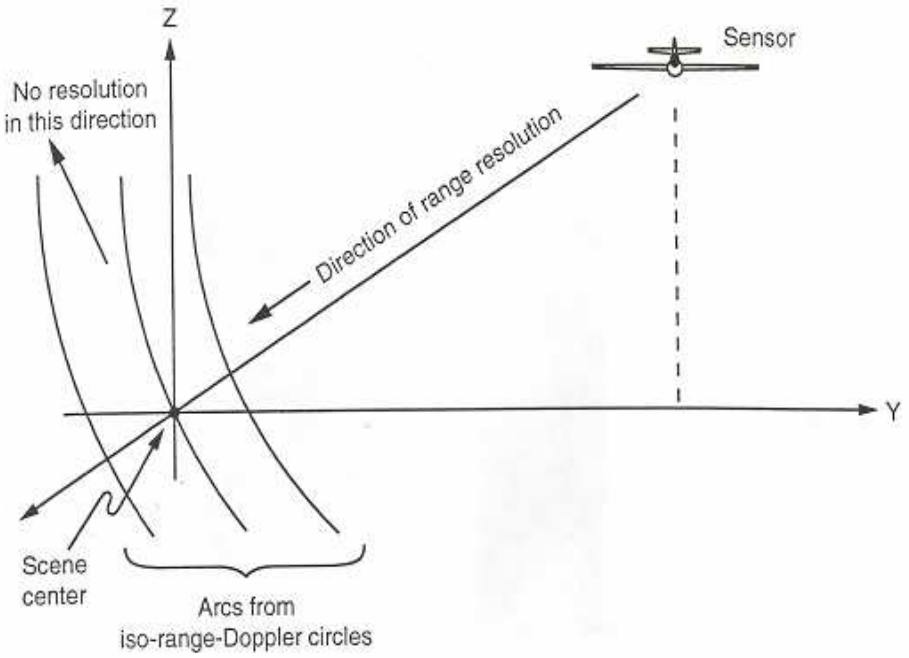

(a) Side-look SAR

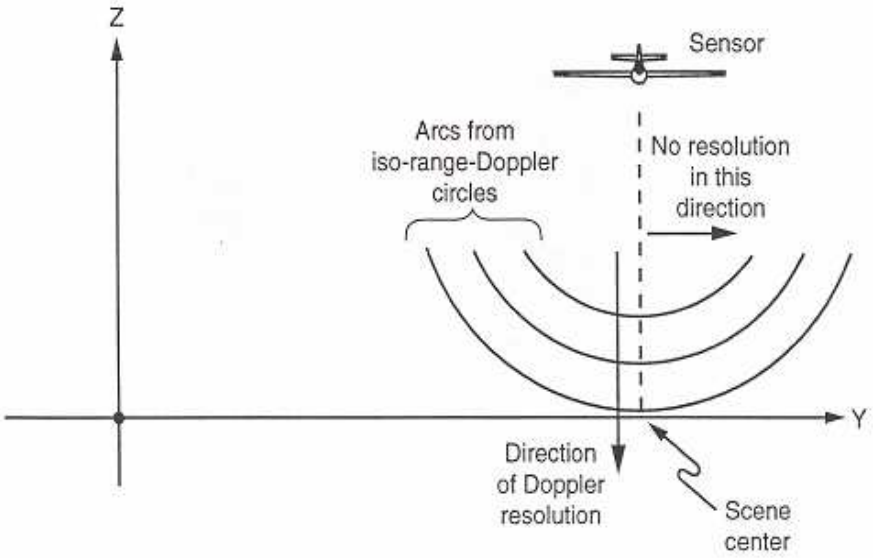

(b) Forward-look SAR

Figure 5-23 Directions of range and doppler resolution [6]

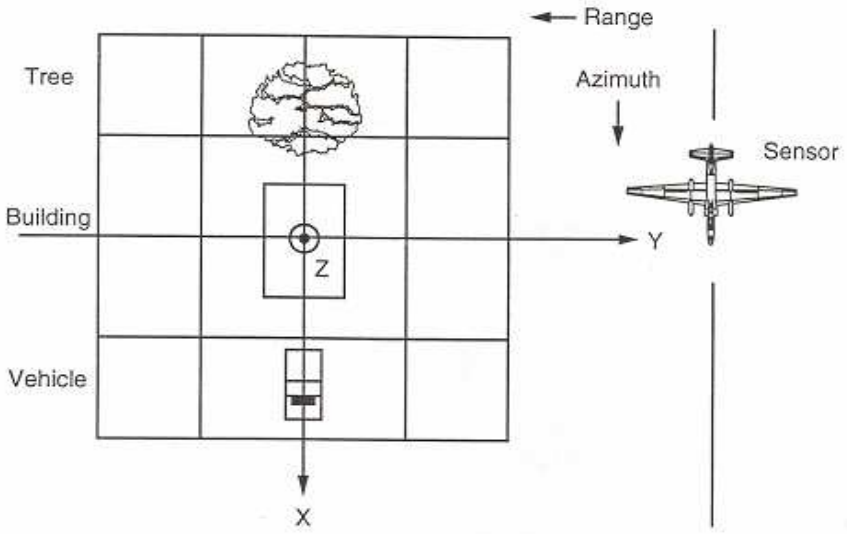

(a) Side-look SAR

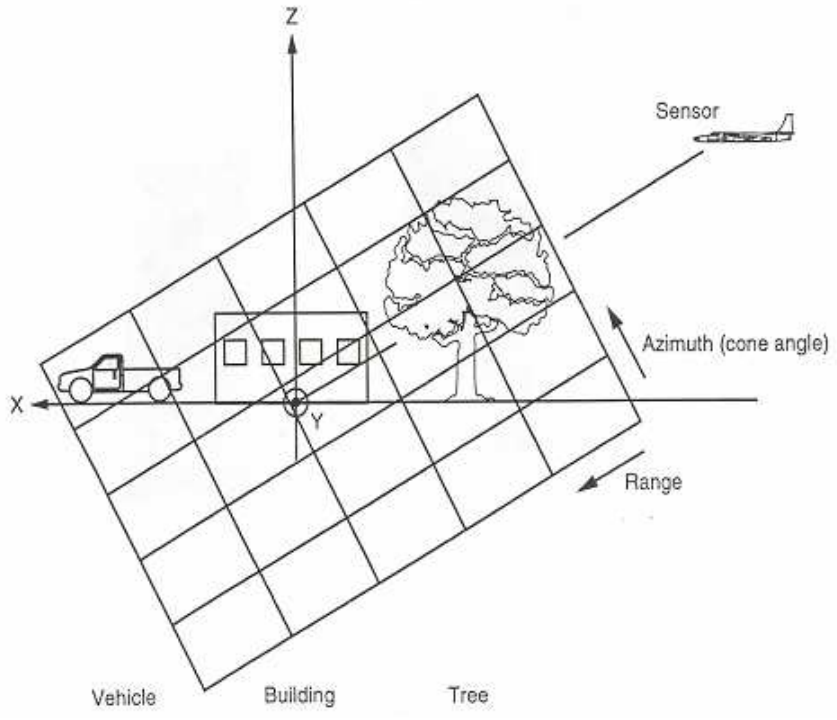

(b) Forward-look SAR

Figure 5-24 Illustration of Image geometries [6]

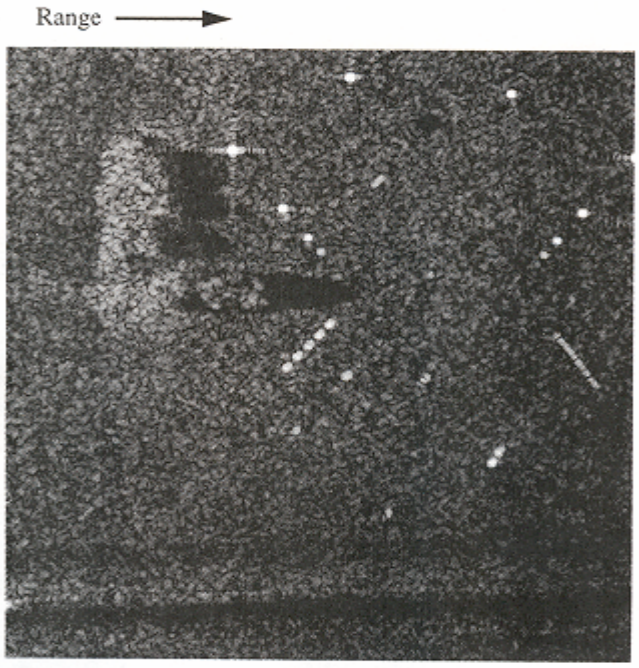

(a) Side-look SAR

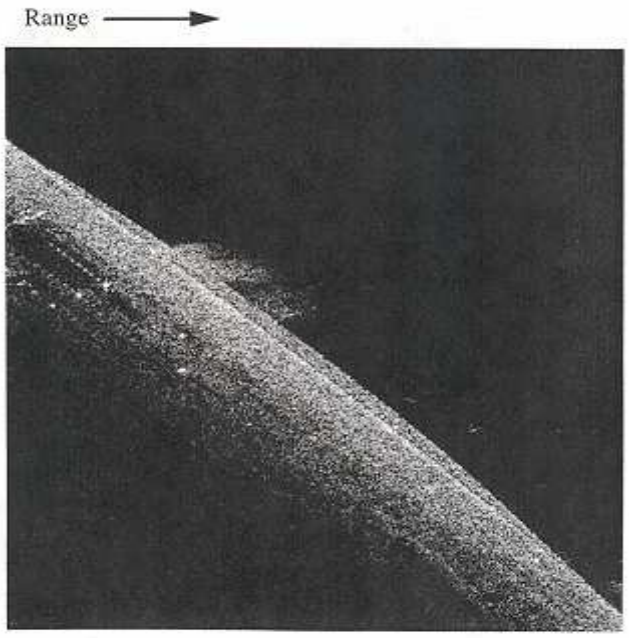

(b) Forward-look SAR

Figure 5-25 Images of a radar test site from two geometries [6]

It is observed that the eigensensor analysis is a *more complicated* when it comes to the forward-look (or backward look) case as compared to the standard side-look scenario. The eigensensor array looks very different and consequently the process of partitioning the measurement space to form two complex SAR images, is also more difficult. To start with, we know from (2.9) that,

$$K = \frac{w_c}{c}\begin{bmatrix} \frac{-(h^2+y_o^2)}{R_o^3} & \frac{x_o y_o}{R_o^3} & \frac{-hx_o}{R_o^3} & \frac{-2v_x(h^2+y_o^2)}{R_o^3} & \frac{2x_o}{w_c R_o} \\ \frac{x_o y_o}{R_o^3} & \frac{-(h^2+x_o^2)}{R_o^3} & \frac{-hy_o}{R_o^3} & \frac{2v_x x_o y_o}{w_c R_o} & \frac{2y_o}{w_c R_o} \\ \frac{-hx_o}{R_o^3} & \frac{-hy_o}{R_o^3} & \frac{-(x_o^2+y_o^2)}{R_o^3} & \frac{-2hx_o}{R_o^3} & \frac{-2h}{w_c R_o} \end{bmatrix}$$

As it has been mentioned earlier, x_0 is a non-zero value and consequently, all the elements of the K matrix are non-zero as well. After performing singular value decomposition on the above matrix, we obtain the projection vectors $\overline{u}_i$, $\overline{s}_i$ and $\overline{v}_i$. In the side-look case, we observed that the projection of the five dimensions of the measurement space (x,y,z,t,ω) into a three-dimensional eigensensor is such that each of the five dimensions is projected *only* along one eigensensor dimension. However, in the forward look situation, the projection is not that simple. Each measurement dimension is now projected on to more than one eigensensor dimension because of which the entire measurement space as well as the three-dimensional target space is rotated across the three dimensions. This is precisely what leads to the complicated eigensensor scenario, which was described earlier in this section. Figure 5-26(a) depicts the eigensensor array corresponding to 8 receive antennas recording 31 time

samples and 65 frequency samples. As seen from the figure, the time-frequency samples corresponding to each receive antenna do not line up neatly as in the side-look case but are spread out more sparsely. Hence, on partitioning the eigensensor, it is seen that the data samples localized within a given partition layer will generally not be localized in the physical measurement space of time, frequency and spatial locations. In other words, it is possible that two measurement samples taken at different times and at different apertures can occupy the same location on the eigensensor array.

Figure 5-26(b) shows the target grid in eigen dimensions. In order to determine the correct partitioning technique for the forward-look, we again define α, β and γ as the dimensions of the three-dimensional eigen sensor array while α_t, β_t and γ_t are the dimensions of the eigentarget space. The results of singular value decomposition show that the γ_t eigen dimension contains information about the target's height. The tests that we performed on the side-look scenario actually help us a lot to deal with the forward-look case because the information that we gathered earlier enables us to decide on how to go about partitioning this 3D eigensensor. For instance, we know that γ is the eigensensor dimension which can sense any change in target's height dimension and moreover the array is also *thinnest* along γ. Therefore, just as we did in the side-look case, we could partition the eigensensor in a direction perpendicular to the dimension (γ) that can sense the target height.

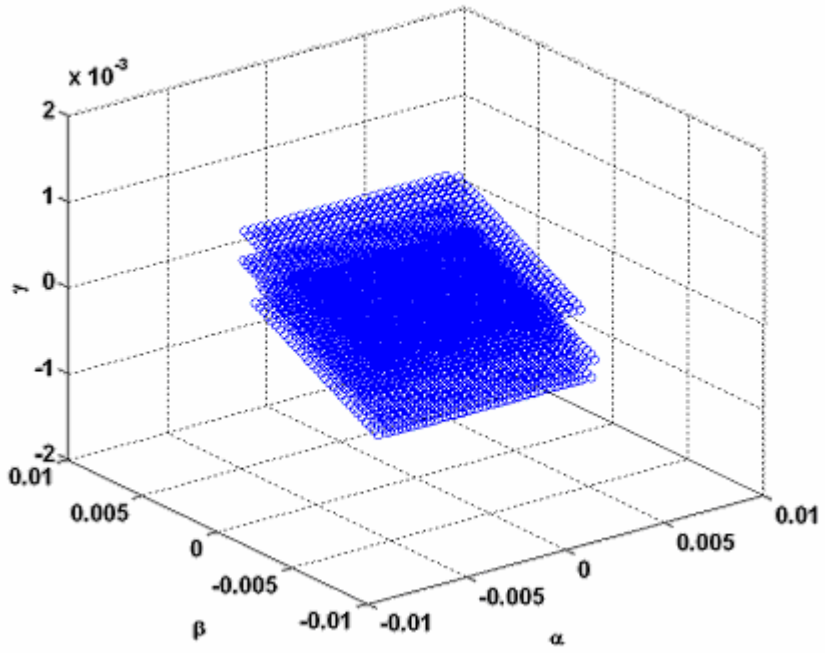

Figure 5-26(a) 3D Eigensensor array (forward-look)

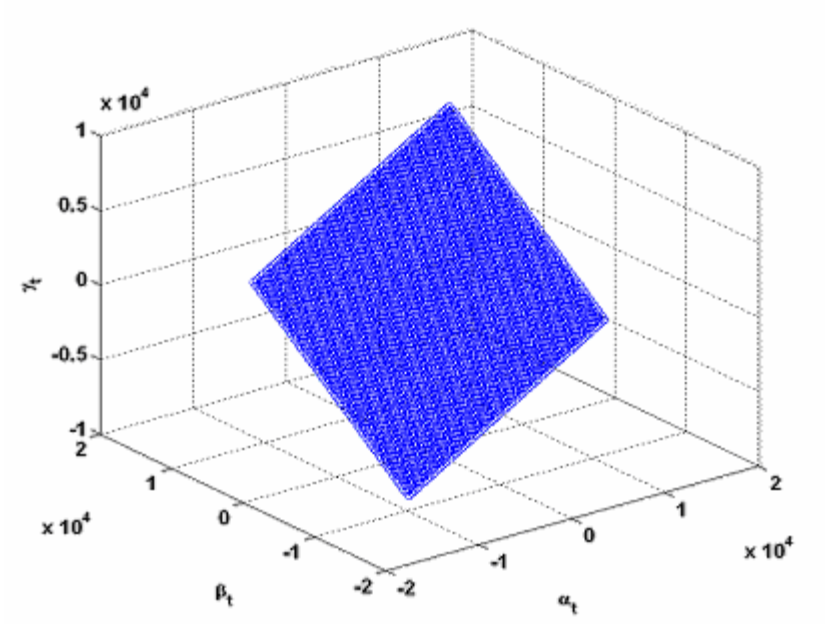

Figure 5-26(b) Target space (63x63 size) in eigen dimensions

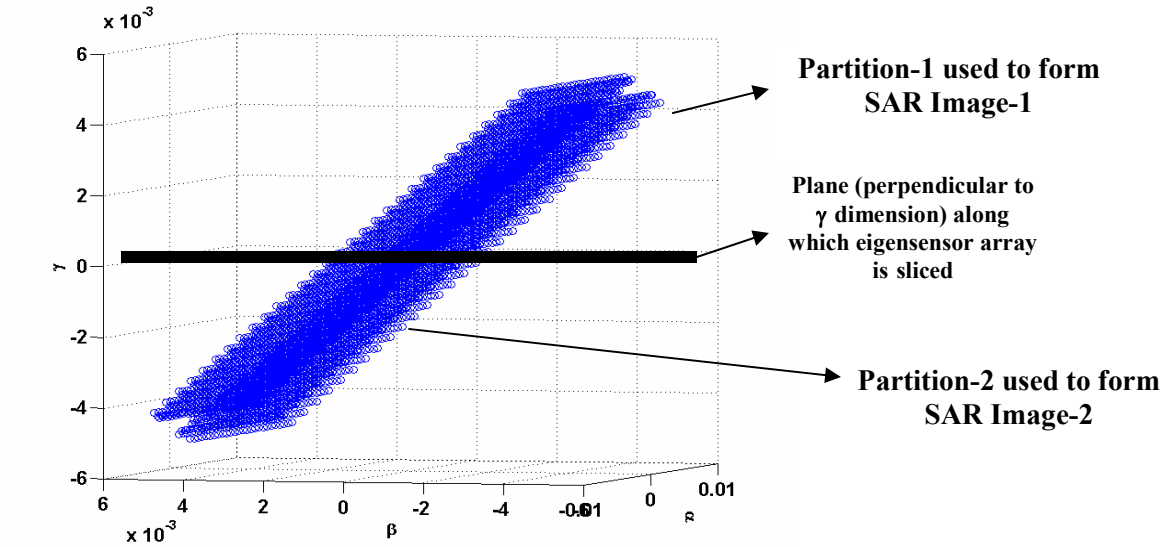

Figure 5-27 Partition of eigensensor – Forward-look scenario

Once we obtain the two sets of measurement samples, we can use them to form two complex SAR images to get two scattering estimates for each target pixel. As elaborated earlier, the partitioning process in the forward-look scenario leads to a situation wherein measurement samples corresponding to the same receive element may lie in different partitions. The procedure thereafter is exactly the same as the side-look case and we are then ready to apply the topography-estimation algorithm to the forward-look case.

5.4.2 Test 4-Results

Figure 5-28(a) depicts the actual topography provided to a SAR simulator which collects the measurements from a forward-look position. Figure 5-28(b) depicts the estimated surface topography – the result obtained as the output of the developed height-estimation algorithm.

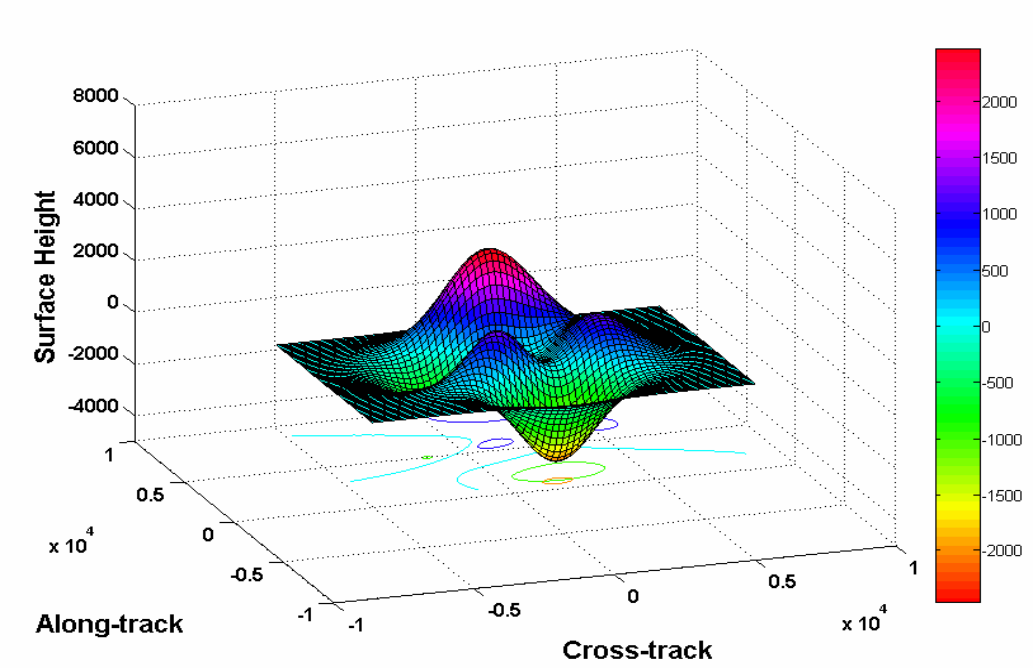

Figure 5-28(a) Three-dimensional elevation model depicting the ACTUAL topography

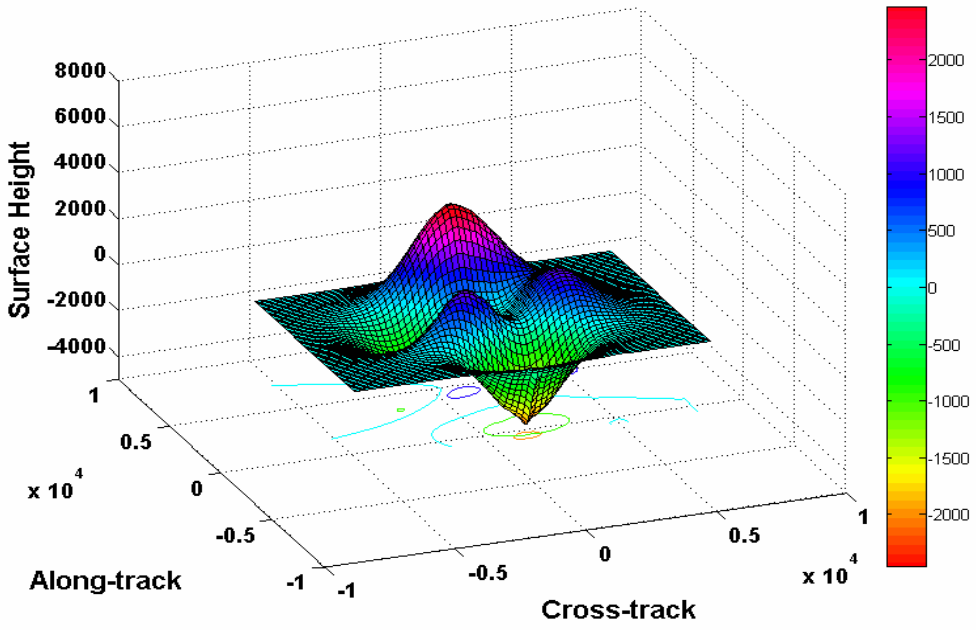

Figure 5-28(b) Three-dimensional elevation model depicting the ESTIMATED topography

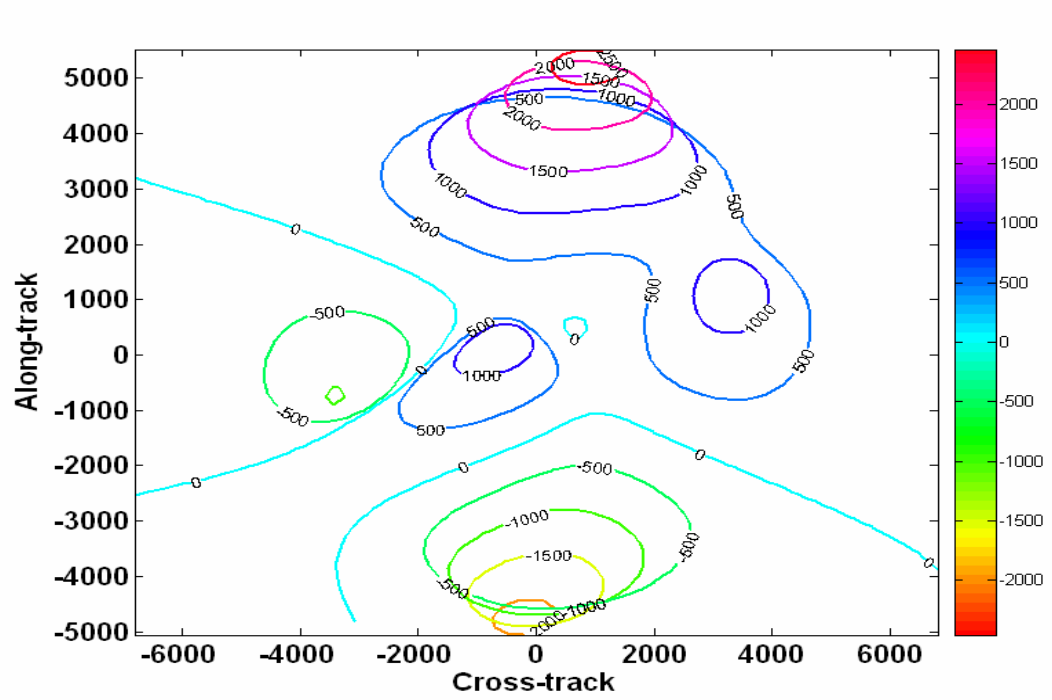

Figure 5-29(a) Contour plot depicting ACTUAL surface topography

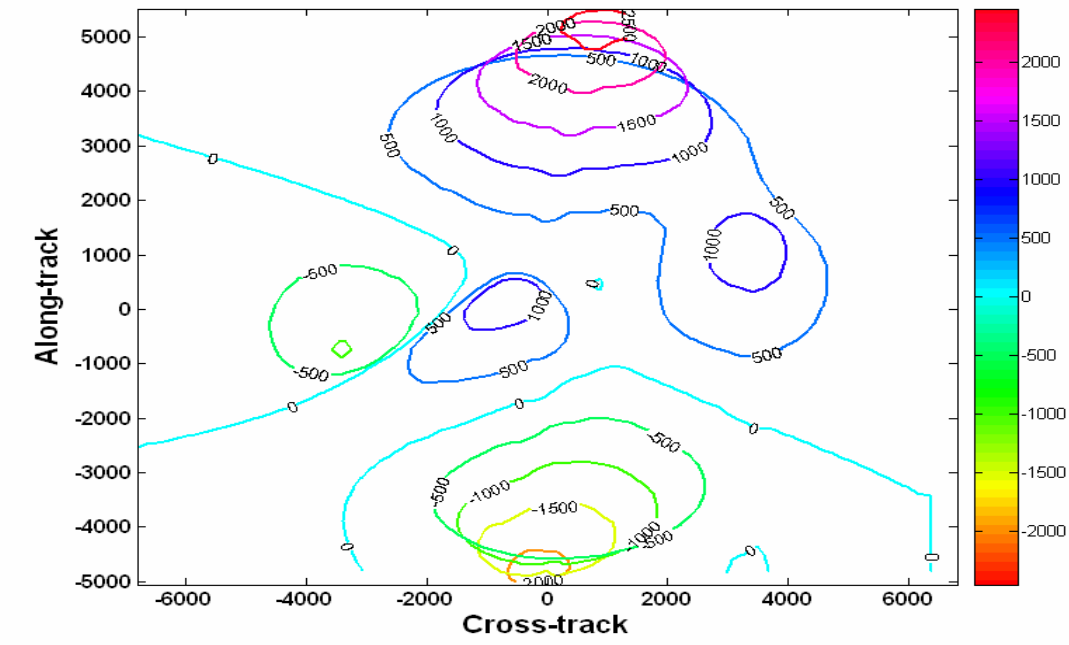

Figure 5-29(b) Contour plot depicting ESTIMATED surface topography

6. CONCLUSIONS AND FUTURE WORK

6.1 Conclusions

The main motivation for this research was the fact that existing SAR models and associated TopSAR processing algorithms developed for regular and linear arrays cannot be used for large, sparse, random arrays and, to the best of our knowledge, no study has been carried out to lay out the details regarding a TopSAR system which uses such a spaceborne distributed radar configuration. Therefore, the challenge was to organize the measurement data obtained from such a sparse and random radar configuration and process the data to form SAR images. Then, the need was to develop a topographic estimator, which could be applied to the processed data to determine the height of the illuminated surface. All these objectives were successively accomplished over the months of research dedicated to this problem.

A mathematical model [4] was developed and used to create a random, sparse space-time radar simulator. This model completely characterized the entire "distributed" radar constellation that is both sparsely populated and randomly spaced. The data samples from all the receive elements of such an array were collected to form a measurement vector of samples in space-time and frequency, whose dimension exceeds the clutter rank. Then, this measurement vector was optimally partitioned using the *three-dimensional eigensensor* approach. Through simulations, it is proved that under high SNR conditions, this approach has the potential to provide

high-quality, independent and unambiguous SAR images, which could then be used for estimation of surface topology.

A *topography estimation algorithm* was developed to estimate the surface height of an illuminated surface area. The height vector generated by the algorithm was then used to create a three-dimensional elevation model, which provides complete information about the height of each target resolution cell. Thus, it was proved that the data provided by a sparse and random configuration of arrays can also be used for topographic estimation, hitherto not possible using conventional sensors and algorithms.

6.2 Future work

The performance of the topography estimation algorithm developed during this research could be further evaluated as a function of factors such as transmit signal, illumination area, resolution, SNR, constellation size, number of microsats and satellite positioning error. The results obtained could then be compared with those procured with traditional interferometric SAR systems, in terms of both estimation accuracy and ambiguity. One big assumption that was made during the simulations was that the maximum height of the illuminated area lies within the region corresponding to unambiguous phase. However, future work could deal with the problem of phase ambiguity and incorporate the theory of phase unwrapping [17] to overcome this limitation. The performance of the estimator can also be further improved using super-resolution techniques such as MUSIC and ESPIRIT [21,22].

REFERENCES

[1] Nathan Goodman, "SAR and MTI processing of sparse satellite clusters", Doctoral thesis, The University of Kansas, July 2002

[2] A. Hein, "Processing of SAR data- Fundamentals, Signal Processing,Interferometry",Springer-Verlag,2004.

[3] Subhash Gullapalli, "Application of Kalman Filtering Technique for SAR Processing of sparse satellite clusters", Master's Thesis, The University of Kansas, December,2002.

[4] J.M. Stiles, "Space-Time Radar Transmission,Target and Measurement Model",Revison E, The University of Kansas, Radar Systems and Remote Sensing Laboratory, Lawrence, KS, August 2004

[5] Chris Oliver, Shaun Quegan, "Understanding Synthetic Aperture Radar Images",Artech House, Inc., 1998.

[6] Walter G. Carrara, Ron S. Goodman, Ronald M. Majewski, "Spotlight Synthetic Aperture Radar - Signal Processing algorithms", Artech House, Inc., 1995

[7] J.M. Stiles, "Transmit Signal Model", Revison 'E', The University of Kansas, Radar Systems and Remote Sensing Laboratory, Lawrence, KS, August 2004

[8] Riadh Abdelfattah, " Topographic SAR Interferometry Formulation for High-Precision DEM Generation", *IEEE Transactions on Geoscience and Remote Sensing*, Vol.40, No.11, November 2002.

[9] Nathan A. Goodman, J.M. Stiles, "Resolution and Synthetic Aperture Characterization of Sparse Raday Arrays", *IEEE Transactions on Aerospace and Electronic Systems*, Vol.39, No.3, July 2003.

[10] Nathan A. Goodman, J.M Stiles, "Synthetic Aperture Characterization of Radar Satellite Constellations", in *Proceedings of the IEEE International Geoscience and Remote Sensing Symposium*, Vol.1, pp.665-667, June 2002.

[11] Nathan A. Goodman, J.M. Stiles, "Clutter Rank estimation for radar satellite clusters", submitted to *IEEE Transactions on Aerospace and Electronics Systems*, June 2003.

[12] H. Steyskal, J. K Schindler, P. Franchi, R.J. Mailloux, "Pattern Synthesis for TechSat21- A Distributed Space-Based Radar System", IEEE Proceedings of Aerospace Conference, Vol.2, March 2001.

[13] J.M. Stiles, Nathan A. Goodman, SiChung Lin, "Performance and Processing of SAR Satellite Clusters", The University of Kansas, Radar Systems and Remote Sensing Laboratory, Lawrence, KS. June 2000

[14] D. Massonnet, "Capabilities and Limitations of the Interferometric Cartwheel", IEEE Transactions on Geoscience and Remote Sensing, vol.39, No.3, March 2001, pp.506-520

[15] Christopher T. Allen, "Interferometric Synthetic Aperture Radar", IEEE Geoscience and Remote Sensing Society Newsletter, No.96, pp. 6-13, September 1995

[16] Fawwaz T. Ulaby, Richard K. Moore, Adrian K. Fung, "Microwave Remote Sensing – Active and Passive", Vol. 2, Artech House, Inc., 1986

[17] Gordon W. Davidson, Richard Bamler, "Multiresolution Phase Unwrapping for SAR Interferometry", IEEE Transactions on Geoscience and Remote Sensing, Vol. 37, No.1, January 1999.

[18] Harold W. Sorenson, "Kalman filtering: theory and application", IEEE Press, 1985.

[19] Maurice Martin, Steve Kilberg, Pete Klupar, James Winter, "TECHSAT 21 and revolutionizing space missions using microsatellites", American Institute of Aeronautics and Astronautics.

[20] Air Force Research Laboratories, "TECHSAT 21 – FACT SHEET" Available : http://www.vs.afrl.af.mil/Factsheets/techsat21.html

[21] H.Yamada, K. Sato, Y. Yamaguchi, and W. M. Boerner, "Interferometric Phase and Coherence of Forest Estimated by ESPIRIT-based Polarimetric

SAR Interometry", *IEEE International Symposium on Geoscience and Remote Sensing*, Vol.2, June 24-28, 2002, pp.829-831.

[22] F. Gini, F. Lombardini, and M. Montanarti, "Layover Solution in Multibaseline SAR Interferometry," *IEEE Transactions on Aerospace and Electronic Systems*, Vol.38, No.4, October 2002, pp.1344-1356.